Quantitative techniques for permanent breast seed implant brachytherapy

by

Daniel R. Morton
B.Sc., University of British Columbia, 2011
M.Sc., University of Victoria, 2013

A Dissertation Submitted in Partial Fulfillment of the
Requirements for the Degree of

DOCTOR OF PHILOSOPHY

in the Department of Physics and Astronomy

Quantitative techniques for permanent breast seed implant brachytherapy

by

Daniel R. Morton
B.Sc., University of British Columbia, 2011
M.Sc., University of Victoria, 2013

Supervisory Committee

Dr. A. Jirasek, Co-supervisor
(Department of Physics and Astronomy)

Dr. W. Beckham, Co-supervisor
(Department of Physics and Astronomy)

Dr. M. Hilts, Departmental Member
(Department of Physics and Astronomy)

Dr. N. Dechev, Outside Member
(Department of Mechanical Engineering)

Supervisory Committee

Dr. A. Jirasek, Co-supervisor
(Department of Physics and Astronomy)

Dr. W. Beckham, Co-supervisor
(Department of Physics and Astronomy)

Dr. M. Hilts, Departmental Member
(Department of Physics and Astronomy)

Dr. N. Dechev, Outside Member
(Department of Mechanical Engineering)

ABSTRACT

Permanent breast seed implant brachytherapy (PBSI) is a recently developed form of treatment for early-stage breast cancer which can be completed in a single day procedure. Due to the reduced treatment burden, PBSI has the potential to benefit many women. However the technique has not been widely implemented, potentially related to the lack of a standardized, reproducible procedure and a high level of operator dependence. Challenges relating to target visualization uncertainties and the reliance on free-hand 2D ultrasound (US) guidance potentially inhibit adoption of the technique. This work aims to evaluate the current PBSI procedure to identify uncertainties and potential sources of errors in the current technique and develop methods to ameliorate these issues to potentially increase treatment accuracy, standardize the procedure, and reduce user-dependence.

A comprehensive assessment of the current PBSI procedure was performed to identify any trends or systematic errors in the placement of seeds and establish the effects

of seed placement accuracy on the treatment. Baseline seed placement accuracy, assessed in a 20 patient cohort was observed to be 9 ± 5 mm. Random displacements of seeds from their planned position contributed significantly to the overall accuracy. No trends or systematic errors were observed across the aggregate population, however intra-patient systematic offsets were observed. The potential effects of visualization of the post-lumpectomy cavity (seroma) on treatment delivery was investigated using spatially registered CT and 3DUS images. Planning the treatment on CT, as is standard practice, resulted in less than optimal coverage to target volumes defined on US in the majority of cases. The effects of intra-operative adjustments relating to the visualization differences on the two modalities was assessed by shifting the CT-based treatment plan to centre on the US-defined seroma. Such shifts were shown to potentially contribute to the systematic displacements observed in PBSI delivery, and also had significant dosimetric effects on the planned target volumes.

The impact of seroma visualization on PBSI implant accuracy was further assessed through the evaluation of CT and 3DUS images acquired for PBSI patients. Correlations were observed between the seed placement accuracy and the inter-user variability of seroma definition on CT ($r = 0.74$, $p = 0.01$) and the volume difference of the seroma on the two modalities ($r = 0.65$, $p = 0.04$), indicating that discrepancies in target delineation can impact treatment accuracy. The systematic displacements of the implants were observed to be correlated with the visualization metrics, however random displacements were independent of seroma delineation.

Deviations in needle positioning during insertion may not be realized until the implant is complete, thus contributing to the random inaccuracies in seed placement. A purpose built 3DUS scanning system was investigated for its use in guiding needle insertion. Registration of the treatment template with the imaging system was validated to provide accurate target localization for needle insertion. Adjustments and re-insertion of needles under 3DUS guidance provided significant improvements to the needle positioning accuracy. A simulated implant with the guidance system indicated that overall treatment accuracy may be improved through the clinical implementation of such a system.

Efforts to improve seroma definition during treatment planning and image guidance during the delivery can significantly increase seed placement accuracy and reduce the need for subjective intra-operative adjustments to the setup and needle positioning. Standardization of such advanced imaging techniques can greatly benefit the PBSI procedure by reducing user dependence and help to promote implementation.

Contents

List of Tables

List of Figures

List of Acronyms

3DUS - Three-dimensional ultrasound
AP - Anterior-posterior
APBI - Accelerated partial breast irradiation
CSI - Centre for the Southern Interior
CI - Conformity index
CTV - Clinical target volume
CT - Computed tomography
DVH - Dose volume histogram
EBRT - External beam radiation therapy
EC - Electron capture
ETV - Evaluative target volume
Grays - Gy
HDR - High dose rate
IR - Infrared
KERMA - Kinetic energy released in the medium
LDR - Low dose rate
ML - Medial-lateral
OAR - Organ as risk
OR - Operating room
PBSI - Permanent breast seed implant
PTV - Planning target volume
QA - Quality assurance
ROI - Region of interest
RT - Radiation therapy
SI - Superior-inferior
SPL - Spatial pulse length
S_k - Air kerma strength
TPS - Treatment planning system

TPX - Polymethylpentene plastic
TRUS - Transrectal ultrasound
US - Ultrasound
WBI - Whole breast irradiation

ACKNOWLEDGEMENTS

This dissertation is a product of countless contributions from many different people that I have had the pleasure of working with over the years. I would like to begin by thanking Drs. Deidre Batchelar and Michelle Hilts for their immeasurable support. Their guidance, input, and dedication have been invaluable and this work would not be possible without them. For everything they've taught me, for keeping me focused on what's important, for managing the "collection of emergencies", and for helping me keep my head on straight when times were tough, words cannot express how appreciative I am.

This project has been an incredible experience due to wealth of amazing people that I've had the opportunity to interact with. I want to thank all of the staff, researchers and students within the University of Victoria, the BC Cancer Agency, and beyond for everything I've learnt from them and all of the assistance they have provided throughout the course of my studies. Specifically, I would like to acknowledge Dr. Andrew Jirasek for the many years of guidance, my committee Drs. Wayne Beckham and Nikolai Dechev for their continued support and feedback, Dr. Juanita Crook for her expertise and passion for PBSI, Mark Robinson for brilliantly bringing my terrible schematics to life, the Early Detection team for their companionship and technical support, the CSI RTs who were always so happy to help, the team at Robarts Research Institute for their incredible work and assistance with this project, and the wonderful CSI medical physics group for all of their knowledge and inspiration. I also would like to sincerely thank the BC Cancer Foundation for their generous support.

Thank you to my incredible family, Mom, Dad, and Kyla, for a life-time of guidance, assistance, optimism and for always believing in me. And finally, thank you to my outstanding wife Hailey for the unconditional support, encouragement, and everything to help navigate this arduous journey. I am so fortunate to have such an incredible group of people close to me who have truly made this all possible.

Chapter 1

Introduction

Radiation therapy is one of the principle methods for treating cancer, along with surgery and chemotherapy. Widespread implementation of screening for breast cancer, one of the most commonly diagnosed cancers, has allowed for early detection of the disease and shifted standard treatment away from total mastectomy in favour of breast conserving surgery (lumpectomy) followed by irradiation of the whole breast [1–3]. Surgery and adjuvant RT has been shown to achieve equivalent disease-free survival rates as mastectomy with significantly improved cosmetic outcomes over a course of 5-7 weeks [3, 4].

Treatment times can be reduced, thus increasing patient convenience and reducing cost, by irradiating the lumpectomy cavity (seroma) alone [5–7]. A novel form of this partial breast irradiation is the permanent breast seed implant (PBSI) technique, which offers acceptable target coverage and normal tissue toxicity with the convenience of a single day procedure [8–10]. PBSI is therefore an attractive treatment option, especially with the large geographical catchment areas typical of Canadian treatment centres [11, 12]. However, widespread adoption of PBSI has been limited, impeding the potential benefits of the treatment for a broad patient population. The technique currently lacks a standardized, quantifiable delivery procedure and relies heavily on the skills and interpretations of the delivering oncologist. Challenges relating to target visualization, different imaging techniques for planning and delivery, and the reliance on free-hand ultrasound make the procedure difficult to implement. Improved imaging has the potential to significantly benefit the PBSI procedure, standardizing the planning and delivery processes. This work aims to quantify the uncertainties throughout the PBSI procedure, evaluate how they impact the accuracy of the treatment and determine the imaging methods required to reduce them, thus

improving confidence and facilitating implementation.

1.1 Radiation Therapy

The discovery of x-rays and radioactivity in the late 1800's quickly lead to new applications for radiation in medicine, from medical imaging to the treatment of cancer. Radiation therapy (RT) aims to treat cancerous regions with high doses of ionizing radiation while sparing normal, healthy tissue. Early RT treatments were limited, particularly due to the low x-ray energies and crude planning methods available, restricting treatments to shallow and well defined tumour sites [13]. The transition from a primarily palliative treatment to a curative option began in the 1930's through improved treatment planning. The development of cobalt-60 treatment units in Canada in 1951 lead to the widespread implementation of megavoltage treatments, which have become the standard of care with modern day linear accelerators [13–16]. Currently, radiation treatments are generally delivered using either brachytherapy (Section 1.1.3), which delivers dose from within the patient using radioactive sources, or external beam radiation therapy (EBRT), commonly delivered through the use of high energy linear accelerators. The development of new delivery technologies, radioactive isotopes and implant techniques, and image guidance has made RT a primary method for treating cancer in the world today, with over half of all cancers being treated with some form of RT [17].

1.1.1 Principles of Radiation Therapy

Uncontrolled abnormal proliferation by mutated cells results in the growth of tumours, or cancer [18]. Treatment of cancer is focused on the removal or destruction of these mutated cells in order to stop the growth and spread of the disease. Surgical removal is the primary form of treatment for many types of cancer, but may be limited by the location and spread of the disease [18]. Chemotherapy is used in a wide variety of cancer treatments to provide symptom relief and disease control, but is often used in combination with other curative treatments [17]. Radiation therapy is an effective treatment option which can be targeted to kill cancer cells while potentially maintaining normal tissue function and cosmesis relative to invasive surgeries. Depending on the disease, RT can be used as a sole curative modality or, more commonly, as an adjuvant treatment following surgery to provide improved

local control rates [17].

Radiation is effective at treating cancer because of its ability to cause the death of individual cells [17]. Exposure of cells to radiation results in a system of physical, chemical, and biological events that ultimately lead to cellular death or the inability for the cell to further reproduce. Ionizing radiation causes charged particles to interact throughout a medium and may result in the creation of highly reactive molecules which will subsequently undergo many reactions to restore electronic equilibrium. When these reactions occur within a cell the DNA can potentially be damaged and, if not fully repaired, lead to its death through various different pathways [17]. Therefore, exposing volumes to high doses of radiation will subsequently result in the death of the cells within and can provide local tumour control to cancerous regions.

Damage from radiation can also occur in normal, healthy tissue. During RT, normal tissue is unavoidably exposed to radiation which can result in negative effects of the treatment. Short term side effects, such as the breakdown of the skin, result from the death of healthy stem cells and the loss of subsequent cells that they would have produced [17]. Late side effects can include the loss of function when components of organs are damaged, or even the induction of secondary cancers, and may take years to appear [17]. RT can therefore be limited by the location of the disease since adequate dose can not always be delivered to the tumour without seriously harming critical structures. Due to the proximity of healthy tissue to the cancer, normal tissue complications must be considered in addition to local tumour control in order to ensure the patient completes treatment with a high quality of life [19]. Modern RT uses complex planning and delivery techniques to balance these two goals and achieve the best possible treatment.

1.1.2 Radiation Treatment Planning and Delivery

Radiation therapy treatment planning is based on extensive calculations of the prospective radiation dose distributions to the patients' anatomy. Modern RT relies heavily on 3D-volumetric imaging of the patient in order to determine the areas to be treated and the dose to the target and surrounding tissue that will result from the treatment in a simulation procedure. The success of the treatment is directly related to the effectiveness of the simulation [18].

Treatment simulation processes vary widely, but computed tomography (CT) is the most commonly used imaging modality for treatment planning [20]. Patients

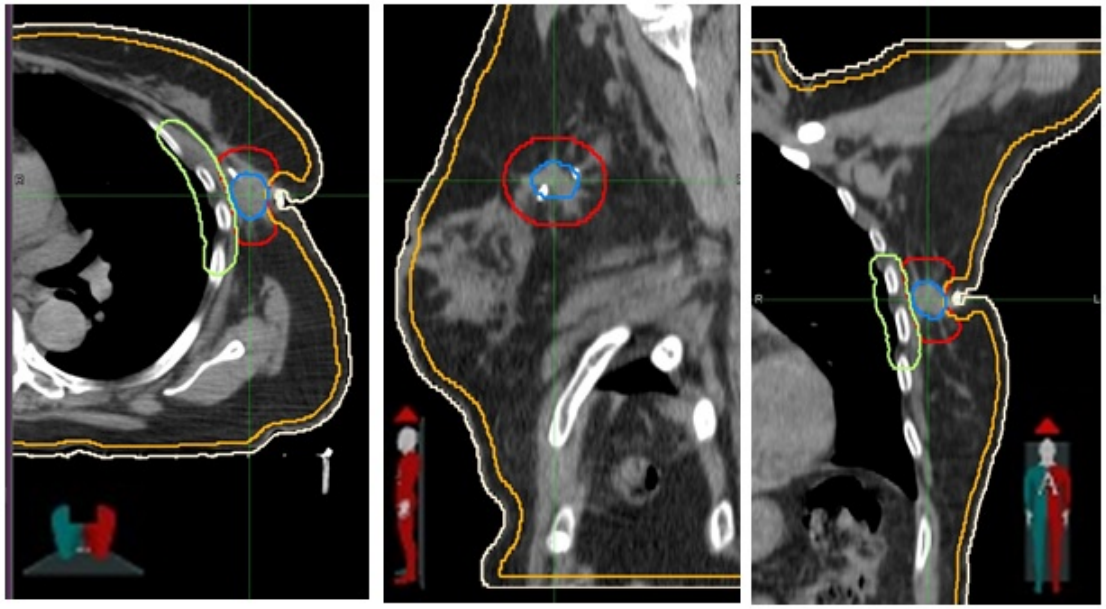

Figure 1.1: The anatomy of the breast, including contoured CTV (blue) and PTV (red), chest wall (green), and skin (orange) observed in 3 orthogonally reconstructed CT imaging plans in the TPS. From left to right, the planes are referred as axial, sagittal, and coronal

generally undergo CT imaging in the proposed treatment delivery position and the images are used in a computerized treatment planning system (TPS) to observe the anatomy in different imaging planes and define the treatment, as shown in Figure 1.1. In post-surgical treatments, the primary region to be treated is defined by oncologists as the clinical target volume (CTV), and a planning target volume (PTV) is usually defined as an expansion of the CTV to account for geometric uncertainties [18]. Organs at risk (OAR) are also contoured on the images. Plans are created in a variety of ways depending on the type of treatment. Traditional forward planning methods are performed by defining and manually adjusting treatment parameters to achieve the desired dose, while advanced inverse planning begins by defining dose constraints to the anatomy and the parameters are computed to optimize the dosimetry. Dose volume histograms (DVH) are used to assess the planned dosimetry on the clinical targets and OARs and ensure that the dose distribution meets predefined constraints. Adjustments may be subsequently made to achieve a sufficiently high dose and acceptable distribution to the PTV and reduce dose to OARs before the plan is finalized for treatment.

Radiation treatments can be delivered using a variety of different brachytherapy

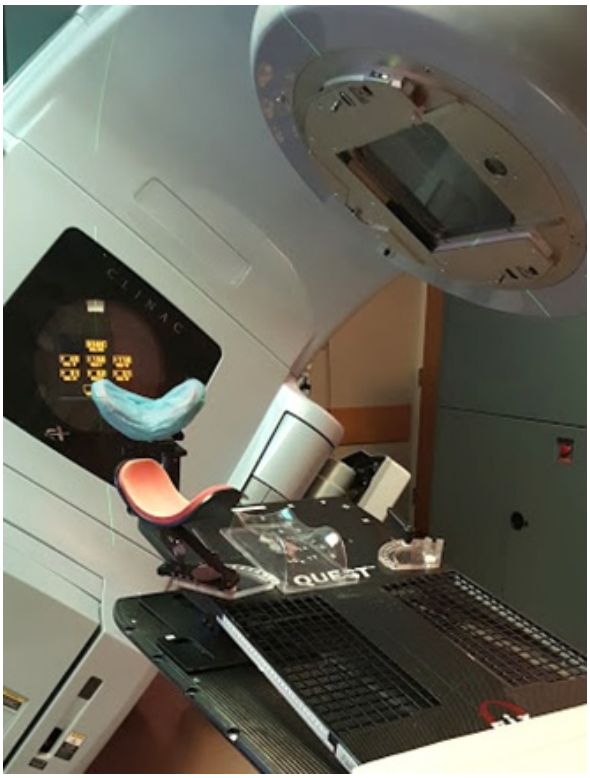

Figure 1.2: Angled breast board positioned to raise the right arm for breast radiation therapy with a high-energy linear accelerator.

(Section 1.1.3) and EBRT techniques. Regardless of the method, treatment delivery begins by replicating the patient positioning used for treatment planning so that the plan may be delivered as originally intended. Accurate repositioning of the patient is critical to the success of RT as variations in the patient positioning may result in the dose being delivered to incorrect areas and thus compromising the treatment [18, 19]. Devices, such as a breast board (Figure 1.2), may be used for patient immobilization and reproducibility.

Radiation treatments are generally delivered in a fractionated schedule, depositing dose over the course of several days or weeks, in order to maintain a balance between tumour death and normal tissue complications [17]. For example, standard whole breast RT is delivered daily over 5-7 weeks [6]. In order for the treatment to be successful, the correct dose must be delivered over each fraction. However, the anatomy will inevitably change throughout the course of the treatment and uncertainties in positioning inhibit the accuracy of the delivery. Large PTV margins are therefore often required to ensure that the correct dose is given to the target volume, at the

risk of exposing more normal tissue than necessary. Modern RT techniques aim to reduce treatment margins through advanced delivery and image guidance in order to provide escalated dose to the target volumes without compromising normal tissue.

1.1.3 Introduction to Brachytherapy

Brachytherapy is defined as the irradiation of a target area using radiation sources (typically radioactive isotopes) which are placed directly within, or very near to the intended treatment volume [21]. Following the discovery of the radioactive properties of uranium by Becquerel in 1896 and radium by the Curies in 1898, brachytherapy was first used as a cancer treatment in 1903 [21, 22]. Treatments have since evolved from the use of radium-226 (^{226}Ra), primarily in inter-cavity and skin treatments, to the development of numerous radioactive sources applied to the treatments of cervical, lung, oesophageal, prostate, and breast cancer, among many others. The insertion of needles loaded with low-energy radioactive sources (seeds), such as palladium-103 (Section 2.1.3), which are permanently implanted into the target volume is known as low-dose-rate (LDR) permanent seed brachytherapy, commonly referred to as LDR brachytherapy. The primary use for LDR brachytherapy is in the treatment of prostate cancer using iodine-125 (^{125}I) (described further in Section 2.3.2), a process that was introduced widely in the 1980s and has become a standard treatment option [21]. Modern technology has allowed for the implementation of high-dose-rate (HDR) treatments in which high-activity sources such as irridium-192 (^{192}Ir) are remotely mechanically moved through implanted catheters (interstitial brachytherapy) with pre-calculated dwell positions and times to optimize the coverage to the target volume and surrounding tissues.

The prevalence of brachytherapy continues to increase, as treating cancer using brachytherapy has several advantages over EBRT. While brachytherapy treatments are more invasive than EBRT, often requiring an operating room (OR), anaesthesiology, and post-anaesthetic recovery, overall treatment times range from a single day operation (for permanent implant LDR) to several fractions of HDR brachytherapy. Compared to the 5-35 days of treatments required for most EBRT, the rapid treatment times of modern brachytherapy presents a distinct advantage, especially when considering commitments for patients required to travel long distances for their treatments. While patient comfort is an important factor when considering different types of treatments, a principle reason for choosing brachytherapy over EBRT relates

to the dose delivery. EBRT requires x-rays from external sources to pass through normal tissues in order to reach the target volume. In contrast, brachytherapy irradiates from within the diseased tissues, bringing the desired dose directly to the target. Therefore, high doses may be delivered to the target, in a relatively short time, while the greater distance of the surrounding tissue from the source will inevitably result in a considerably reduced dose [21].

Since the sources in brachytherapy are directly connected to the target, variations in treatment due to patient motion are small compared to EBRT and therefore treatment margins may be reduced to limit the exposure of healthy tissue. However, due to the limited number of HDR fractions, and the permanent nature of LDR brachytherapy, intra-operative and post-implant adjustments and corrections to the treatment are difficult to achieve. Therefore, precise implantation of the sources is especially important to achieve an accurate and successful treatment. Traditionally, brachytherapy was limited to few sites with well-defined geometry, such as gynaecological and skin cancer, but modern innovations in volumetric treatment planning and image guided delivery has allowed for more complex tumour sites to be successfully treated while limiting toxicity related to the irradiation of healthy tissue.

1.1.4 Imaging in Brachytherapy

Similar to EBRT, planning for brachytherapy is primarily performed using 3D volumetric images. Volumetric datasets acquired using 3D imaging modalities such as computed tomography (CT) and 3D ultrasound (3DUS) (Section 2.2) are an important component of defining treatment volumes and planning source positions since they allow for improved visualization of the anatomy and more accurate dose calculations over traditional 2D imaging [21]. Currently, CT is the most widely used imaging modality for planning the majority of brachytherapy sites [21]. Originally, LDR prostate brachytherapy procedures required CT imaging to create volumetric data to use for treatment planning, while the implant procedure was guided using transrectal ultrasound (TRUS). The development of spatially registered US imaging allowed for the TRUS system to acquire a 3D dataset (Section 2.2.3), which could then be used to define the CTV (prostate plus margins), plan source positions, and calculate dose. Eliminating the need for CT reduced the uncertainties relating to the visualization and changes in the positioning that arise from the use of different imaging modalities, making the procedure more accurate and TRUS-based prostate

brachytherapy a standard treatment [21]. The same principles have currently been explored for HDR prostate brachytherapy as well, eliminating the need to move the patient between catheter insertion, imaging, and delivery [23, 24].

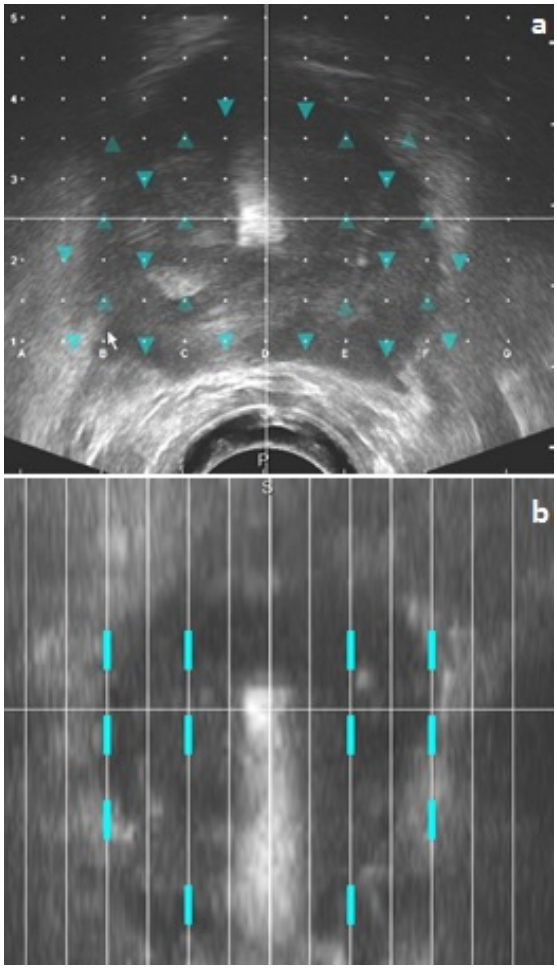

Figure 1.3: Virtual display of the treatment template (white dots (a) and lines (b)) on TRUS images used for prostate brachytherapy, viewed in the (a) needle insertion direction and (b) perpendicular to the insertion. Visible template positions allow for real-time feedback on needle positioning to assess the quality of the implant and make intra-operative adjustments.

In addition to treatment planning, US imaging is important to the success of brachytherapy as a guidance method during delivery. The probability of local tumour control in RT is directly related to the amount of radiation that a tumour is exposed to, with moderate dose escalations resulting in significant increases in tumour control probability. The benefits of conformal brachytherapy treatment planning may be lost if the radiation sources can not be implanted as planned. Access to precision image

guidance allows for more effective treatments by providing a visual confirmation of brachytherapy source positions relative to the patient's anatomy, and confirming the sources are being placed in their pre-calculated planned positions. For example, shown in Figure 1.3, during prostate brachytherapy implants the treatment template can be spatially registered to the TRUS system, creating a virtual representation of the template and planned source positions on the US images. The imaging can then be used to assess the quality of the implant and make adjustments to the implanted needle positioning before seeds are deposited. Knowing exactly where the sources are being placed ensures that the dose is being sufficiently distributed to provide local tumour control and minimize healthy tissue toxicity and thus increase the confidence in the procedure.

1.2 Permanent Breast Seed Implant Brachytherapy

Breast cancer is the most commonly diagnosed cancer in women, with an estimated 1 in 8 risk of developing the disease over a woman's lifetime [17, 18]. Treatment for breast cancer was traditionally performed by removing the entire breast along with the axillary lymph nodes and pectoral muscle in a process known as a "radical mastectomy". It wasn't until the widespread implementation of breast screening to detect the disease early that less invasive treatment options with significantly improved cosmesis became available. Breast conserving surgery (lumpectomy) combined with radiation therapy has been demonstrated to be an effective option for woman with early-stage breast cancer and is now standard of care [3, 18, 21, 25]. Due to the high volume of breast cancer patents, various treatments have been developed in order to provide adjuvant radiation in a more effective and reliable manner.

1.2.1 Accelerated Partial Breast Irradiation

Whole breast irradiation (WBI) is the principle technique of adjuvant radiation used in breast conserving therapy. EBRT is used to effectively provide coverage to the breast over a fractioned schedule of 5-7 weeks. However, the duration of treatment may be difficult to manage and can result in some patients refusing radiation or opting instead for mastectomy [6, 7, 11, 25, 26]. Additionally, the majority of recurrences in the breast after lumpectomy have been observed to occur within the immediate

vicinity of the lumpectomy cavity, and therefore WBI potentially irradiates more normal breast tissue than necessary, although this is currently a debated topic [5, 6, 25, 27–29]. The aim for treatments with reduced schedules, lower resource demands, and lower dose to healthy tissue has lead to the investigation of accelerated partial breast irradiation (APBI).

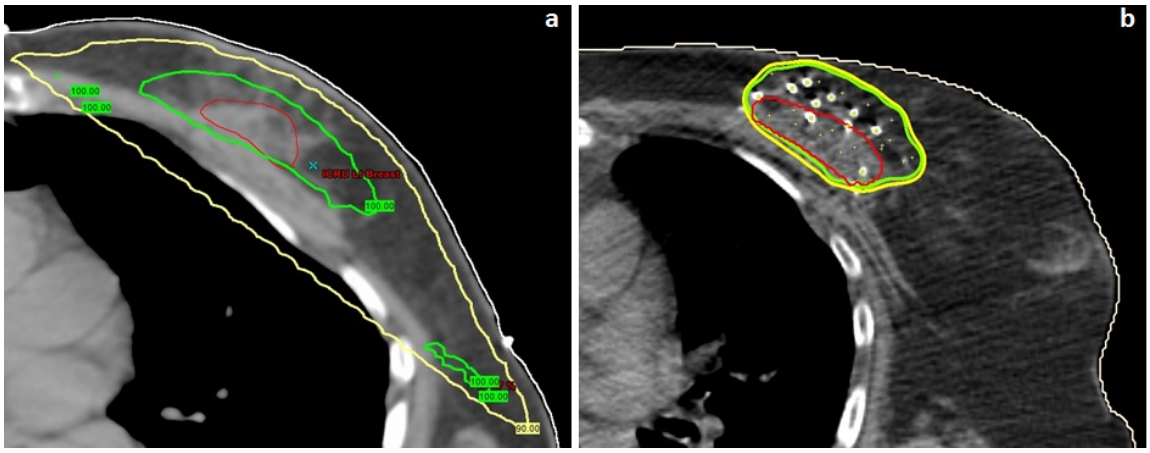

Figure 1.4: Comparison of the dose distributions from (a) a whole breast EBRT treatment plan and (b) the resulting dose distribution from an APBI treatment. The 100% (green) and 90% (yellow) doses are confined to a much smaller area around the seroma (red) in the APBI treatment.

APBI delivers curative doses of radiation only to the post-lumpectomy cavity (seroma) region plus the margin. The conformal dose distributions can provide a sufficiently high dose to the target while reducing exposure to the skin and remaining breast tissue (Figure 1.4), allowing for greater doses per fraction and expedited treatment schedules compared to WBI. A variety of methods of APBI have been successfully implemented, including hypo-fractionated conformal EBRT and HDR brachytherapy (Section 2.3.3), each with the aim of reducing treatment schedules to less than 1 week [5–7, 25, 27]. However, APBI is restricted by the size, staging, and location of the disease, depending on the treatment type, and is not yet widely available as a treatment option. Although APBI has been shown to achieve outcomes equivalent to WBI in early studies, current guidelines recommend treating only low risk patients with small (less than 3 cm diameter) primary tumours until large scale clinical trial data is available [6, 7, 25, 28, 30]. In order to make APBI more accessible, researchers and physicians aim to develop more safe and effective methods to deliver highly conformal doses to the target area with minimal resources and invasiveness.

1.2.2 Introduction to Permanent Breast Seed Implants

A recent development in partial breast irradiation is the permanent breast seed implant (PBSI) brachytherapy technique [8]. Recognizing the volume of breast cancer patients, the increasing popularity of partial breast irradiation techniques, and the success of LDR prostate brachytherapy (Section 2.3.2), PBSI was proposed by Pignol *et al.* as a method to further limit the treatment burden and resources of breast RT [8]. PBSI was designed, similar to prostate brachytherapy, to provide a dose to a target volume by permanently implanting radioactive sources (seeds) into and around the seroma. The seeds would provide the adequate dose to the seroma and margins to prevent recurrences using the principles of APBI, while limiting the dose delivered to the skin and breast. The primary advantage of PBSI over other forms of breast RT is that the treatment could be completed in a single day with a rapid return to normal quality of life, thus significantly reducing the burden of treatment and potentially making treatment more accessible for patients.

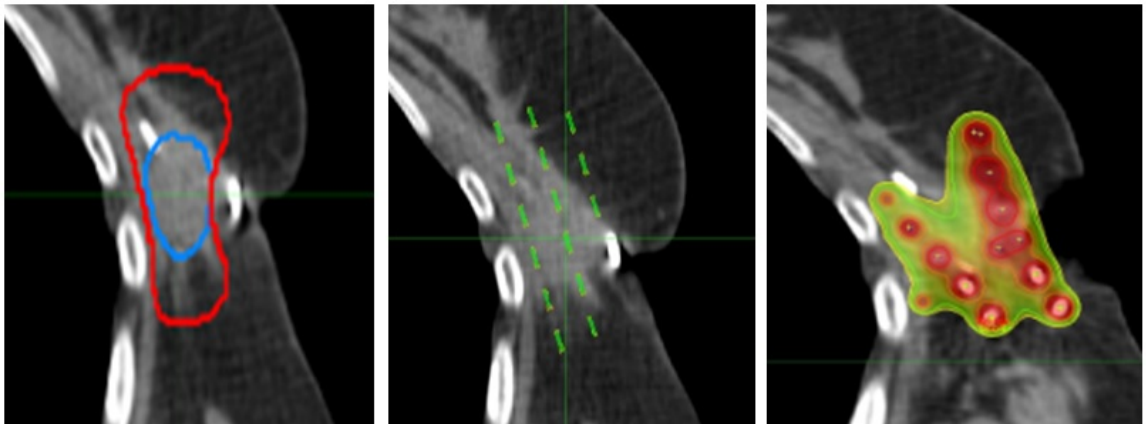

Figure 1.5: The contoured CTV (blue) and PTV (red) within the breast (left), planned the seed distribution throughout the volume (center), and the post-implant dose distribution from the implanted seeds (right). Green represents the regions receiving 100% of the prescription dose, and the high dose (200%) region is red.

PBSI uses palladium-103 (^{103}Pd) seeds (Section 2.1.3) to irradiate the seroma and surrounding tissue [31]. CT imaging is performed similar to the EBRT simulation procedure and the needle positions are planned to provide optimal coverage to the seroma (CTV) and surrounding margin (PTV). A detailed description of the planning procedure is provided in Section 2.4.2. During this procedure, setup is guided by free-hand ultrasound (US) and a fiducial needle which centres the treatment template (Concure Oncology, Mercer Island, WA) and can be visualized on US as a reference

for the loaded needle positions during the implant (Figure 1.6) [32]. The aim of the procedure is to deposit the seeds at their planned locations in order to provide the prescribed dose to the seroma and margins.

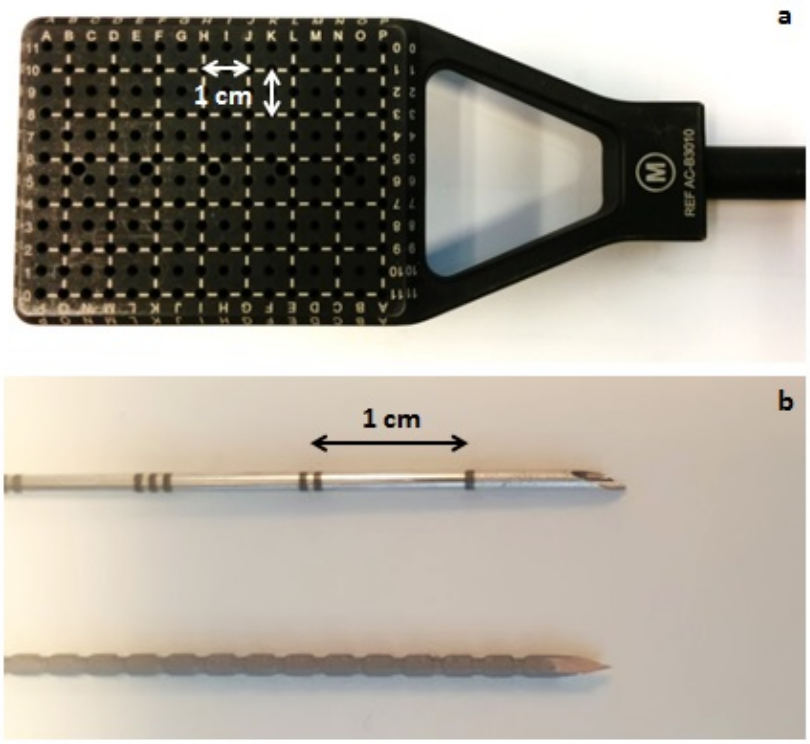

Figure 1.6: (a) The template used for PBSI treatments featuring a grid of holes (5 mm spacing) for needle insertion. (b) A bevelled needled used for depositing seeds (top) and a fiducial needle used to assist in guidance (bottom).

Early clinical trials showed promising results from PBSI, achieving successful target volume coverage, minimal skin toxicity and low local recurrence rates, and excellent patient satisfaction [8, 9, 33]. A comprehensive evaluation of 134 PBSI patients by Pignol *et al.* over a mean 63 month follow up period reported similar results, with an overall local recurrence rate of 1.2%, equivalent to that seen in patients who receive WBI [10]. The early success of PBSI, combined with the convenience of a single day procedure, has made this treatment an attractive option for patients with early-stage breast cancer.

1.2.3 Technical Challenges

Implementation of PBSI would potentially introduce a safe, effective, and favourable treatment option for breast cancer patients, but the procedure has not yet been widely adopted. Beyond the initial implementation at the Sunnybrook Health Sciences Centre [8, 10, 33], no additional developments were made and PBSI was only adopted by few sites for a limited number of cases. Although analogous to prostate brachytherapy, technical challenges in planning and delivery, along with the lack of a standardized procedure make it difficult to transfer and implement. Additionally, an initial learning curve was identified [8]. Godinez *et al.* expressed criticisms of the originally proposed procedure in 2006, doubting the clinical validity of the treatment based on the accuracy of target volume identification and seed placement, deeming the PBSI procedure to be a "potentially hazardous treatment alternative for breast cancer" [34]. To date, theses concerns have not been addressed.

PBSI has recently been introduced at the BC Cancer Agency - Centre for the Southern Interior (CSI) in an ongoing feasibility trial as only the second institution worldwide to offer the procedure [35]. During the trial period, several unique technical challenges have been identified. Among these, the treatment is based on the definition of the seroma in planning, which is performed on CT images, but US is used to guide the implant based on the seroma observed in the OR. Due to uncertainties in the target visualization, especially related to the known visualization differences between the two modalities (discussed in detail in Chapter 5) as seen in Figure 1.7a, the treatment plan may not accurately translate to the OR, requiring intra-operative adjustments to be made in order to treat the seroma visualized during implant. Additionally, guidance is based on 2D free-hand US, which lacks the rigid spatial registration of the template and image used in prostate brachytherapy. Real-time feedback on needle positioning is not available, making it difficult to ensure that needles end up in their planned positions, especially for peripheral needles where the fiducial and seroma are not visible as a guide (Figure 1.7b). Due to the challenges in visualization, setup, and needle insertion, the success of the procedure relies heavily on the skills and interpretations of the delivering oncologist and is susceptible to errors in the delivery, thus impeding the potential benefits of PBSI. In order to facilitate implementation, uncertainties throughout the procedure, and the methods required to reduce them, must be identified.

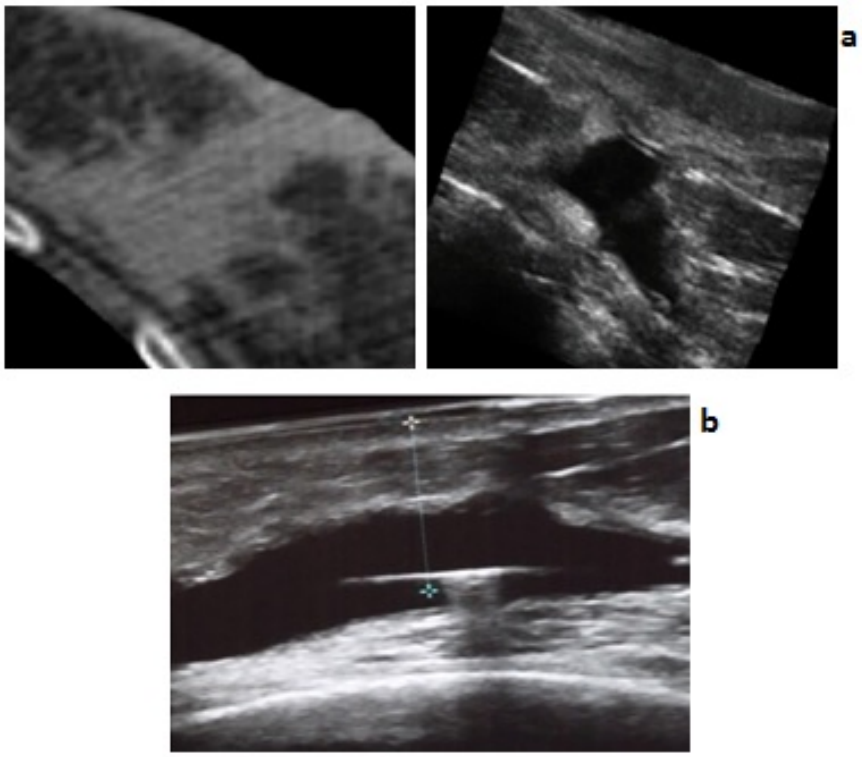

Figure 1.7: Deficiencies in imaging for PBSI. (a) Visualization of the same seroma visualized on CT (left) and US (right) may appear different in terms of size and shape. (b) The fiducial needle inserted through the center of the seroma, visualized on US, using only subjective interpretation of the surrounding anatomy as a guide. No spatial information relative to the template is available.

1.3 Dissertation Scope

The impact and prevalence of breast cancer necessitates treatments that can be completed safely, accurately, and reliably while limiting the required resources and burden of treatment. PBSI, a novel form of breast conserving therapy, has the potential to achieve these goals by accommodating successful partial breast radiation therapy in a single-day procedure. Many woman may potentially benefit from this procedure, but widespread adoption has currently been limited. The lack of implementation has therefore impeded the potential benefits of the procedure that may not be realised until PBSI has become standardized. Uncertainties relating to planning, visualization, and delivery, deficiencies in imaging, and the lack of a quantifiable procedure make the technique susceptible to errors and highly-user dependent. The objectives of this work are to identify and quantify the uncertainties in the current PBSI proce-

dure and determine their impact on the treatment. By revealing the magnitude and impact of errors on the procedure, methods to ameliorate the issues will be developed to increase the accuracy of PBSI and facilitate implementation.

This dissertation presents the work that was performed to assess uncertainties and innovate in each phase of the PBSI procedure: treatment planning, delivery, and post-implant verification. The following chapter provides background information into the principles of radiation therapy physics and radioactivity that are fundamental to brachytherapy, as well as the components of modern brachytherapy treatments that are relevant to the PBSI procedure. Chapter 3 describes the materials and methods that were used throughout the research, from the assessment of seed placement to the evaluation of seromas with 3DUS. The design of a novel 3DUS scanning system specifically for PBSI is also outlined.

In order to determine potential improvements that could be made in the PBSI procedure, the sources of uncertainty and their relative impact on the treatment must first be defined. By assessing the accuracy of seed placement in the current procedure, any systematic errors in the delivery can be identified. Chapter 4 describes the comprehensive evaluation of seed placement accuracy in a cohort of PBSI treatments, and the resulting effects on treatment dosimetry. The assessment highlights the magnitude of placement errors in the delivery and identifies the potential sources of errors which may subsequently be ameliorated through additional developments in the procedure. The planning and delivery process in PBSI using CT and US is hypothesised to be a major contributing factor to set up and seed placement errors in PBSI. The differences between the modalities, in relation to PBSI treatments, are thoroughly examined in Chapter 5. PBSI treatment plans are used to evaluate the dosimetric effects of visualization differences and the resulting potential for intra-operative set up adjustments, affecting the accuracy of the treatment. Based on this evaluation, methods for incorporating 3DUS into the planning procedure are explored.

The impact of improved visualization in treatment planning on the treatment can be quantified by examining the relationship between seroma delineation and seed placement accuracy. Chapter 6 presents an assessment of seroma delineation uncertainties on CT and US, within PBSI treatments. Correlations between the visualization and seed placement accuracy identifies the sources of error that can be reduced in the procedure through improved visualization in planning. However, improved visualization in treatment planning only reduces a component of uncertainty of the PBSI procedure. Random errors during the delivery may only be reduced through

improved intra-operative guidance. In Chapter 7, the benefits of needle guidance are explored. The initial characterization of a novel 3DUS image guidance system is presented, and the potential impact on seed placement accuracy, relative to the current procedure is evaluated. A final discussion and conclusions of the work are given in Chapter 8, along with future considerations of developments for PBSI.

Several clinical and research groups were involved in the presented work, with the overall study designs, development, data collection, and analysis performed by the dissertation's author. PBSI data was collected from implants performed by the clinical PBSI team at BCCA - CSI. Retrospective analysis of the clinical implants was performed for the studies in chapters 4 and 6, independent of the clinical procedure. The images used for the study in Chapter 5 were acquired from a previous study by Berrang *et al.* [36], with subsequent planning simulation and analysis performed by the presenting author. In Chapter 6, the 3DUS system was reconstructed and maintained for patient imaging by the author, who also coordinated and analysed the image acquisition and contouring performed by radiation oncologists. The 3DUS system used in Chapter 7 was developed and commissioned at The Imaging Research Laboratory (Robarts Research Institute, Western University) with guidance from the CSI PBSI research group to create a system unique to our implant procedure. The experiments, measurements, and analysis presented in Chapter 7 were designed and performed by the dissertation's author, with support from the developers, to characterize the system and it's potential accuracy and impact in a clinical setting, while the final simulated implants were performed by an expert brachytherapy oncologist.

Chapter 2

Background

The presented work aims to evaluate the current PBSI procedure to quantify uncertainties in both treatment planning and delivery, and to develop the methods required to reduce them. This chapter describes the principles of radiation physics that are fundamental to brachytherapy, including the source of radiation and its interaction with matter. The physics of the medical imaging procedures used throughout this work will be described, as well as the principles of brachytherapy planning and delivery. Finally, a comprehensive overview of PBSI, from patient selection to recent developments, is presented.

2.1 Radiation Therapy Physics

Brachytherapy treatments are based on the fundamental principles of radiation therapy physics. The interactions of high energy photons and electrons with matter are ultimately responsible for depositing the dose that leads to cellular death. The properties of radioactive decay allow for these interactions to occur from within the tissue without having to travel from an external source.

2.1.1 Interactions of Radiation with Matter

Photon Interactions

High-energy photons used for imaging and RT can undergo a variety of different types of interactions as they travel through a medium, as shown in Figure 2.1. The majority of interactions result in the removal of an orbital electron from the atom,

or ionization. One of the dominant interactions that occurs at energies relevant to imaging and brachytherapy is the Compton effect, the collision between a photon and electron. Compton interactions occur when the photon's energy is significantly greater than the binding energy of the electron, and therefore primarily occurs with outer shell, essentially free, electrons. Figure 2.1 shows a photon with incident energy E_1 colliding with an electron e_1^-. The electron receives energy from the collision and is ejected from the atom at an angle ϕ, while the photon is scattered at angle θ with a reduced energy E_f.

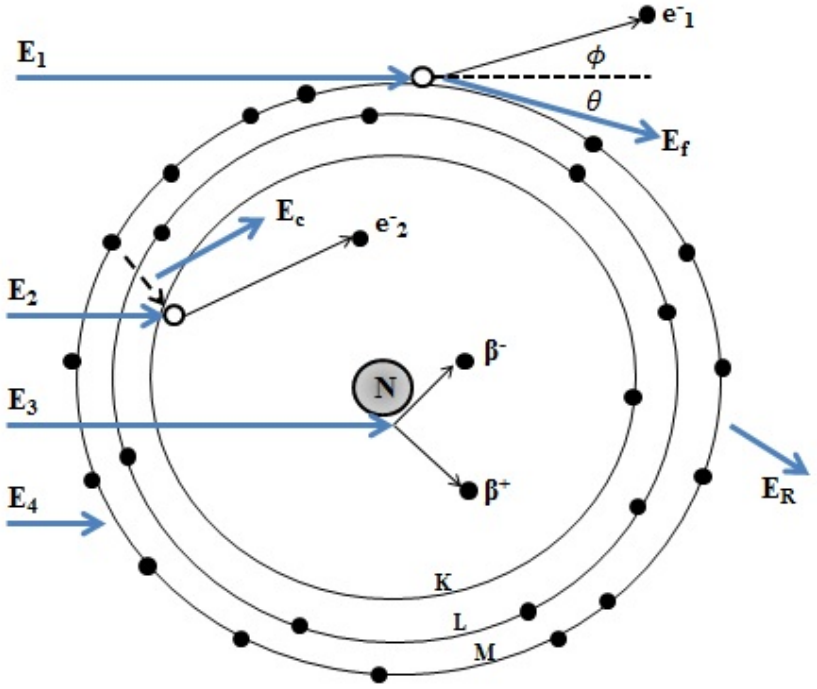

Figure 2.1: Interactions of high-energy photons with matter. Photon E_1 undergoes Compton scattering with an outer shell electron e^-_1. E_2 is absorbed in a photoelectric interaction, ejecting electron e^-_2 and a characteristic x-ray (E_c) is produced. E_3 interacts with the electromagnetic field of the nucleus (N), producing the electron positron pair, β^- and β^+. The interaction of E_4 with the atom produces the Rayleigh scatted photon E_R.

The second principle interaction to occur within the energy range of imaging and brachytherapy is the photoelectric effect. A photon interacts with an atom and its energy is completely absorbed and transferred to an orbital electron. The electron is ejected with kinetic energy equal to the difference between the incident photon energy and the binding energy of the electron shell. Therefore, the photon's energy must be

greater than the binding energy of the electron in order for photoelectric interactions to occur. However, the closer an electron's binding energy is to the photon's energy, the higher probability that it will be ejected [37].

The ejected electron creates a vacancy in the shell, which can subsequently be filled by an electron from an outer shell. In Figure 2.1, the hole left by the ejection of electron e^-_2 is filled by an electron from the M-shell, creating a characteristic x-ray, with energy E_c equal to the difference between the two binding energies. This process can cascade to the outer shells until a vacancy is filled by a free electron [38]. A K-shell vacancy filled by an adjacent electron produces a K_α x-ray, and from a non-adjacent shell produces a higher energy K_β x-ray. Characteristic x-rays are named from unique spectrum of energies produced by each energy level in every element. Even within the same shell, binding energies of the electrons vary slightly, resulting in a spectrum of K_α and K_β emissions.

When a photon interacts with the electromagnetic field of the nucleus, the process of pair production may occur. The photon's energy is entirely absorbed and converted into an electron-positron pair (Figure 2.1). The rest mass energy of electrons and positrons is 511 keV, and therefore the minimum photon energy required for pair production to occur is 1.022 MeV. The γ-rays produced by brachytherapy sources are rarely above the 1.022 MeV threshold, or not at all in ^{125}I and ^{103}Pd (Section 2.1.3), and therefore pair-production is not a primary interaction in brachytherapy.

The remaining photon interaction is Rayleigh (coherent) scattering. Primarily at low energies, the photon can interact with the whole atom, causing the electrons to oscillate and re-emit energy, resulting in the emission of a photon with energy equal to the incident photon's in a slightly different direction [38]. Electrons are not ejected and therefore ionization does not occur. Rayleigh scattering predominately occurs with photons in the 10 - 70 keV range, but interaction probability is low in tissue, accounting for at most 12% of interactions at 30 keV.

The probability of the different types of interactions occurring depends on a variety of factors. Compton event probability in a medium is related to the electron density of the material, while Rayleigh, pair production and photoelectric interactions are related to the atomic number (Z) [37]. The energy of the incident photon is a strong determining factor of the interaction type, with the photoelectric effect dominating under 30 keV (in water), after which Compton scattering becomes the primary interaction until the pair production threshold is met [39]. The total probability of any interaction occurring at any energy is expressed by the attenuation coefficient of

the material.

Electron Interactions

As electrons travel though a medium, they undergo a variety of different interactions resulting in excitation, ionization, and radiative loses. Excitation and ionization occur through the electromagnetic interactions of electrons causing the transfer of a portion of the electron's energy to an orbital electron [37]. When the energy transferred is not sufficient to eject an electron, the orbital electron is raised to a higher-energy level (excitation) and then returns to lower energy level (de-excitation), re-emitting the excitation energy. With sufficiently high transferred energy, exceeding the binding energy, the orbital electron may be ejected from the atom resulting in an ion pair, the negatively charged ejected electron and the positively charged atom. The incident electron may continue to interact throughout the medium. The ejected electron, with kinetic energy equal to the difference in the energy transferred and the binding energy of the shell, may also possess sufficient energy to produce further secondary ionizations, and are called delta-rays.

After an electron is ejected from its shell, the vacancy may be filled from an electron of a higher energy level, resulting in characteristic x-ray production, as described above. The excess transition energy may instead be transferred to another orbital electron, called an Auger electron [38]. This electron will subsequently be ejected with energy equal to the difference between the transition energy and binding energy of the shell. Auger emission predominantly occurs over characteristic x-ray production in low Z elements, like those found in the majority of soft tissue, and therefore are an important component of dose deposition [38].

When an electron travels close to atomic nuclei and is decelerated by the positive charge, the electron radiates energy equal to the loss of kinetic energy [38]. The energy is emitted as a bremsstrahlung x-ray which will proceed to interact via the processes described above. The electron, if energy remains will continue to interact throughout the medium. While bremsstrahlung emissions are essential for the creation of x-rays in imaging and RT, the process of ionization is what ultimately results in the biological damage to cells.

Radiation Dose

The concept of radiation dose relates to the amount of energy that is transferred to a medium through ionizing radiation and is a measure of its biological effects. Dose is measured in units of grays (Gy) where 1 Gy is equivalent to 1 J of energy imparted to 1 kg of matter. The quantity KERMA (kinetic energy released in the medium) is used to quantify the energy transferred to a medium by the incident radiation, or the total kinetic energy of the initial charged particles [37]. The combined effects of the initial interactions, ionizations, and secondary electron ionizations result in the absorbed dose to the medium. Due to the range of electron motion, dose can be deposited at a point far from the initial site of interaction [37]. Electrons lose energy through their combined interactive processes over a short distance, with rapid loses occurring at lower energies, or near the end of an electron track [39]. Therefore, at lower energies, electrons deposit dose close to the site of initial interaction. For example, all interactions of a 80 keV electron will occur within approximately 0.1 mm in tissue before it comes to rest [39].

The dose of radiation is directly related to the number of significant damages to cellular DNA that may occur, and thus ultimately lead to the death of a cell. In general, 1 Gy of radiation dose will result in approximately 100 000 ionizations in a cell. Of these ionizations only about 2000 will result in damage to the DNA, with only around 20-40 significant double strand breaks occurring which can potentially lead to cellular death [17].

2.1.2 Radioactive Decay

An unstable atom undergoes radioactive decay to achieve a stable state, emitting radiation in the process. Decay can occur in several different ways, and a series of different decays may occur before the atom reaches a stable state. The process of radioactive decay emits a spectrum of radiation at various energies with dose rates unique to each radionuclide, some appropriate for various types of medical applications.

The activity (A) of material is described by the change in the total number of atoms (N) in a time (t) by a radioactive process [37]

$$A = -dN/dt. \tag{2.1}$$

The change in the number of atoms is related to the total number of atoms by the decay constant, λ, of the atom

$$-\frac{dN}{dt} = \lambda N. \tag{2.2}$$

Therefore, the activity at any time (A_t) can be expressed as

$$A_t = A_o e^{-\lambda t} \tag{2.3}$$

where A_o is the initial activity at time t_o. An important concept in defining the activity of a material is the half life ($T_{1/2}$), which describes the time it takes for the activity or number of atoms to reduce by half ($A/A_o = 0.5$) and can be calculated from the decay constant by

$$T_{1/2} = \frac{ln2}{\lambda}. \tag{2.4}$$

When an atom decays it gives rise to a daughter atom. If the daughter is stable, the decay process ends, otherwise the atom will continue to decay until a stable state is reached. Decay to an excited daughter atom often results in the emission of excess energy to achieve a lower energy state in the form of gamma (γ) rays. De-excitation may also result in the formation of an internal conversion electron, where the excess energy is transferred to an orbital electron that is ejected from the atom with kinetic energy equal to the difference of the γ-ray and binding energies [37]. The vacancy in the shell can be filled by the processes described in Section 2.1.1, producing characteristic x-rays or Auger electrons. The total decay process of an atom through several levels to a stable state can therefore result in the production of a wide spectrum of different photon and electron energies, unique to the decaying material.

There are multiple different forms of decay that may occur depending on the properties of the atom. The primary methods of decay are alpha, beta-minus and beta-plus (positron) emissions, electron capture, and isometric transitions. Generally, the decay processes result in the production of a proton or neutron in order to achieve a stable neutron-to-proton ratio [37]. Low energy brachytherapy sources such as ^{125}I (28 keV) and ^{103}Pd (21 keV) tend to decay by electron capture (EC) [21]. EC occurs when a neutron deficient nucleus captures an orbital electron and converts a proton into a neutron, emitting excess energy, as described by

$${}^{A}_{Z}X + e^{-} \rightarrow {}_{Z-1}{}^{A}Y + neutrino + energy \tag{2.5}$$

where X and Y are the parent and daughter atoms with mass number A and atomic number Z and $Z-1$, respectively [37]. With the removal of a proton and creation of a neutron, the atomic number decreases and the mass stays the same. EC primarily captures a K-shell electron due to their closer proximity to the nucleus, but capture from other shells is possible. Due to the missing electron, the vacancy is filled by a bound electron from a higher energy shell, producing characteristic x-rays and Auger electrons. As the name implies, an electron is captured in every EC decaying atom, although not necessarily the same one. The subsequent K_α and K_β x-rays can therefore account for a significant portion of the resulting x-ray spectrum.

2.1.3 Palladium-103

Many different types of radionuclides are used in modern brachytherapy, as briefly discussed in Section 1.1.3, primarily based on the emitted energy and dose rate. Palladium-103 (^{103}Pd) is the isotope used in permanent breast seed implants (PBSI). Production of ^{103}Pd can occur in a nuclear reactor where stable ^{102}Pd captures a thermal neutron, or in a cyclotron by bombarding a rhodium (Rh) target with protons [21]. ^{103}Pd decays by EC with a half life of 16.99 days ($\lambda = 0.0408$ d^{-1}) into the excited state of ^{103m}Rh. During the decay to ^{103m}Rh, a total of 8 different γ rays (mean energy of 359.6 keV) may be emitted, and further de-excitation to the ground state of ^{103}Rh emits an additional 39.8 keV γ ray. Through the decay, and as a result of the processes described in Section 2.1.2, a spectrum of 40 characteristic x-rays (mean energy of 1.6 keV), 48 internal conversion electrons (mean 108.6 keV), and 11 Auger electrons (mean 782 eV) may be produced, and an additional spectrum of low energy ($<$ 1 keV) x-rays and electrons are produced in the de-excitation [21]. The majority of the resulting photons and electrons have a very small energy, likely attenuated within the seed itself, and offer no value to treatments. The resulting spectra, removing energies below 5 keV, has a weighted mean photon energy of 20.7 keV, and electron energy of 32.6 keV [21]. As shown in Figure 2.2, approximately 77% of the total resulting photons have energies between 20-23 keV [40, 41]. These photons are K_α and K_β characteristic x-rays resulting from vacancies in the K-shell from the EC process being filled by outer shell electrons, with the energies defined by the binding energies of Rh's shells. In contrast, the higher energy γ rays contribute to an insignificant portion of the overall spectrum. Therefore, ^{103}Pd is considered a low energy source, allowing it to be used for LDR brachytherapy [21].

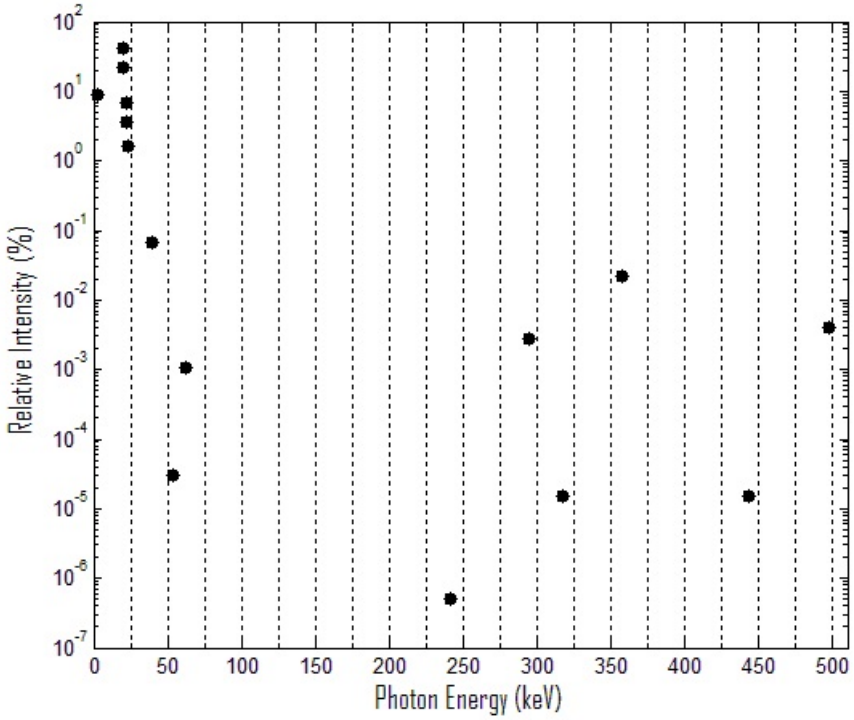

Figure 2.2: The discrete spectrum of photons emitted during the decay of ^{103}Pd to ^{103}Rh. The large number of photons with energies less than 5 keV have been omitted.

^{103}Pd was deemed to be the suitable isotope for PBSI by Keller *et al.* primarily due to the proximity of the implant to the skin surface [31]. The dose to OARs is important to consider when selecting an isotope for treatment, but PBSI presents a unique situation where other people besides the implanted patient are at risk of exposure. Unlike in prostate LDR brachytherapy, natural shielding from within the breast is low due to the relatively shallow implant depths, potentially resulting in high doses to the skin and beyond. Due to the lower energy, ^{103}Pd (mean energy = 20.7 keV) was found to provide significantly reduced dose to the skin surface and lower external exposure, to safe levels, compared to ^{125}I (mean energy = 28.4 keV) implants for PBSI [31]. ^{103}Pd may also provide a radiobiological advantage over ^{125}I due to the shorter half-life delivering the dose at a faster rate [37].

A schematic diagram of the ^{103}Pd seed used in PBSI, the Theraseed Model 200 (Theragenics, Buford, GA) is presented in Figure 2.3. The seed contains graphite pellets plated with ^{103}Pd inside of a tube made of titanium (0.06 mm thickness) [39]. A lead marker is placed in the centre of the seed in order to visualize the seed on CT

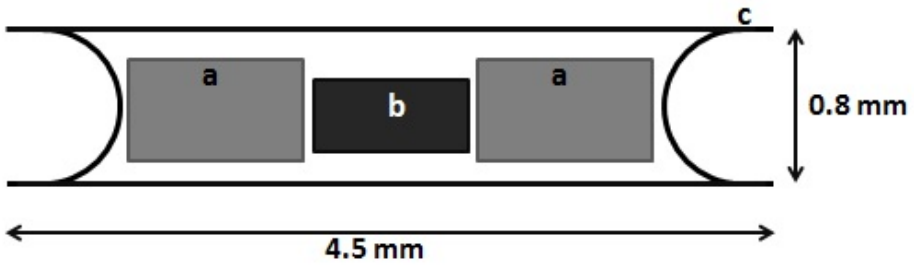

Figure 2.3: Schematic diagram of the Theragenics Theraseed 200 ^{103}Pd seed. (a) Graphite pellets are coated with ^{103}Pd and loaded on either side of (b) a lead marker and sealed in (c) a titanium capsule.

or radiographs. The seed is not an isotropic (point) source and therefore dose is not deposited uniformly around the seed. Absorption of photons and electrons by the wall, and within the seed itself, as well as the distribution of palladium in the seed results in a lower fluence along the axial direction of the seed [37, 39]. A description of this anisotropy and the role it plays in dose calculations is provided in Section 2.3.1.

2.2 Imaging for Brachytherapy

2.2.1 Computed Tomography

As discussed in Section 1.1.2, CT is the most widely used imaging modality for RT treatment planning as it provides a highly detailed 3D representation of a patient's anatomy. CT imaging involves the use of an x-ray source (a kV x-ray tube) that is continually rotated around the patient. The x-rays emitted from the source are attenuated as they travel through the patient, based on the interactions described in Section 2.1.1, and the resulting x-ray spectrum upon exit on the distal side is measured by a row of detectors [38]. The detection process results in a series of thin radiographic images which, when combined over all angles of acquisition, can be reconstructed into a single slice of the imaged volume. Continual acquisition of such slices produces a 3D volumetric image with voxel grey scale values directly related to the attenuation coefficients of the materials within the imaged volume, primarily relating to the electron density and atomic number, corresponding to the probability of Compton and photoelectric interactions, respectively. High contrast between different tissue types can therefore be achieved by differentiating between

small differences in the properties resulting in attenuation in the different materials [38].

CT images are useful for treatment planning because they offer the ability to image the patient in their planned treatment positioning in order to perform accurate dose calculations based on not only the attenuation properties but also the positioning of the anatomy. CT also provides means to accurately record patient positioning for later replication. In RT, lasers can be mounted in the room that intersect at a known distance outside of the scanner, corresponding to the treatment isocenter in the CT volume. The laser points on a patient's skin may be tattooed so the position can be accurately replicated by aligning similar lasers in the treatment room. Although highly useful for treatment simulations, patient exposure is to be considered due to the measurable radiation dose resulting from a CT scan [38].

2.2.2 Ultrasound Imaging

Ultrasound Physics

Sound is mechanical energy that propagates through a medium via a series of compressions and rarefractions (back and forth vibrations) of the particles within, creating a moving pressure wave. Compression of particles within a medium from an external force results in an increase in pressure. Following a compression, the particles transfer energy to adjacent particles with the reduction in local pressure, thus producing a sinusoidal pressure wave, characterized by its wavelength (λ) and frequency (f) [38]. Sound waves which propagate at frequencies between 15-20 kHz comprise the audible acoustic spectrum, and those greater than 20 kHz (cycles/second) are called ultrasound (US), with medical US using frequencies between 2 to 10 MHz [38]. Like other types of waves, sound waves may interact with each other and produce a composite wave. The interaction can result in series of constructive or destructive interference, either reinforcing or cancelling each other out. Short bursts of sound result in pulses of energy that will travel and interact according to the various acoustic properties of the material.

The speed of sound (c) varies widely across different mediums. A sound wave propagates according to the medium's compressibility, determined by the density (ρ), and bulk modulus (B), or the "stiffness" of the material. Media such as air have a very low speed of sound ($\sim$330 m/s) and dense, solid material like bone have a high speed of sound ($\sim$4080 m/s) [38]. The speed is also equal to the product of the

frequency and wavelength, and thus can be determined by

$$\sqrt{\frac{B}{\rho}} = c = \lambda f. \tag{2.6}$$

The difference between the speed of sound in different materials is fundamental to US imaging. As sound travels from one medium to another, changing the speed, the frequency remains constant and therefore changes the wavelength at the interface of the two media. The speed of sound is used to define the acoustic impedance, Z (kg/(m^{2}sec)), of a material by

$$Z = \rho c \tag{2.7}$$

where ρ is the density of the material in kg/m^3. As sound travels through a medium, minor variations in Z allow for the continued propagation of the sound wave, where larger differences (for example, from tissue to air) results in the reflection of the sound wave called an echo [38]. At an interface of two materials with impedances of Z_1 and Z_2, where the boundary is much larger than the US wavelength, the intensity reflection coefficient (R_I) is expressed as the ratio of the reflected and incident intensities (I_r and I_i respectively)

$$R_I = \frac{I_r}{I_i} = \left(\frac{Z_2 - Z_1}{Z_2 + Z_1}\right)^2 \tag{2.8}$$

where I is the power per unit area (W/cm^2) (Figure 2.4) [38]. Large differences in Z, such as from air ($Z = 0.0004 \times 10^6$) to water ($Z = 1.48 \times 10^6$), will result in nearly 100% of the indecent wave being reflected [38]. Therefore, medical US imaging is impossible without the assistance of an acoustic coupling gel due to the inevitable air gap that will exist between the US transducer (discussed below) and the skin surface. Smaller differences in Z, such as from fat ($Z = 1.38 \times 10^6$) to muscle ($Z = 1.71 \times 10^6$), result in only a portion of the incident wave being reflected [38]. The component of the signal that is not reflected will continue to propagate through the material. Reflection of the US beam is a critical component of US imaging as the time it takes for an echo to return is used to determine the location of tissue boundaries.

When the incident wave is travelling perpendicular to the boundary region, the transmission and reflection occur parallel to the incident direction. As shown in Figure 2.4, at oblique incidence at the boundary of materials with speeds of sound c_1

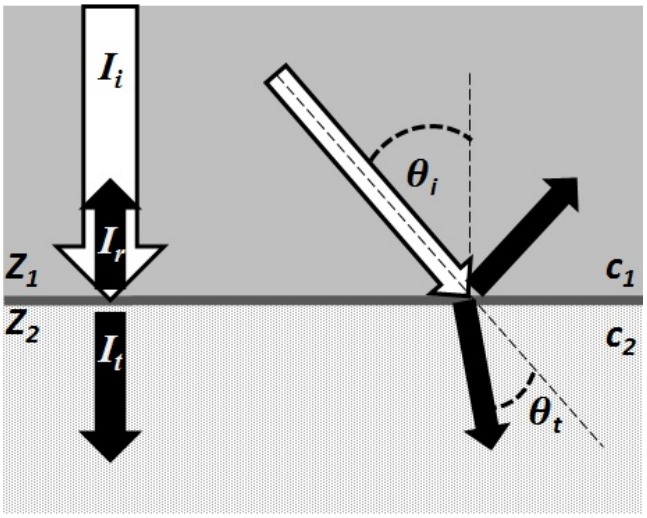

Figure 2.4: Incident ultrasound wave with intensity I_i is reflected at the boundary of materials with acoustic impedances of Z_1 and Z_2, causing a portion to be reflected (I_r) and transmitted (I_t). Non-perpendicular incidence results in reflection away from the incident wave and refraction of the transmitted component.

and c_2, the wave is refracted according to Snell's law

$$\frac{sin\theta_t}{sin\theta_i} = \frac{c_2}{c_1} \tag{2.9}$$

where θ_i is the angle of incidence and θ_i [38]. Specular reflection occurs at smooth boundaries where the size of the boundary is much greater than the wavelength of the sound.

Objects that are near the same size, or smaller, as the US wavelength represent a non-specular surface and result in acoustic scattering, reflecting the sound in all directions at a low amplitude (Figure 2.5a) [38]. While hypoechoic materials represent a near uniform medium where minimal reflections or scattering occur, hyperechoic materials have a large number of scatterers and often give rise to distinct scatter "signature" that characterize different tissues and is thus useful in diagnostic imaging [38]. As a US wave travels through a hyperechoic material, acoustic energy is lost as a result of this scattering, attenuating the signal (Figure 2.5b). Attenuation is also caused by the conversion of acoustic energy to heat in the tissue. Attenuation occurs exponentially with penetration depth and increases with increased frequency at a rate of approximately 0.5 (dB/cm)/MHz in soft tissue [38]. Therefore, the reflected signal from a boundary several centimetres deep is many times weaker than a similar signal

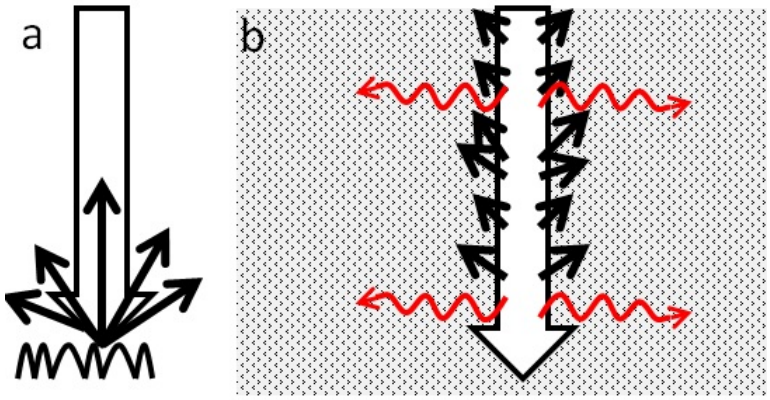

Figure 2.5: (a) Ultrasound interaction with a non-specular boundary results in diffuse reflection. (b) As an US beam travels through a hyperechoic medium, it interacts with small particles causing small scattered echos, and loses energy to heat (red), resulting in attenuation.

reflected closer to the surface, hence more difficult to detect.

Image Formation

Ultrasound images are acquired using an US probe (transducer) that is placed on the surface of the material, usually assisted by a viscous coupling gel with a speed of sound similar to tissue in order to limit the reflection at the air-transducer interface. The US probe contains an array of piezoelectric crystals which are used to generate and detect the US waves. Piezoelectric materials contain a uniform arrangement of electrical dipoles, synthetically created by heating to a high temperature and applying an external voltage while the material cools to maintain the diople orientation [38]. An applied alternating voltage to a piezoelectric element causes the physical deformation and oscillation of the crystal by forcing the dipoles to realign, converting the electrical energy into mechanical (sound) energy [21, 38]. Conversely, applying mechanical pressure to the crystal results in the formation of a surface charge and thus an induced electrical signal, as shown in Figure 2.6.

Short ($\sim$1 μsec) burst of voltage are applied to the piezoelectric elements in a transducer, forcing them to expand and contract at the frequency the voltage is applied, creating an US pulse. A matching layer covering the elements minimizes the difference in acoustic impedance, and hence reflections, between the transducer and tissue surface (or coupling gel). After the pulse is produced, the transducer switches to a "listening" mode in which incoming mechanical pulses are converted

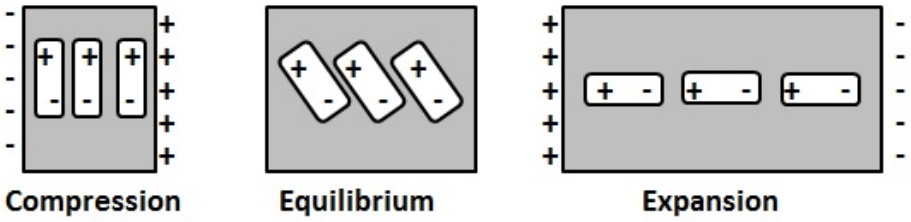

Figure 2.6: At equilibrium the piezoelectric element has no net surface charge. Under the influence of mechanical pressure the element contracts or expands, causing the dipoles within to re-arrange and produce a surface charge. An external voltage causes the element to expand and contract in an opposing manner.

to a proportional electric signal. The amplitude of the returning signal is generally much smaller than the initial pulse, often orders of magnitude due to the intensity of reflection and attenuation. Therefore, the analog signal is subsequently amplified, converted to a digital signal, processed and filtered in order to be displayed [38]. The duration of listening depends on the desired depth to be measured. Sound takes approximately 13 μsec per cm of depth of tissue to return to the transducer (from Equation 2.10), and another pulse will not be produced until the initial pulse has adequate time to return [38].

The pulse travels through a medium until it interacts with a boundary, causing a portion of the signal to be reflected back to the transducer which is subsequently detected. The digital signal, proportional to the amplitude of the echo, is generated as a function of the time it takes for the echo to return (A-mode). The time (t) it take for the echo to return can be used to determine the distance (d) between the transducer and the reflecting object, based on the speed of sound in tissue (assumed to be $\backsim$1540 m/s)

$$d = \frac{c \times t}{2} \tag{2.10}$$

where the factor of 2 is due to the total distance representing a return trip of the pulse from the transducer to the boundary region. The A-mode signal can therefore be localized and converted to a brightness signal (B-mode), displayed as a series of points along a scaled distance [38]. Distances between different levels of brightness represent changes in the medium in the path of the US pulse. Subsequent pulses are produced along the length of the transducer, offset by several individual elements, after the previous signal has been detected with the successive collection of the B-mode signals along the total length creating a 2D image (Figure 2.7). The pulse

repetition period, or the time is takes to generate, listen, and display a pulse, is on the order of 100-200 μsecs, allowing for 20-100 2D images to be produced per second, depending on the resolution and depth of imaging, and thus the images are essentially displayed in real time [38].

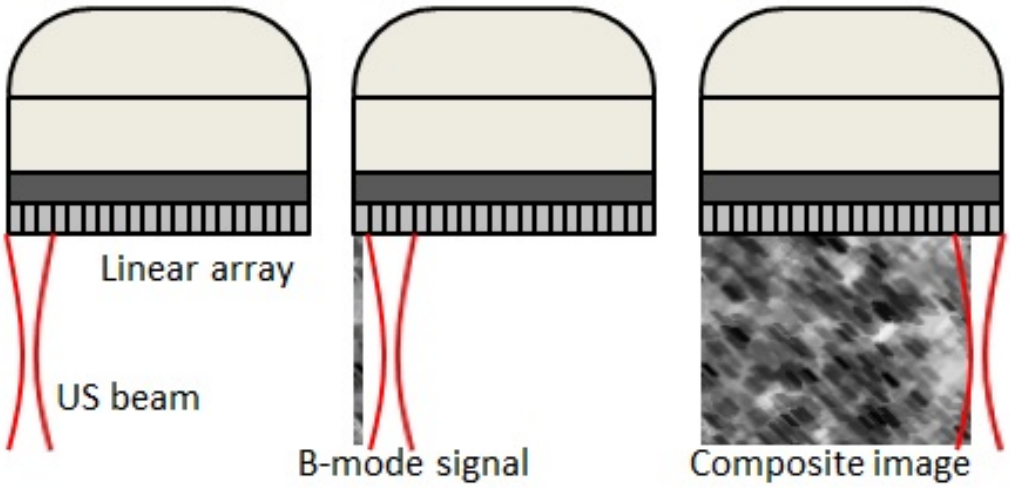

Figure 2.7: A group of piezoelectric elements in a linear array are activated, resulting in a narrow converging/diverging ultrasound beam traversing and returning through the medium and generating a single A-line, converted into a B-mode signal. Subsequent activation of groups of elements results in additional B-mode signals across the array until a composite rectangular image is produced.

Modern US transducers consist of an array of piezoelectric elements (generally 128 to 512) with individual widths of less than half of the US wavelength [38]. Linear and curvilinear arrays operate by activating a group of approximately 20 adjacent elements to produce an US beam. Echoes are detected before another group of elements, displaced by one or two elements, is activated with continual acquisition resulting in a 2D image, as shown in Figure 2.7. Phased arrays activate all elements nearly simultaneously to produce a single narrow beam. Images from phased arrays are acquired along the length of the transducer by continually adjusting the delay between individual element activation, causing the resulting beams to be produced at slightly different angles which are then detected and combined. Due to the constructive and destructive interference of the waves produced by the individual elements, the resulting beam converges out to a distance defined by the diameter of a single element, or effective diameter of the group of activated elements, and the frequency [38]. After the focal zone, where lateral resolution is greatest, the beam proceeds to diverge. The length of the converging field (the near field), and thus the focal distance can

be adjusted by changing the number of simultaneously active elements in order to reduce the effective diameter in a linear array, or by adjusting the time delays in the discrete elements in a phased array.

Image Resolution and Artifacts

Good image quality is essential for interpreting US images and being able to accurately localize small objects within an imaged volume. Contrast in an image, or the ability to distinguish between different types of material, is highly dependent on the ability of the system to detect a range of echos, and also to filter out low amplitude signals. As discussed above, reflections produce the signal in an image and the scatter signatures of different tissues provide context to the materials being observed. Therefore, contrast primarily depends on the density and size of scatterers within different materials [38]. From Equation 2.8, the interface of materials with similar speeds of sound can result in a very low amplitude reflection that must be detected and appropriately amplified in order to produce a signal. Alternatively, very low signals, from very low intensity scattering and even electronic fluctuations, must be filtered out to prevent excessive noise in the image [38]. In modern US systems, the display range can be adjusted to remove low-intensity signals, reducing the noise in the image.

The spatial resolution determines the ability to distinguish small closely spaced objects in an image. The spatial resolution in US images is primarily dictated by the size of the US pulse. The wavelength determines the spatial resolution in the direction of the beam (axial). An US pulse is produced by multiple (typically 3) cycles that travel through the medium together, separated by a distance called the spatial pulse length (SPL), determined by the wavelength and number of cycles [38]. Boundaries separated by less than 1/2 the SPL will result in echoes that overlap, limiting the axial resolution. Therefore a high frequency US, reducing the wavelength and thus SPL, provides a higher resolution, but the depth of penetration is reduced due to the attenuation [38]. Resolution in the lateral direction, or perpendicular to the beam direction in a 2D image, is limited by the width of the piezoelectric element and the effective width of the US beam. Therefore, the best lateral resolution occurs in the near field, due to the decreasing beam width, and may be improved by re-grouping elements and taking multiple scans while only accepting signals from the focal zones [38]. Similarly, the height of the piezoelectric elements may cause small objects to be missed in the elevational direction, perpendicular to the plane of imaging. Elevational

resolution is important in 3DUS image reconstruction (Section 2.2.3). During volume acquisition, while scanning along the elevational direction, increased slice thickness results in gaps in the volumetric data that are filled through interpolation of the adjacent data, contributing to blurring artifacts or causing small objects in between slices to be missed.

Several artifacts are common in US imaging, demonstrated in Figure 2.8. Shadowing occurs when the beam travels through a highly attenuating material, such as bone, or a highly reflecting interface, such as tissue to air, resulting in a low intensity streak beyond the object due to a loss of signal [38]. Due do the magnitude of reflection occurring at air interfaces, good contact between the transducer and tissue is imperative to the acquisition of high quality US images. Reverberations may form from multiple reflections of the same beam between two highly reflecting materials. The back and forth reflections will ultimately appear as a series of bright spots or lines in the resulting image when they are finally detected due to the increased time that it takes for them to return to the transducer [38].

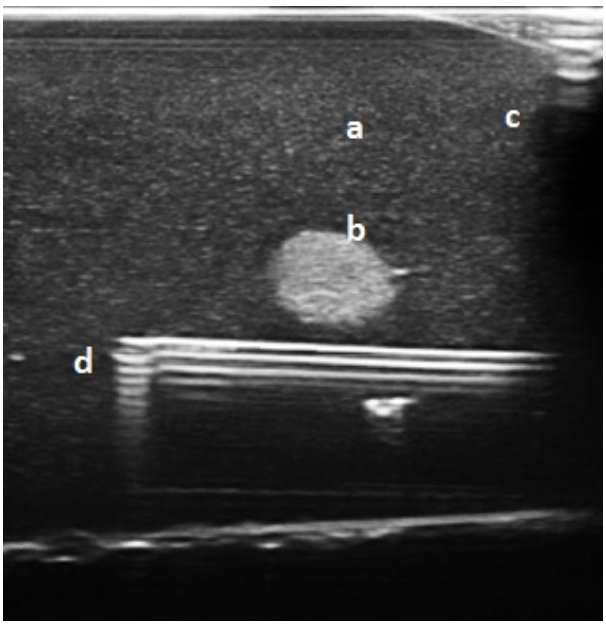

Figure 2.8: An US image of a needle inside of a phantom. (a) The background signal is produced by the scatterers in the material. (b) When the US beam travels into a different hyperechoic material, clear contrast is produced. (c) Poor contact of the transducer with the surface produces a bright blur from the high intensity reflection followed by the loss of signal appearing as a shadow. (d) The large speed of sound difference between the needle and phantom materials results in a series of reverberation artifacts beyond the actual needle position.

Refraction of the US beam can cause the misplacement of positions within the image. Since the beam is travelling off the imaging axis, the returning beam may contain signals from reflections outside of the primary beam. Additionally, lateral echos, resulting from the perpendicular expansion of the piezoelectric elements are positioned as if they occur along the main beam, potentially resulting in interference when the probe is next to a highly reflecting surface[38]. Since the speed of sound is different throughout different materials, distances to boundaries may be displaced due to the assumed constant speed by the US system[38]. This effect can also reduce the accuracy of spatial measurements on the image.

2.2.3 3-Dimensional Ultrasound

The principles of 2DUS have been adapted to develop techniques to acquire full 3-dimensional volumetric datasets. The introduction of 3DUS has been an important advancement in medical imaging due to the ability to record real-time volumetric images of anatomy which can be used to diagnose, calculate volumes, observe organ function, and guide therapeutic procedures [42, 43].

A series of 2D images are acquired by sweeping the US transducer over an area and combined, with each image contributing a "slice" to the 3D volume, similar to CT imaging. Reconstruction of the 3DUS requires the location of each individual 2D image to be recorded. Spatial registration is performed using a variety of different methods. Common in 3DUS imaging are mechanical systems in which the probe is physically mounted to the tracking system. Based on the mounting of the probe to the system and mechanical encoders within, the exact position of the probe, and thus the imaging plane at any time is able to be determined. The transducer is moved over the imaging volume and the tracking system records the position and orientation of the probe for each image position and can be automated to acquire the images at pre-define intervals and locations [43, 44]. Depending on the system, images can be acquired by linear translation of the probe (stepping), rocking, rotating, or any combination as long as the imaging plane can be tracked [38]. Such systems however may be bulky and reduce the range of motion. Freehand systems, which use IR cameras or magnetic or acoustic sensors set up in calibrated locations to track the position of the transducer, can have a wider range of motion and operator control but may be limited due to line of sight or signal interference [43, 44]. In an IR system, detectors are placed on the probe and the IR camera continually monitors

the location and orientation, linking each acquired image to an imaging plane in space. Transducers with a 3D array of elements are also recently available, eliminating the need to translate the probe and allows for the acquisition of 3DUS videos.

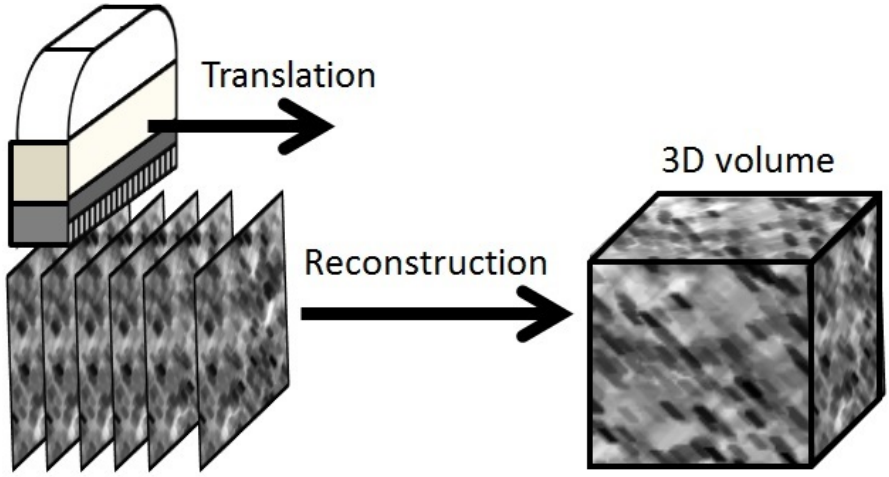

Figure 2.9: A transducer acquires US images as it is linearly translated across the imaged volume with it's position at each acquisition recorded. Based on the spatial information, the individual images are combined to create a 3D volume, with missing information filled in via interpolation.

With the location and orientation of each 2D image in the series recorded, and thus each pixel's position within 3D space, the scan can be reconstructed into a 3D volume. The most common method of reconstruction is based on using the set of 2D images to build a voxel-based image by filling in a Cartesian grid of volume elements [43, 44]. Each pixel from the acquired images is embedded into the volume by placing them in their correct 3D coordinate, based on the 2D image coordinates, and the geometry of the 2D image relative to the 3D volume determined by the tracking. Any missing voxel information is calculated by interpolation of the nearest recorded pixel values [43]. This method for volume reconstruction preserves the information acquired in the original 2D scans, but if the scan acquisition creates gaps between the images then the interpolated voxel values will not depict the true anatomy and may therefore miss small objects or boundaries, or cause blurring as mentioned in Section 2.2.2 [42–44]. Such artifacts may be reduced by acquiring more images to fill out the volume, for example by taking more slices in a lateral scan. However, increasing the number of acquired images, or slowing down the scan speed, will increase the time it takes to acquire the full 3D dataset. Additional artifacts are introduced during

the image acquisition due to unplanned patient or transducer motion. Specifically for long scan times, motion (such as breathing) may cause the scan to miss details, image objects multiple times over an area, or blur the boundaries.

2.3 Brachytherapy

Brachytherapy involves treating cancerous tissues with a radioactive source implanted inside, or very near to the diseased tissue. Treatment can be achieved by either implanting catheters through which a high activity source travels to pre-planned positions for set times, or through the permanent implantation of radioactive seeds. In either method, extensive treatment planning, dose calculations, and careful delivery are performed to ensure the treatment is safe and accurate.

2.3.1 Dose Calculations

Clinical dosimetry requires the total dose from a brachytherapy source, and the combined dose from multiple sources to be determined. During the planning process, using traditional forward planning methods, the planned source locations are selected on the volumetric image and the resulting dose to the target volumes are calculated. Adjustments to the plan may subsequently be made in order to optimize the dose distribution accordingly.

As every brachytherapy source has a unique spectrum of emitted photons and electrons, as well as geometric characteristics, dose calculations are specific to the type of radionuclide selected for treatment. One of the primary factors to determine the amount of dose that will be deposited from a particular radionuclide is the source strength. Based on the energy fluence of of the emitted spectrum, the air kerma strength, S_k, can be determined [45]. S_k is typically measured in units U, where 1 U $= 1$ cGy cm^{2}h^{-1}, with standard values for brachytherapy sources specified by standard dosimetry laboratories [21]. As mention in Section 2.1.3, low energy thresholds are used to remove photons which do not significantly contribute to the absorbed dose distribution; 5 keV in the case of photon emitters such as ^{103}Pd [21]. In order to determine the dose resulting to a relevant medium, water in standard calculations, S_k is scaled by the dose rate constant Λ (cGy h^{-1} U^{-1}), which describes the ratio of the dose rate to water at a reference position (r_o, θ_o) to the air kerma strength, either measured or calculated via simulations [21].

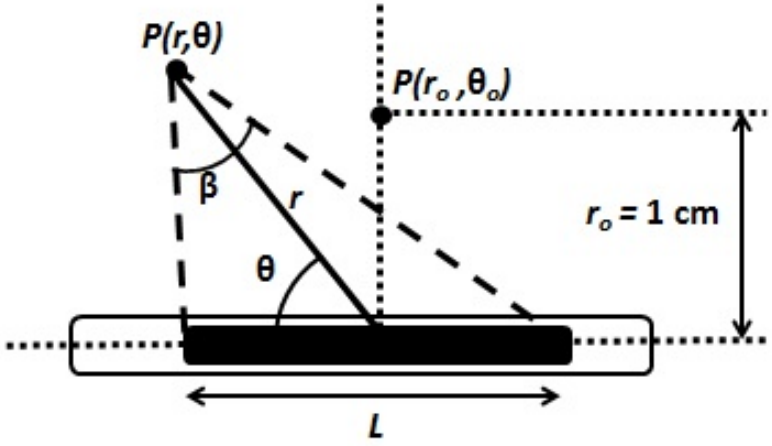

Figure 2.10: Geometry and coordinates for a 2D brachytherapy dose calculation at point P(r, θ) from a source with length L. A reference point P(r_o, θ_o) is defined at r_o = 1 cm and $\theta_o = 90^o$.

The international standard for brachytherapy dose calculations is the based on the AAPM Brachytherapy Subcommittee Task Group report 43 (TG-43) formalism, which defines the dose rate ($\dot{D}$) in water from brachytherapy sources, generally in cGy/h, at any point in polar coordinates (r, θ) by [21, 45, 46]

$$\dot{D}(r,\theta) = S_k \times \Lambda \times \frac{G_L(r,\theta)}{G_L(r_0,\theta_0)} \times g_L \times F(r,\theta). \tag{2.11}$$

As shown in Figure 2.10, the reference point, used in determining Λ, is at a distance of $r_0 = 1$ cm along the transverse axis of the source ($\theta_o = 90^o$). The physical distribution of emitted radiation is approximated using a line source geometry function $G_L(r, \theta)$ where [21]

$$G_L(r,\theta) = \frac{\beta}{Lrsin\theta} \tag{2.12}$$

and $G_L(r_0, \theta_0)$ is calculated at the reference position. The dose distribution as a function of r, mainly resulting from attenuation, is given by the line source radial dose function $g_L(r)$. As mentioned in Section 2.1.3, brachytherapy seeds are not true isotropic sources based on their physical design and therefore dose is not deposited uniformly around the seed. Factors such as self-absorption, and the emission distribution are accounted for using the 2D anisotropy function $F(r, \theta)$, dependent on the source material and seed design [45]. For poly-energetic sources (^{103}Pd), anisotropy is significant close to the source due to the prevalence of low energy photons, and at

greater distances anisotropy is essentially negligible due to the higher energy photon fluence [21].

The exact orientation of the sources is not always known in clinical practice, particularly for post-implant dose calculations. In such cases the TG-43 formalism is simplified by replacing $F(r,\theta)$ with a 1D anisotropy function ($\phi_{an}(r)$), and g_L with a radial dose function using a point source approximation ($g_P(r)$) [21]

$$\dot{D}(r) = S_k \times \Lambda \times \left(\frac{r_0}{r}\right)^2 \times g_P(r) \times \phi_{an}(r). \tag{2.13}$$

The simplified geometry, using a point source approximation, allows for the geometry function to be replaced with an inverse square law approximation, $(\frac{r_0}{r})^2$, which describes the rate of dose fall off from an isotropic source.

The source strength is dependent on the activity of the seed, and therefore changes with time in a similar fashion as the activity (Equation 2.3)

$$S_k(t) = S_{ko}e^{-\lambda t} \tag{2.14}$$

where S_{ko} is the initial source strength. Substituting 2.14 into Equation 2.11 and integrating over the treatment time (T) gives the total dose (D) delivered to a point

$$D(r,\theta) = \frac{S_{ko}}{\lambda} \times (1 - e^{-\lambda T}) \times \frac{G_L(r,\theta)}{G_L(r_0,\theta_0)} \times g_L \times F(r,\theta). \tag{2.15}$$

For permanent seed implant brachytherapy the seeds remain in place for times much longer than the active life of the isotope, thus the treatment time can be approximated as infinity and Equation 2.15 reduces to

$$D(r,\theta) = \frac{S_{ko}}{\lambda} \times \frac{G_L(r,\theta)}{G_L(r_0,\theta_0)} \times g_L \times F(r,\theta) \tag{2.16}$$

The dose to any point can be calculated using Equation 2.16 for each implanted brachytherapy source, as shown in Figure 2.11 for a single ^{103}Pd seed. For multiple sources, the superposition of the dose contributions from each source represents the total dose delivered. The contoured volumes may then be used to generate DVHs, or the percentage of the volumes to receive a specific dose. For example the percentage volume of a target that receives at least 100% of the prescription dose can be expressed as the V_{100}, and the minimum dose received by 100% of the volume is expressed as

D_{100}.

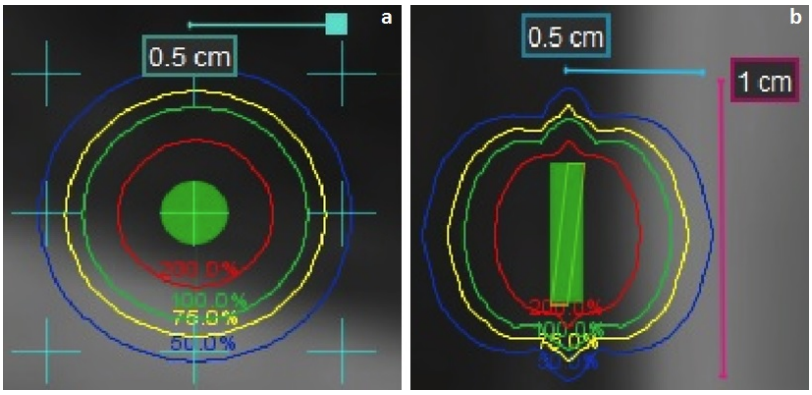

Figure 2.11: Dose distribution of a single ^{103}Pd seed resulting from a TG-43 calculation shown (a) perpendicular to the seed and (b) along the length of the seed. Isodose lines represent 200% (red), 100% (green), 75% (yellow), and 50% (blue) of the total dose deposited around the seed.

2.3.2 Seed Implant Brachytherapy

Planning and delivery methods for seed implant brachytherapy are similar across different treatment sites, but the standardization of the steps involved in LDR prostate brachytherapy related to advanced image guidance have made it one of the most widely adopted brachytherapy techniques [21]. Seed implant brachytherapy involves the permanent implantation of radioactive sources into defined treatment volumes to deliver a prescribed dose. In a general description, the process of LDR brachytherapy involves the acquisition of 3D volumetric images (through CT or 3DUS), the identification and contouring of the target volumes and margins, the pre-planning of source locations, dose calculation (via the methods described in Section 2.3.1), followed by implant and post-implant verification [21, 47]. Seed implant brachytherapy is most commonly used in the treatment of localized prostate cancer and has been shown to be a highly effective treatment option [21, 48]. The success of the treatment relies on achieving optimal dosimetry, which requires accurate imaging, planning, and delivery.

Planning for LDR prostate brachytherapy is generally performed using a transrectal ultrasound (TRUS) system to acquire images throughout the prostate region and generate a 3D dataset that is used for treatment planning [21, 47]. The probe is mounted on a stabilizing device, known as a stepper, which tracks the position during image acquisition which can then be reconstructed into a 3D volume (Section 2.2.3).

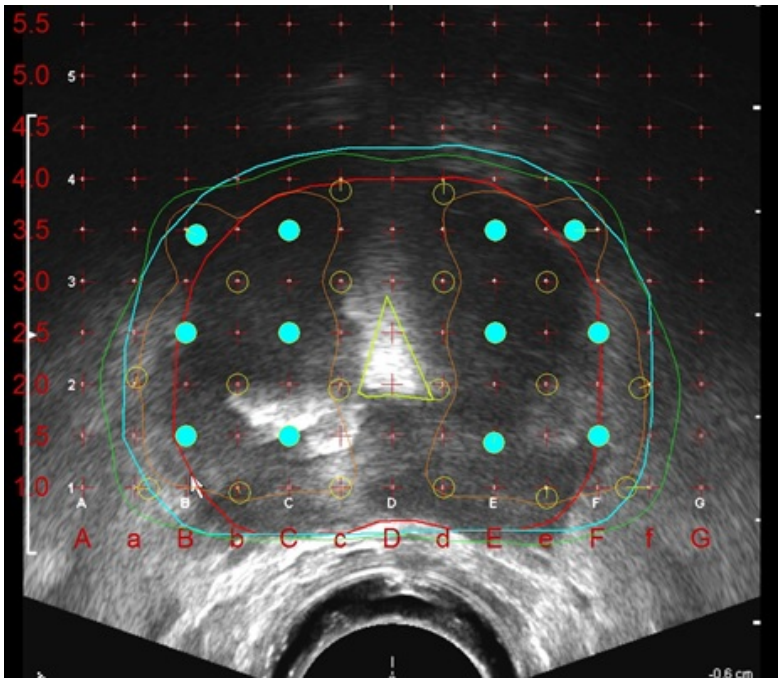

Figure 2.12: Planning a prostate LDR implant using TRUS images. The seed positions (blue points) are planned to provide coverage (100% dose in green) to the prostate (red) and PTV (blue). The 150% dose region (orange) is confined to outside of the urethra (yellow).

The TRUS stepper can be used to step the probe by known distances to acquire a series of transverse images, or rotate the probe to acquire a "fan" of longitudinal images which are used to reconstruct the 3D volume [24, 49]. TRUS based planning offers advantages as planning and delivery can be performed using the same imaging modality in the same patient positioning, and provides very accurate imaging to differentiate between the prostate, rectum, and bladder [21]. Image acquisition may occur several weeks before the actual implant [48].

As shown in Figure 2.12, the prostate is contoured on the treatment planning system and a PTV is generated by expansion of the prostate contour by several mm (5 mm laterally, 3 mm anteriorly) [48]. The TRUS is inserted along the cranial-caudal axis of the patient. A template, composed of a grid of small holes to guide the needles, can be mounted on the US system. Due to the spatial registration of the imaging and stabilizing system, the template positions can be displayed on the 3D dataset by extrapolating the template holes over the treatment depth in order to plan the treatment in the orientation that the implant will be delivered. Template positions are used to define the entry point, and position at depth, for various needles. Each needle

is planned to be loaded with several seeds and distributed in order to provide optimal coverage to the PTV while limiting the dose to the urethra. ^{125}I (28.4 keV, $T_{1/2}$ = 59.4 days) is primarily used due to the ability to achieve better dose distributions and reduced severity of normal tissue complications such as proctitis compared to implants using ^{103}Pd [47]. Standard prescription dose is 145 Gy for ^{125}I implants, or 110 Gy if used as a boost following EBRT, requiring approximately 100 seeds to be implanted [47, 48].

During the implantation procedure the patient is positioned in the OR and the TRUS is used to refine the setup in order to match the position to the planning TRUS images [21, 47]. The template is mounted on the stepper while a virtual representation of the template positions are displayed in the 3DUS image. Each needle is commonly pre-loaded with the seeds based on the treatment plan. Needles feature a sharp beveled edge (Figure 1.6) and central stylet which is used to hold the seeds in place as the needle is removed. The needles are inserted into the planned template positions, through the perineum. Although the needles are inserted in the planned entry point, their position at depth may deviate from the intended position, thus resulting in the misplacement of seeds if not corrected. The implementation of TRUS into the implant procedure allows for the visualization of the needles at depth and real-time guidance. Since the position of the US probe is registered to the insertion template, the virtual representation of the template hole positions can be visualized at depth on the US image, as shown in Figure 1.3. A live display of a needle as it is being inserted assists in ensuring that the needle is placed at the correct depth and position. Based on the implanted position and the expected location, adjustments can be made to the needle insertion to achieve an accurate position before the seeds are deposited.

Post-implant the treatment is verified via a dosimetric evaluation. Imaging is performed to evaluate the positioning of the seeds and the dose distribution that was achieved from the implant. Post-implant verification may be performed immediately after implant (day-0), but more typically occurs 1-month afterwards (day-30) when swelling has decreased [21, 48]. CT is considered standard for post-implant verification as it provides good localization of the implanted seeds, although fusion with magnetic-resonance images may be used in addition to CT to assist in tissue delineation [21, 48, 50].

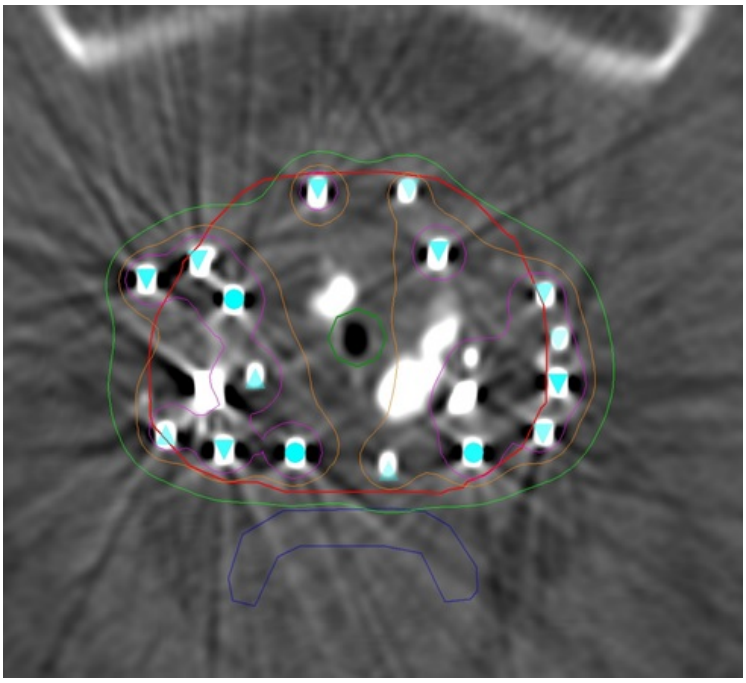

Figure 2.13: Prostate LDR post-implant CT. The seeds (bright spots) are identified to calculate the dose to the prostate (red), urethra (green) and rectum (blue). Here, the prostate was defined on MRI and the contour transferred to the CT images, due to the difficulty of observing the prostate on the CT.

2.3.3 Brachytherapy for Breast Cancer

Brachytherapy plays an important role in the modern treatments of breast cancer, and is used in approximately 30% of APBI treatments [21]. The most common breast brachytherapy procedures are intracavity balloon and interstitial multicatheter brachytherapy [21]. The intracavity balloon procedure involves the insertion of a balloon at the end of a catheter, under US or CT guidance, which is filled with saline to expand the balloon (4 - 5 cm) and fill the excision cavity. Multilumen catheters within the balloon allow for an ^{192}Ir source to be loaded into the balloon with pre-defined positions and times to provide an optimal dose distribution around the expanded volume. A similar procedure can be performed with a strut-based system which provides a non-symmetric lining of the seroma, allowing for more flexible dose distributions [21].

Interstitial multicatheter brachytherapy allows for complex and flexible dosimetry of the target volume. This procedure involves the implantation of multiple catheters in and around the post-lumpectomy seroma volume [51]. Appropriate placement of

the catheters and accurate definition of the target volumes are critical to the success of the treatment, so an extensive planning procedure is required [21, 51, 52]. Patients receive CT imaging to evaluate the eligibility and technical feasibility, and may also be used to define the target volume (1 - 2 cm expansion of the seroma contour). The breast is often compressed with a bridge template to provide a rigid guide for the implant. The template and breast are held in place by several needles that are inserted through the template, pass through the breast, and emerge at the same template position on the distal side of the breast. A CT scan of the setup is performed in order to define the treatment volumes and plan the appropriate positions for the implanted catheters to adequately cover the target.

Catheters are implanted in the planned positions, sometimes under US image guidance, after which another CT scan is performed. The final, uncompressed, CT scan reveals the actual locations of the implanted catheters within the breast and is used to determine the optimal dwell positions and times for the ^{192}Ir source within the catheters. When an acceptable plan has been generated the catheters are connected to an HDR afterloader that feeds the ^{192}Ir source into each catheter, slowly pushing it through the catheters to the planned depths for the calculated times. The treatment typically occurs over several days with two fractions per day, for example 34 Gy prescription dose over 5 days (3.4 Gy per fraction), after which the catheters are removed [21, 51, 52].

Improvements to image guidance in multicatheter interstitial HDR breast brachytherapy allow for a simpler and more accurate treatment. 3DUS guided brachytherapy techniques have recently been applied to this procedure [52]. Multicatheter breast HDR planning requires the patient to move from the implant OR to CT scanning after the catheters have been inserted. A novel 3DUS system to be used specifically in HDR breast brachytherapy was developed in order to increase confidence in catheter insertion and allows for intra-operative US-based planning to be performed [52]. The mechanical scanning system was developed to fit on the HDR compression template and sweep the transducer across the treatment area to gather a series of approximately 200 images in a 5 cm scan length. The US images are spatially encoded based on the transducer's mounting position relative to the template, the translational scan position, and the probe angle. The mounting position and geometry are then used to reconstruct the 3D volume.

Software modules for image reconstruction, seroma segmentation, and catheter reconstruction for the system were implemented to allow for intra-operative treatment

planning [52, 53]. Fast, semi-automatic segmentation is based off of techniques developed for prostate contouring for intra-operative planning in prostate brachytherapy [54, 55]. Needle segmentation techniques are also important in accurately defining the catheter positions to perform does calculations on US in prostate brachytherapy [24, 56, 57]. Catheter reconstruction was similarly used in the breast HDR system to accurately plan the source positions on the US images. A module was also developed to automatically move the transducer to the current needle insertion plane in order to perform real-time needle insertion guidance [53]. Overall, the development of a 3DUS translation scanner for breast has demonstrated accurate image reconstruction, needle localization, and volume segmentation proving to be a useful tool, similar to that standard imaging techniques used in prostate brachytherapy [52, 53, 58]. As 3DUS has been successfully developed to guide various LDR and HDR brachytherapy procedures, including breast HDR, the potential exists for such technology and techniques to be further adapted to assist in the PBSI brachytherapy implant procedures.

2.4 Permanent Breast Seed Implant Brachytherapy

As discussed in Section 1.2.2, PBSI is novel brachytherapy procedure, relative to other forms of breast brachytherapy [8]. Presently, the technique is still being adapted, but many of the original guidelines and general techniques are still in use. This section describes the current PBSI procedure that has been used for the presented research, including patient guidelines, planning methods, delivery, and verification.

2.4.1 Patient Criteria

As a relatively new procedure, PBSI is currently only available to patients who meet a specific eligibility criteria. APBI treatments in general are often limited based on patient age (due primarily to expected life span), tumour size, resection margins, and disease staging [7, 10, 21, 28, 30]. PBSI is currently limited to low-risk patients including those over 50 years with ductal carcinoma *in situ* or t1, estrogen receptor positive invasive ductal carcinoma, and no evidence of metastatic disease [59, 60]. After tumour resection, pathology determines the amount of diseased-free tissue around the lumpectomy site, with eligible patients having greater than 3 mm margins [10].

Additional technical eligibility criteria are required for PBSI patients in order to provide safe and effective treatments. For planning and delivery to be possible, the seroma must be clearly visualized on both CT and US and the seroma itself should be less than 3 cm in equivalent sphere diameter [59, 60]. The resulting PTV size is ideally less than 120 cm^3 [10]. The seroma must be in a position such that it can be accessed by the insertion of needles from the lateral side without requiring insertion through the chest wall or directly toward the skin surface or lung on the distal side. Additionally, the size of the breast has to be feasible for implant, as large implant depth and breast mobility may inhibit reproducibility in the procedure.

2.4.2 Planning and Delivery

Treatment Planning

Within approximately 10 weeks of lumpectomy, allowing the seroma time to stabilize after surgery [61], CT and evaluative US scans are performed for potential PBSI patients. Patients are positioned on a breast board (Figure 1.2) in the EBRT treatment position with the ipsilateral arm raised in an extended position. US is used to localize the seroma and measure the size and distance to skin in order to evaluate technical eligibility [8]. A CT scan is subsequently performed with the patient in a reproducible position, and tattoos are placed on the patient (Section 2.2.1). If deemed suitable for PBSI treatment, the patient's CT scan is imported into a TPS, MIM Symphony (MIM Software, Cleveland, OH), where the treatment planning procedure is performed.

The planning process, shown in Figure 2.14, begins by contouring the relevant anatomy within the breast, including the chest wall and skin surface. A skin margin is defined as a 5 mm inner ring from the skin surface. The seroma is contoured using standard clinical guidelines for APBI, defining the CTV as the evident dense region in the image, including surgical clips that are deposited during the lumpectomy around the perimeter of the excision site if present [62]. The PTV is generated by expanding the CTV contour by 1.25 cm, cropped at the chest wall and at 5 mm from the skin surface [60, 63]. The fiducial needle, which centres the treatment template, is planned to be inserted in the lateral side through the center of the CTV (isocenter) to the distal side of the PTV, approximately tangential to the chest wall to minimize the risk of puncturing the lung (Figure 2.14a) [8]. Based on its position and direction, the fiducial needle entry point on the skin surface is determined. Images are re-sliced

in directions orthogonal to the fiducial needle insertion angle to provide a needle's-eye-view of the template throughout the treatment volume, as shown in Figure 2.14b.

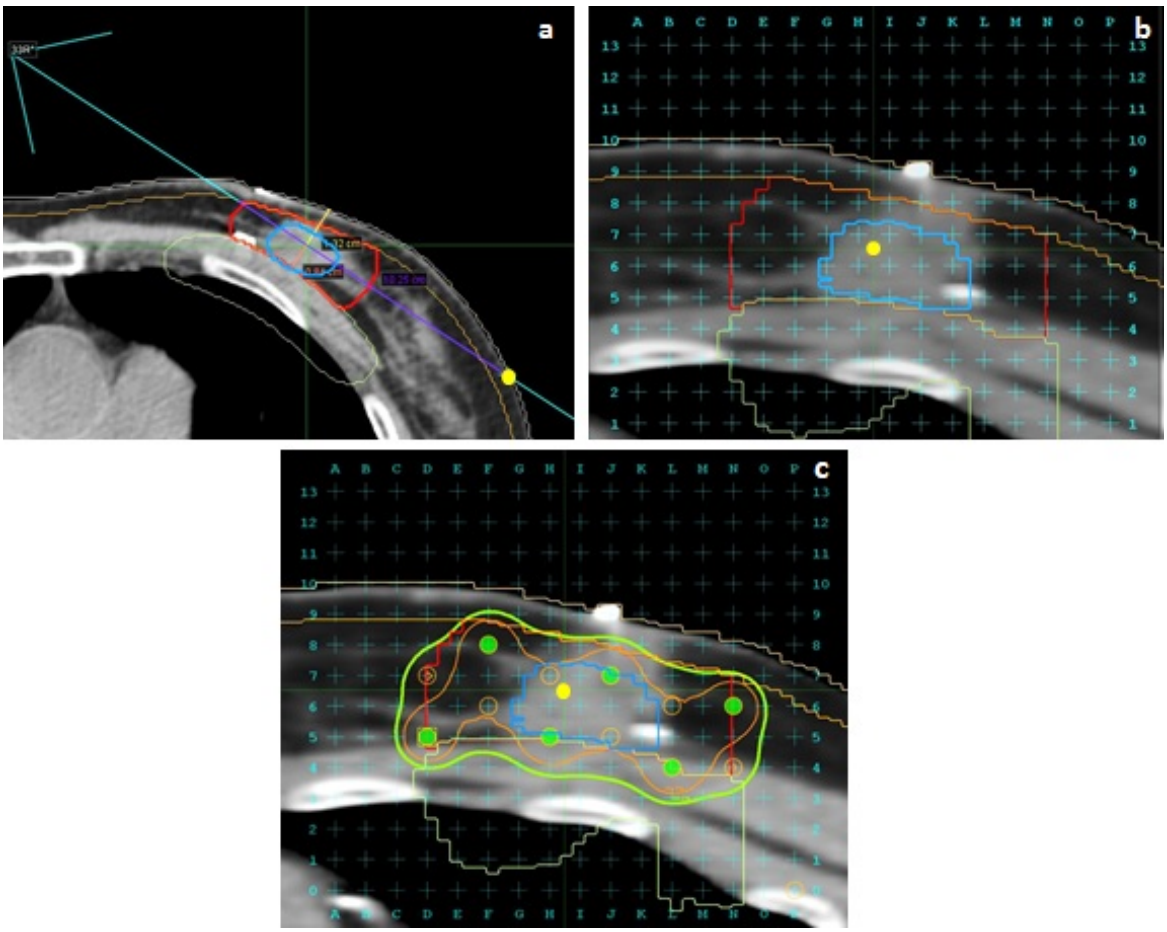

Figure 2.14: (a) The fiducial needle angle approximately tangential to the chest wall (green), through the seroma (blue), and the resulting needle entry point marked on the skin surface (yellow). (b) Image re-sliced perpendicular to the insertion direction (needles-eye-view), with the template centred on the fiducial needle (yellow). (c) Needle and seed positions (green points) planned to provide coverage to the PTV (red). The green areas represents the volume receiving 100% of the prescribed dose, while the orange represents the 150% high dose region.

The needle positions are planned around the perimeter of the PTV and evenly throughout in grid pattern [10]. Seeds within the peripheral needles are planned to be spaced 1 cm apart, alternating between a seed and a spacer (each 4.5 mm long), and seeds within the central needles are separated by 2 spacers (1.5 cm between seeds), in order to improve dose homogeneity throughout the PTV [10]. Manual adjustments to the seed positions and spacing can subsequently be made to optimize the dose

distribution throughout the volume. The activity of the seeds is typically 2.5 U, but may be slightly adjusted (±0.3 U) to improve the coverage [10, 60]. Positions are planned such that no 2 needles are inserted with less than 1 grid spacing (5 mm) between them, and at least 1 cm of space exists between adjacent seeds to prevent overlap and potential high dose "hot spots". The cumulative dose from the seeds is calculated via the methods described in Section 2.3.1, using a line source geometry. The prescription dose of 90 Gy is planned to be delivered throughout the PTV, with target goals of $V_{90} > 98\%$, $V_{100} > 95\%$, $V_{150} < 75\%$, and $V_{200} < 25\%$, while limiting the skin dose to less than 90% of the prescription over a 1 cm^2 area to minimize skin toxicity [9, 60, 63].

Delivery

The delivery process begins with a mark-up procedure, intended to reduce set up time in the OR [32]. Patient planning positioning is reproduced using the breast board, room lasers, and tattoo positions. The fiducial entry point and treatment isocenter are then marked on the skin surface (Figure 2.15a). US is used to assess the seroma for any changes from planning, and the projection of the PTV, orthogonal to the needle direction, is marked on the skin surface to guide US imaging during the implant [10, 32].

After the patient has been moved to the OR and is given general anaesthesia, the setup is again reproduced (Figure 2.15b). Lateral tattoo and fiducial needle entry points are verified through manual measurements [32]. The template is positioned and set to the planned angle, and the fiducial needle is inserted. Positioning of the fiducial needle is verified with US and adjustments may be made to position the needle as planned relative to the seroma (Figure 2.15c). After the template has been set, the preloaded needles are inserted into their planned positions, row-by-row starting from the bottom to prevent visualization interference from the seeds in the US images [10]. Free-hand US is used to qualitatively evaluate the positions of the needles relative to the seroma and fiducial needle, the protrusion of the needles is measured to ensure the correct depth (Figure 2.15d) and the seeds are deposited when an appropriate position has been achieved.

Following the completion of the implant, after anaesthetic recovery, the patient is again repositioned in CT to evaluate post-implant dosimetry. A follow-up scan is performed at a later time (day-30 or day-60) to provide quality assurance of the

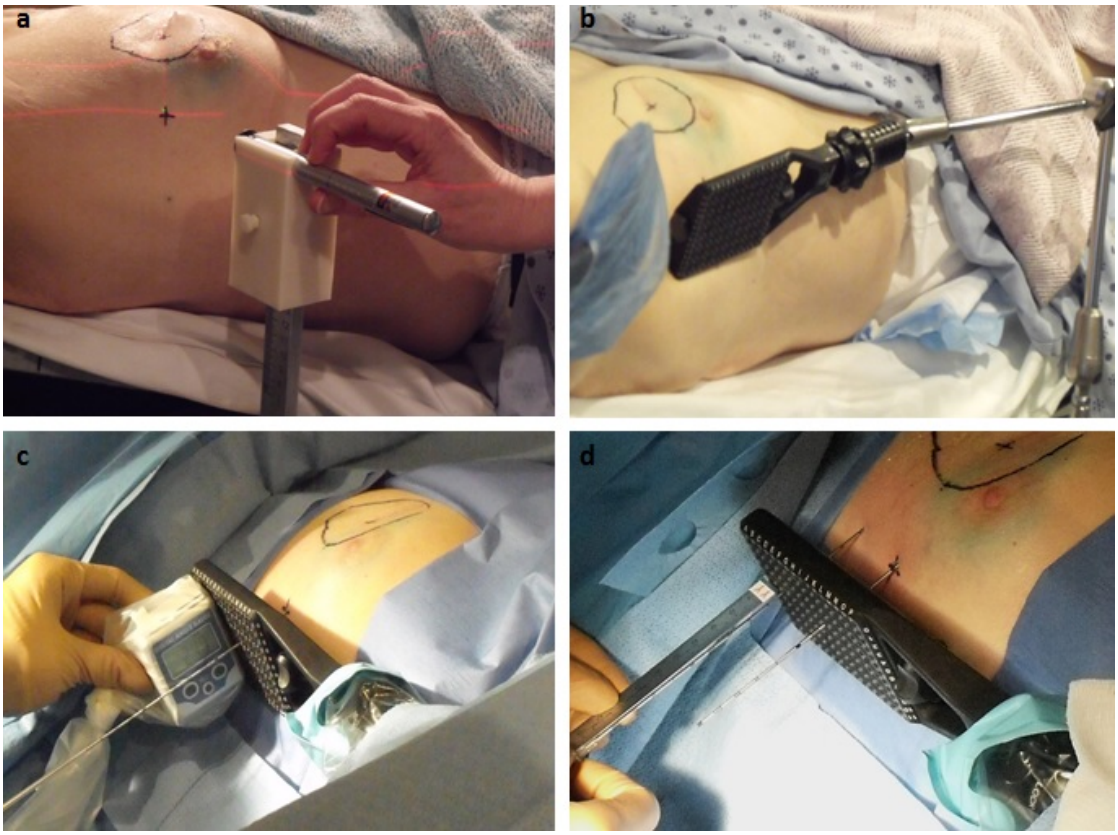

Figure 2.15: PBSI delivery procedure. (a) The fiducial needle entry point is marked using the CT rooms lasers and verified using a portable laser. (b) The set up is recreated in the OR and the template is set into it's planned position. (c) The fiducial needle is inserted and final adjustments to the template positioning are made. (d) Loaded needles are inserted into their planned template positions with depths verified by the protrusion distance.

overall treatment [10, 60, 63]. The implanted seed positions are identified on the CT images and the resulting dose is calculated using a point-source geometry (Equation 2.13). The seroma is contoured on the post-implant CT, and an evaluative target volume (ETV), defined as a 0.5 cm expansion of the CTV, is created to assess the quality of the implant [60]. Additionally, the dose to OARs (skin, breast, lung, ribs, heart) is verified in order to track toxicities [9, 60, 63].

2.4.3 Previous Work in PBSI

As mentioned previously, the use of permanent seed implants in breast brachytherapy is a relatively new procedure, with the first treatments reported by Pignol *et al.* in

2006 [8]. Research and development of the procedure was helmed by Pignol and Keller of the Sunnybrook Health Sciences Center (Toronto, ON). The feasibility of the treatment was first reported based on the initial results of 16 implants over a 7 month period, yielding a mean PTV V_{100} of 79.8% (64.4% - 96.4%) with improvements occurring with operator experience, suggesting a learning curve in the procedure [8]. A follow-up report examined the dose received by family members living with the PBSI patients, due to the potential risk associated with sources implanted close to the skin surface, and concluded the procedure to safe for the public [64].

A 1-year follow-up evaluation was presented by Pignol *et al.* in 2009, summarizing the tolerance and acceptance results of skin related side-effects for 67 patients [33]. This study showed that the procedure was well tolerated, comparing favorably with external beam APBI in terms of skin toxicity, and that the rate of skin reactions decreased (65% to 28%) when the skin received less than 85% of the prescription dose. A report on dosimetry quality assurance evaluated a total of 95 patients across three clinical trials. Planning dosimetry was recommended to aim for a V_{90} of approximately 100% and a V_{200} of between 20 and 30% in order to achieve a successful treatment [9]. A recent multi-institutional follow-up summarized the early dosimetry for the current cohort of patients treated with PBSI, as discussed in Section 1.2.2, finding overall successful recurrence rates and toxicity, supporting the efficacy of the treatment [10]. Subsequent follow-ups focused on the toxicities of PBSI determined that patients with tumour sites located medial and closer to the skin surface were more susceptible to acute side-effects (skin irritation) than primary tumour sites located elsewhere in the breast, and that tumour size and depth are important for consideration for late effects (telangiectasia) [65]. An initial group of 17 patients were treated with PBSI at the Tom Baker Cancer Centre. In this group, evaluation of the dosimetry relating to patient arm positioning found a significant, but relatively small, increase to the V_{200} within the ETV when the arm was not in a raised position, when the majority of the dose will be deposited [66].

Beyond initial implementation, some attempts have been made to standardize post-implant quality assurance and dose reporting by the PBSI research group at the BCCA - CSI. Presently, 52 patients have been treated with PBSI at BCCA - CSI. Early implementation of the procedure found that the seroma was difficult to identify and manually contour on the post-implant CT due to artifacts from the implanted seeds, thus affecting the accuracy of post-implant dosimetry [59]. Deformable image registration and adaptive contouring were used to define the post-implant seroma

from the planning CTV contour with a high-level of accuracy and is recommended for post-implant quality assurance [59]. Standardization of dose reporting for skin toxicity was also developed as the previous recommended guideline of reporting the maximum skin dose to a point [7] was not deemed robust and clinically relevant enough for breast brachytherapy, particularly due to the area effect of radiation on skin [17, 63]. By assessing the correlations between various metrics, the dose to small volumes were found to be robust measures of skin dose, and the dose to a 2 mm internal skin layer ($D_{0.2cc}$), approximately the dose to a 1×1 cm^2 area, was recommended for dose reporting in PBSI [63].

Additional developments into the planning and delivery process in PBSI have not yet been widely explored. An improved dose calculation method has been considered to correct for the tissue heterogeneity within the breast, rather than the simplified homogeneous water-based TG-43 calculations, and was able to detect plans with inadequate coverage and better predict skin toxicity, although this has not yet been implemented clinically [67]. Beyond improved standardization of the set up procedure using the pre-implant procedure described in Section 2.4.2 [32], no additional significant developments into improving the planning or delivery procedures in PBSI have been made.

2.5 Chapter Summary

The fundamental processes behind RT and imaging have been described. From the overview of brachytherapy, specifically the LDR prostate brachytherapy technique, it can been seen how these processes can be applied to the successful treatment of cancer. Imaging with US is an important component of brachytherapy and, with advancements in 3D volumetric imaging, can provide a means to both accurately plan and deliver treatments. The well established prostate LDR technique serves as a benchmark for the standardization and accuracy of further developments in seed implant brachytherapy. While PBSI has been successfully adopted by expert practitioners, challenges in the technique, specifically related to imaging, have not been addressed. Unlike in prostate brachytherapy, PBSI is planned and delivered using different imaging modalities and there is no spatially registered needle guidance system to provide real-time feedback on quality during the implant. The goal of this work is to quantify uncertainties in the PBSI to identify the components which reduce the accuracy and adaptability and to develop techniques to ameliorate such issues

and improve standardization of the procedure. The following chapter describes the methods used to quantify the uncertainties in the PBSI procedure and presents the proposed methods to implement improved US imaging in both treatment planning and delivery.

Chapter 3

Materials & Methods

This chapter describes the principle methods common to several studies in the presented work. First, the methods to evaluate seed placement accuracy in PBSI are described. A detailed description of the tracked 3DUS system used to acquire patient images for retrospective analysis is provided, along with the general methods of image assessment used. Additionally, a novel 3DUS scanning system was developed specifically for PBSI implant guidance. The design of this system and the initial calibration and commissioning that were performed are outlined.

3.1 Evaluation of Seed Placement Accuracy

The accuracy of seed placement in PBSI can be used to evaluate uncertainties in the procedure and serves as a benchmark for the improvements in accuracy through additional developments to the planning and delivery procedures. Methods were established to evaluate seed placement based on the differences between planned and implant positions and are used throughout this work to quantify the current PBSI procedure and identify the components which may be improved through refinement of techniques.

3.1.1 Image Registration

The accuracy of seed placement could be determined by rigidly registering the planning and post-implant CTs and evaluating differences between the planned and implanted seed positions. As described in Section 2.4.2, following the implant (day-0) as part of the post-implant verification procedure, a CT scan is performed to evalu-

ate the dosimetry achieved from the treatment. Due to the difficulties in visualizing the seroma on the post-implant CT as a result of seed-generated image artifacts, deformable image registration and adaptive contouring (MIM Maestro, MIM Software, Cleveland, OH) are used in the clinical procedure to define the post-implant seroma on the day-0 CT, previously validated for use in PBSI post-implant dosimetry [59].

To evaluate seed placement accuracy, a rigid registration of the planning and day-0 CTs was performed, based around spatially aligning the implant region on both CTs. The registration process was performed using the image registration tools in MIM Symphony (MIM Software, Cleveland, OH). A region of interest (ROI) on both the planning and post-implant CTs was defined as the seroma plus a 1 cm margin to include only the most relevant region of the breast to the implant. An intensity based rigid registration was subsequently performed to spatially transform the day-0 CT coordinates in order to align the ROIs. The registration (R_T) can be expressed as a 3D affine transformation of the day-0 coordinates

$$R_T = \begin{bmatrix} \cos\phi\cos\omega & -\cos\phi\sin\omega & -\sin\phi & T_x \\ \sin\theta\sin\phi\cos\omega + \cos\theta\sin\omega & -\sin\theta\sin\phi\sin\omega + \cos\theta\cos\omega & \sin\theta\cos\phi & T_y \\ \cos\theta\sin\phi\cos\omega - \sin\theta\sin\omega & -\cos\theta\sin\phi\sin\omega - \sin\theta\cos\omega & \cos\theta\cos\phi & T_z \\ 0 & 0 & 0 & 1 \end{bmatrix} \tag{3.1}$$

where θ, ϕ, and ω are rotations in the sagittal, coronal, and axial planes, respectively, and T_x, T_y, and T_z are linear translations. R_T can therefore be used to transform the position of any point in the day-0 CT in the planning CT coordinate system.

The registration process was qualitatively evaluated as shown in Figure 3.1. The agreement between the anatomy within the breast, the chest wall, ribs, and skin surface were assessed. Quantitative validation of the registration process was performed by assessing the locations of surgical clips in the registered coordinates. Surgical clips may be implanted around the lumpectomy site at the time of excision and are therefore present in both the planning and day-0 CT images. The location of clips within the ROI, in the shared coordinate system, were manually identified in the registered image sets and the distances between them were calculated to quantify the accuracy of the registration process.

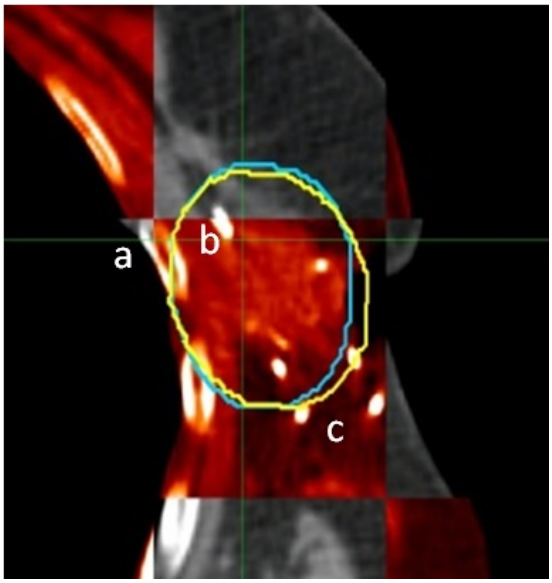

Figure 3.1: Fusion of the planning (gray) and day-0 (red) images after rigid registration based on the volume inside of the ROIs (yellow and blue). The position of a rib (a) is observed to have good agreement between the images. The location of a surgical clip visible in both images (b) within the ROI is nearly identical in the registered coordinates. The bright spots within the day-0 image (c) represent the implanted seed positions, and therefore do not appear in the planning CT.

3.1.2 Seed Matching

The individual implanted seeds are identified in the day-0 CT as part of the post-implant dosimetry process. An automatic identification process (MIM Symphony) is used to define the location of the seeds based on the intensity in the CT image. As can be seen in Figure 3.1, the seeds appear as bright spots in the image and can easily be manually identified in the absence of image artifacts or overlapping seeds and clips. Manual verification of the identification process is performed to ensure that the correct number of seeds have been identified and that clips were not mistakenly localized before post-implant dosimetry is evaluated.

The locations of the post-implant seeds were exported from MIM Symphony in the respective day-0 CT coordinates. Applying the transformation matrix generated from the registration of the day-0 CT to the planning CT (Equation 3.1), the implanted seed coordinates $(x_i,\ y_i,\ z_i)$ could be transformed to the planning CT coordinate

system by

$$\begin{bmatrix} x_t \\ y_t \\ z_t \\ 1 \end{bmatrix} = R_T \times \begin{bmatrix} x_i \\ y_i \\ z_i \\ 1 \end{bmatrix} \tag{3.2}$$

where x_t, y_t, z_t are the transformed seed positions in the medial-later (ML), anterior-posterior (AP), and superior-inferior (SI) directions, respectively. The treatment plan was similarly exported and the planned seed positions extracted, in the planning CT coordinates. Applying the transformation to each implanted seed coordinate allowed for the superposition of the planned and implanted seed positions. As seen in Figure 3.2, the planned seed positions are in a straight line, perpendicular to the SI axis in the planned insertion direction. The implanted seed positions, however, do not always appear in straight lines as a result of placement deviations, needle bending, and deformation of the anatomy after implant, but, due to the physical stranding of the seeds, they remain grouped with the other seeds from the same needle.

The registered seed coordinates were used to evaluate the position of the implanted seeds relative to the planned positions. The difference in the planned and implanted seed positions is referred to as the seed displacement. Custom seed-matching software (SeedPreview) had previously been developed to quantify the motion of seeds in prostate brachytherapy [68]. This software displays a 3D visualization of superposed seed clouds and allows for seeds to be manually paired to calculate the distances between them. The software was modified for the evaluation of seed placement in PBSI. The registered seed coordinates were imported into SeedPreview and the pairing tool was used to manually match each implanted seed to it's planned position (Figure 3.3). Due to the random variations in the placement, seeds could not necessarily be matched to the closest position without incorrectly dividing the strands. In general, the matching process was performed by first determining the number of seeds in a particular planned needle and then finding the nearest implanted strand with the same number of seeds. When each strand was confidently matched to the planned needles, pairing of the seeds was performed in order along the needle insertion direction so as to not leave any seeds unmatched. After pairing, the implanted seed displacements are calculated in both magnitude and direction (ML, AP, SI).

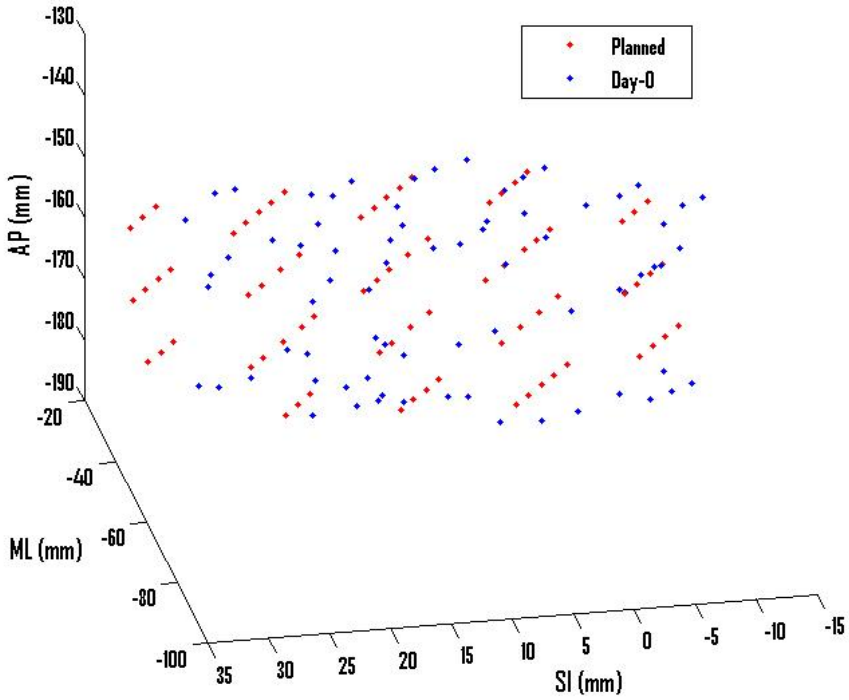

Figure 3.2: Superposed planned (red) and implanted (blue) seed clouds with positions in the planning CT medial-Lateral (ML), superior-inferior (SI), and anterior-posterior (AP) coordinates.

3.1.3 Seed Placement Analysis

Based on the results of the seed matching process, an evaluation of the seed placement accuracy could be performed within a cohort and for individual patients. The metric used to quantify the global seed placement accuracy was the mean total displacement of all implanted seeds, and mean directional (ML, AP, SI) displacements could be assessed in order to determine any global systematic errors in seed placement accuracy. Within individual implants, several metrics were calculated to quantify the uncertainties in seed placements: the mean total displacement, directional displacements, the systematic displacements, and the random displacements. The mean total displacement of all seeds within an individual implant was used to quantify the overall accuracy of seed placement. Similarly, the mean directional displacements were assessed in each of the standard coordinate directions (ML, AP, SI). Mean directional displacements are a result of shifts in the displacements' directional distributions,

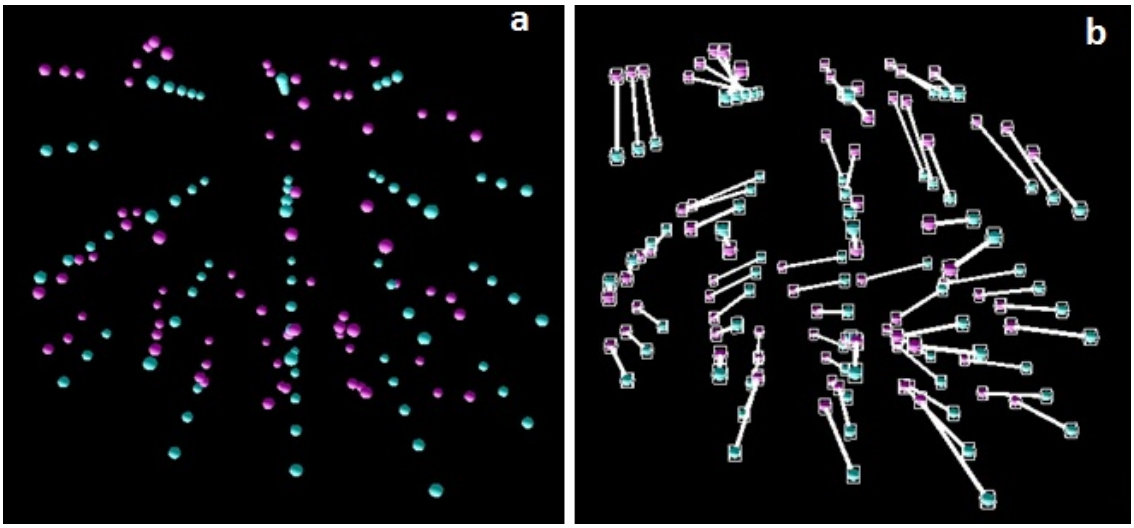

Figure 3.3: (a) 3D visualization of the planned (blue) and implanted (pink) seed clouds along the needle insertion direction. (b) The implanted seeds are paired with the planned positions (white connecting lines), calculating the distance between them.

implying systematic intra-patient uncertainties in seed placement. Therefore, the norm of the mean directional displacements was used to approximate the systematic component of uncertainties in placement within each implant

$$Systematic = \sqrt{\bar{x}^2 + \bar{y}^2 + \bar{z}^2} \tag{3.3}$$

where $\bar{x}$, $\bar{y}$, $\bar{z}$ are the mean directional displacements in the ML, AP, and SI directions. By removing the systematic component from the displacements, or shifting the directional distributions to centre at zero, the remaining displacement could be used to approximate the magnitude of the random component of the uncertainties in placement. The mean directional displacements were subtracted from each individual seed's directional displacements and the residual magnitude was averaged across all seeds in the implant

$$Random = \frac{1}{n}\sum_{i=1}^{n}\sqrt{(\Delta x_i - \bar{x})^2 + (\Delta y_i - \bar{y}^2) + (\Delta z_i - \bar{z}^2)} \tag{3.4}$$

for a cohort of n seeds where Δx_i, Δy_i, Δz_i are the directional displacements of the individual seeds.

In addition to the directional displacements in the standard CT coordinates , displacements were calculated in a needle coordinate system to quantify displacements

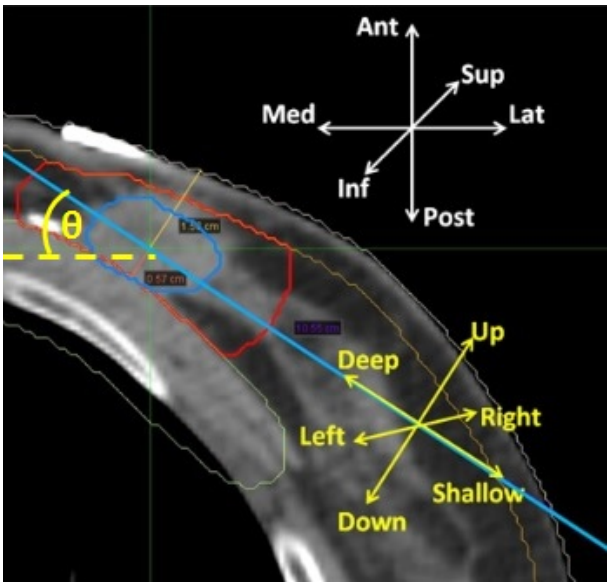

Figure 3.4: The standard CT coordinate system (white) and the rotated needle coordinate system (yellow) used to assess seed displacements.

relative to the needle insertion direction. As shown in Figure 3.4 [60], the directional displacements are rotated by the fiducial needle insertion direction (θ) and are transformed into displacements corresponding to the depth of insertion, and the up-down and right-left directions in the needle's-eye-view (template directions). The rotation is performed by

$$\begin{bmatrix} \Delta x_r \\ \Delta y_r \\ \Delta z_r \end{bmatrix} = \begin{bmatrix} \cos\theta & -\sin\theta & 0 \\ \sin\theta & \cos\theta & 0 \\ 0 & 0 & \pm 1 \end{bmatrix} \times \begin{bmatrix} \Delta x \\ \Delta y \\ \Delta z \end{bmatrix} \tag{3.5}$$

where Δx_r, Δy_r, Δz_r are the displacements in the shallow-deep, up-down, and right-left directions, respectively, θ is the planned fiducial needle angle, and the sign of x (ML) has been corrected for insertions from the left or right side. The needle is inserted perpendicular to the SI-axis and the sign of z_r is reversed for insertions from the right side, as superior displacements are equal to displacements to the left in the needle coordinates for right sided implants, and vice versa.

3.2 3D Ultrasound Image Acquisition and Analysis

Investigation of the differences between the seroma visualized in planning and treatment and the potential impact on treatment planning and delivery required 3DUS images of the seroma that could be assessed in the TPS. For two of the studies in this work, images were acquired using the Clarity US system (Resonant Medical, Montreal, QC). The differences in the seroma on US and CT, and the potential impact of implementing 3DUS into the treatment planning procedure were assessed in MIM Symphony.

3.2.1 3D Ultrasound System

The Clarity US system is a 3DUS platform which acquires and reconstructs volumetric images by visual tracking of the US probe. The system was predominately designed for use in prostate EBRT treatments, in which it could be used for prostate localization instead of x-ray image guidance [69–71]. However, investigation into its use in breast EBRT planning and delivery has also been previously performed [36, 72, 73].

The Clarily US system uses infrared (IR) imaging to track the US probe in order to construct 3DUS images (Section 2.2.3). A mounted IR camera tracks the position of calibrated IR markers that are attached to the US transducer (Figure 3.5b), allowing for recognition of the transducer's position and orientation at all points during image acquisition. The linear array 2DUS transducer (L14-5W, Ultrasonix), with a resolution of 0.25 mm in the imaging plane, can therefore be freely swept across an area with continuous detection and acquisition allowing for the reconstruction of a 3D volumetric image [36, 73].

As the Clarity system is designed for image guidance in EBRT, the system may be used in conjunction with CT scanning to provide a mutual coordinate system between the two modalities. The IR camera is mounted in the CT room in order to track acquisition while a patient is in the simulation position. The spatial information of the US system is calibrated such that images are reconstructed in the same coordinate system as the CT images. A calibration and quality assurance (QA) phantom is positioned in the CT scanner, centred on the isocentric lasers that define the CT origin. IR markers on the phantom are localized by the camera, establishing the coordinate system of the room. Based on the known positions of the markers on the

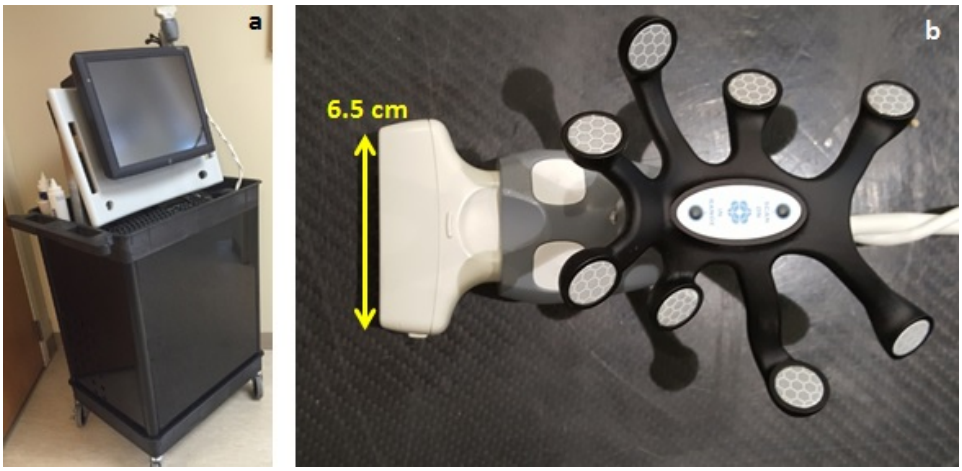

Figure 3.5: (a) The Clarity US system reconstructed into a mobile unit. (b) The US transducer used with the Clarity 3DUS system. The IR camera tracks the locations of sensors mounted on the probe to record spatial information of the acquisition.

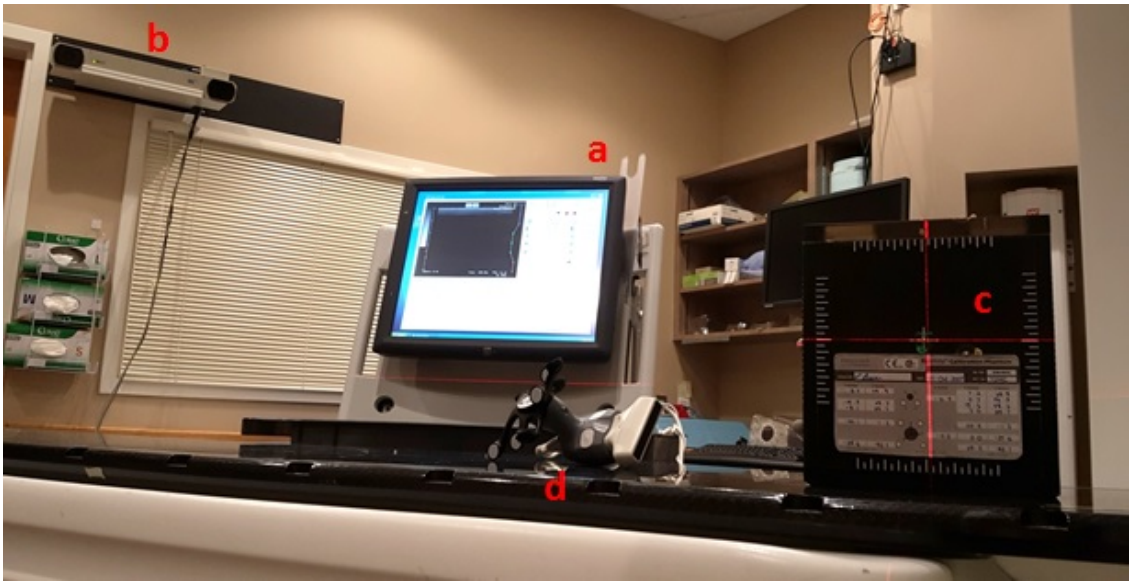

Figure 3.6: (a) The Clarity US system set up in the CT room for QA. (b) The IR camera is mounted on the wall at the inferior side of the CT bed. (c) The calibration phantom is positioned on the bed, centred on the CT's isocentric lasers. (d) The transducer with mounted IR markers (Figure 3.5) acquires images of the sphere in the phantom, displaying the position and volume in the reconstruction (Figure 3.8).

transducer, the acquired US images and 3D reconstruction have positional information in the same coordinate system as the CT images, implicitly spatially registering the two image sets without requiring any automated image registration techniques. A demonstration of the system's set up for QA is shown in Figure 3.6.

Calibration and Commissioning

For the patient data presented in Chapter 5, images were acquired using the Clarity US System at the BCCA - Vancouver Island Cancer Centre for a previous study of seroma definition for APBI treatment planning by Berrang *et al.* [36]. Shortly after this previous study, the system was decommissioned. The decommissioned system was transferred to the BCCA - Centre for the Souther Interior (CSI) where it was reconstructed in order to acquire images of PBSI patients for the study of the impact of seroma delineation on seed placement accuracy (Chapter 6).

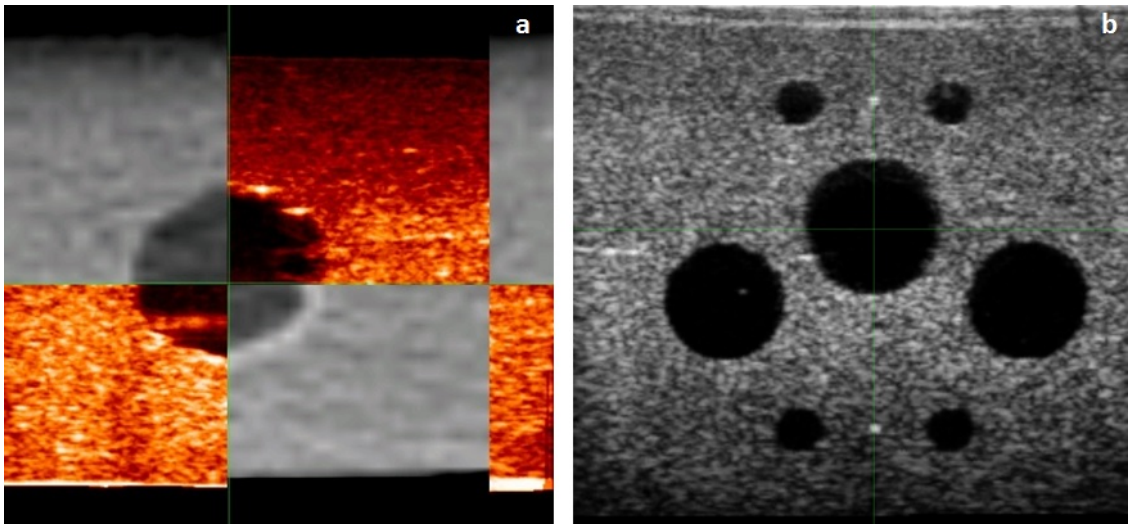

Figure 3.7: (a) Fusion of CT (gray) and 3DUS (red) images using the implicit registration of the Clarity system. A homogeneous sphere embedded in a gelatin phantom has excellent spatial correspondence (<1 mm at the walls) between the image sets. Slight differences in the boundary region appears on the right side. (b) US image of the QA phantom, with a sphere (1.2 cc) at the center and 4 rods used for calibration.

The Clarity system was originally designed with several ceiling mounted components. The system was re-built into a contained mobile unit, shown in Figure 3.5a, and re-commissioned. The system's software contains standard calibration and QA tools which make use of the QA phantom (Figure 3.7). The phantom contains a series of rods which are imaged and used to calibrate the positions in the US images to the CT room coordinates, based on the spatial registration of the phantom with the tracking system. Evaluation of the accuracy of the system's reconstruction and registration was performed in several phantom studies. The sphere in the QA phantom was imaged using the US system and then the phantom was scanned with the CT, without adjusting it's position. Both image sets were exported to MIM Sym-

phony and the implicit registration was verified by comparing the centroid location of the sphere on each modality. Further evaluation of the registration was performed by constructing phantoms composed of gelatine and muscoloid fiber (for contrast) [74] and assessing the fusion between CT and US (Figure 3.7). Small water filled balloons were suspended in the phantoms to simulate the localization of a seroma. Phantoms were imaged using CT and US in the same position with the tracked system and co-registered in MIM Symphony to ensure that the position of the balloon could be accurately localized relative to its position on CT. Table 3.1 summarizes the registration accuracy based on the phantom studies after the final system calibration. Overall, the re-commissioned system's registration was observed to be accurate to approximately 2 mm, including uncertainties related to positioning and speed of sound in the phantom studies, consistent with the expected accuracy of the system based on previous studies [36, 69–71, 75]

Table 3.1: The positional differences in the ML, AP, SI directions (Δx, Δy, Δz, respectively) between the centroid location of volumes in co-registered CT and 3DUS images. Imaged phantoms include the calibration phantom in different orientations (Cal), a block phantom with 3 embedded spheres (Block), and a gelatin breast phantom with simulated seroma (Breast)

	Δx (mm)	Δy (mm)	Δz (mm)	Total (mm)
Cal 1	-0.2	0.5	1.1	1.2
Cal 2	0.6	-0.3	-0.5	0.8
Cal 3	-0.4	0.1	-0.5	0.6
Block 1	1.6	1.0	0.3	1.9
Block 2	1.1	1.4	0.3	1.8
Block 3	1.6	0.9	-0.4	1.9
Breast	-1.5	-0.8	-1.3	2.1
Mean	0.4	0.4	-0.1	1.5
SD	1.1	0.8	0.8	0.6

The system also includes an automatic segmentation technique, similar to the one described in Section 2.3.3. Segmentation is performed by acquiring an US scan of the phantom, and manually identifying the position of the sphere by selecting 4 points around the perimeter in the central slice. The software then automatically contours the sphere in the reconstructed image, displaying volume and centroid position relative to the CT's origin (Figure 3.8). The volume and centroid positions were used to QA the system, based on their agreement with the baseline values determined by CT, before patient image acquisition was performed. The reconstructed images were

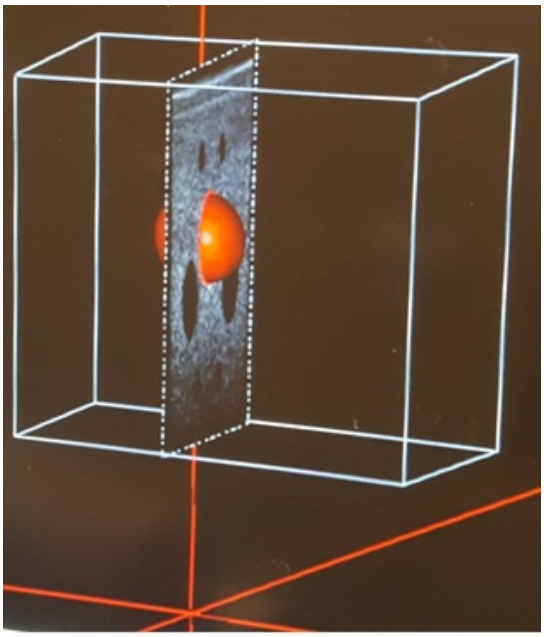

Figure 3.8: Automated segmentation of the spherical volume in the calibration of the phantom relative to the CT's origin (red intersection). The white box represents the reconstructed 3D volume, displaying one slice of the 3DUS image.

aligned within 1 mm in each direction (ML, AP, SI) and the volume was within 3% of the baseline value of 1.2 cm^3 in each of the QA procedures before patient imaging was performed.

3.2.2 Patient Image Acquisition

Image acquisition of co-registered CT and US images begins by positioning the patient in their planned treatment position. For breast scanning, patients are positioned on the angled breast board with the ipsilateral arm raised and extended, as for CT simulation for breast EBRT [36]. Following the standard PBSI evaluation and CT scanning procedure (Section 2.4.2) the US acquisition was performed. The patients were instructed to remain still after the CT scan in order to minimize errors in the registration due to patient motion. The CT bed was positioned to re-align the markings on the patients with the isocentric lasers such that breast is in the same coordinates as in the CT scan, allowing for implicit registration of the 3DUS and CT images.

An initial assessment of the imaging volume was performed with the US to identify the appropriate scanning location and to adjust the depth and contrast settings on

the system to achieve a high quality visualization of the seroma, using coupling gel to maintain good contact between the transducer and skin. The 3DUS scan was subsequently performed by a skilled physician by positioning the probe at the start of the scanning volume (generally inferior of the seroma), beginning the image collection, and sweeping the probe across the seroma. In order for accurate image reconstruction to be achieved, continuous line of site from the IR camera to the markers on the probe must be maintained throughout the entire scan. The system would notify the user if detection was ever lost, prompting a repeated scan with adjusted probe positioning. After the scan, a visual inspection of the reconstructed volume was performed to ensure that the entire seroma had been captured and that contact was never lost with the skin surface, creating signal loss and artifacts in the image (Section 2.2.2). Due to the application of gel to the transducer and skin surface, the scan could be completed smoothly with very little pressure, minimizing compression and deformation of the breast. When a high quality image had been acquired, the 3DUS and CT images were imported into MIM Symphony and registered using their shared coordinate system for analysis.

3.2.3 Contouring and Assessment

Evaluation of the use of 3DUS in the PBSI procedure required seromas to be identified on the US and CT images and their visualization quantified. As described in Section 2.4.2, the seroma on CT is delineated by an oncologist as part of the clinical PBSI planning procedure. Delineation of the seroma on 3DUS is not currently a part of the PBSI procedure, as US is not used in treatment planning, but could similarly be identified on the images acquired with the Clarity system. Seromas were contoured on US using standard clinical guidelines, defining the seroma as the dark anechoic region in the image representing the homogeneous fluid-filled cavity plus the hypoechoic wall of the cavity when visible [36].

Contouring bias may occur from a single user, with high-inter observer variability in seroma contouring previously observed [36, 62, 76, 77]. High inter-user variability in seroma contouring has been shown to be associated with reduced clarity of the seroma on both CT and US, stemming from the volume and location of the seroma in the breast, the presence of dense breast tissue, and greater amounts of scar tissue and stranding resulting from the lumpectomy procedure [36, 61, 76]. Multiple independent contours were used to quantify the visualization of the seroma as well as to provide

consensus contours to use for further analysis of 3DUS in PBSI.

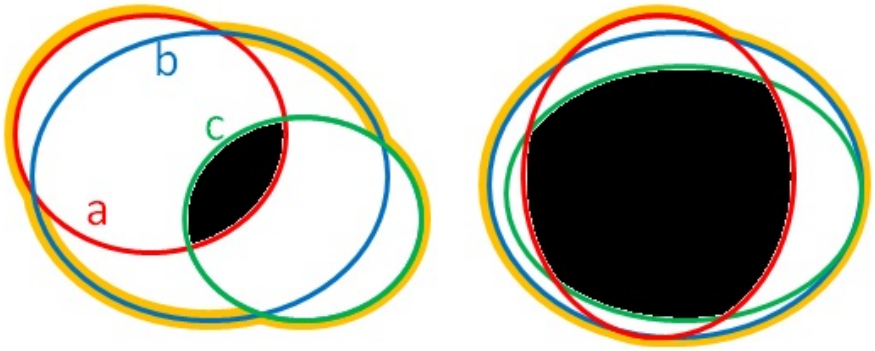

Figure 3.9: Three contours (a,b,c) exhibiting low (left) and high (right) conformity, defined by the ratio of the overlapping volume (black) to the total volume encompassed by all of the contours (yellow)

Based on the multiple independent contours, the inter-user conformity was assessed to quantify the visualization of the seroma on each modality in each image set. The conformity index (CI) was defined as the ratio of the overlapping volume to the total encompassing volume of all contours. For multiple contours (a, b, c), as shown in Figure 3.9, Boolean AND ($\wedge$) and OR ($\vee$) operators were used to define the overlapping and total volumes and the CI was calculated by

$$CI = \frac{Volume(a \wedge b \wedge c)}{Volume(a \vee b \vee c)}. \tag{3.6}$$

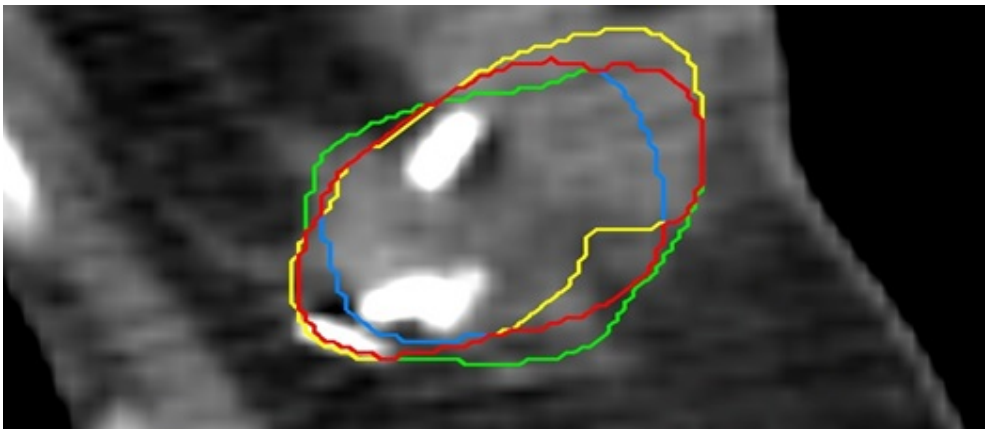

Figure 3.10: Three independent delineations of a seroma (blue, yellow, green) and the resulting consensus contour (red), the middle contour at each point.

In order to reduce user bias from assessment of the differences between the seromas delineated on CT and US, consensus volumes were created using the individual users' contours [36]. The consensus contours were created by observing the overlapping volumes and taking the middle contour at each point in the image, as shown in Figure 3.10. The resulting volume is therefore delineated as the median of the 3 contours, determined by

$$Consensus = (a \vee b) \wedge (a \wedge c) \wedge (b \wedge c). \tag{3.7}$$

The consensus contours on CT and US were defined as CTV_{CT} and CTV_{US}, respectively. To assess the difference between the seromas delineated on the two modalities, CTV_{US} was transferred to the CT images using the implicit registration of the 3DUS system. The inter-modality CI could therefore be calculated for the two consensus contours, similar to Equation 3.6. Positional agreement between the CTVs could also be assessed by calculating the centroid (center of mass) location in the registered coordinates and evaluating the total and directional differences.

3.3 3D Ultrasound System for Permanent Breast Seed Implant Guidance

To realize substantial improvement to the PBSI delivery procedure, an intra-operative 3DUS scanning system that can spatially register the template to the imaging view is required. Such a system, similar to the established prostate brachytherapy systems (Section 2.3.2), would allow for visualization of the planned needle positions at depth. A virtual representation of the template overlaid on live guidance images allows for adjustments to needle positioning to be made to better match their planned positions before depositing seeds, thus potentially increasing the accuracy and adaptability of PBSI. A novel 3DUS scanning system was developed at The Imaging Research Laboratory (Robarts Research Institute, Western University) with guidance from the BCCA PBSI research group about the design characteristics required to make a system specifically for PBSI guidance.

3.3.1 Scanner Design

The PBSI 3DUS system was designed to provide fast, automated acquisition specific to breast imaging. The scanner was designed similarly to the system developed for intra-operative 3DUS in breast HDR brachytherapy, described in Section 2.3.3. Shown in Figure 3.11, the housing of the scanning system contains a motor which drives the translation and rotation of a mount while mechanical encoders record the position. An US transducer is fixed in the mount, and connected to a standard 2DUS imaging system. Thus, the probe is mechanically translated (5 cm linearly) and rotated (60^o) with it's orientation relative to the scanning system tracked in space [78]. In order to avoid contact loss during imaging, and to provide minimal uniform pressure over the scanning range to prevent deformation, a thin (1.5 mm) plate of ultrasound transparent polymethylpentene plastic (TPX) is fixed to the bottom of the scanning system [53, 78]. The TPX plate is machined according to the physical shape of the transducer, allowing for smooth motion and constant contact with the application of coupling gel.

During scanning, the image displayed on the 2DUS system is digitally outputted and recorded by a capture device at predefined intervals, based on the scan speed and frame rate. The mechanical encoder measurements are recorded at each image capture interval. Based on the position of the transducer, the captured images are registered onto planes in space, filling out a volume with each successive image ($\sim$150 total), thus creating a 3D image. The software used for the reconstruction allows for viewing of the US images in re-sliced geometries as well as distance measurements and volume segmentation [53].

While the PBSI 3DUS system acquires and reconstructs images similar to previously developed 3DUS techniques, the principal component that makes it unique to PBSI is the method of registration between the volumetric image and the treatment template. Unlike in prostate brachytherapy, the template is not physically fixed to the scanning system and is not necessarily positioned orthogonally to the imaging planes. The PBSI 3DUS system features a localization arm with a spherical tip mounted on the lateral side of the scanner housing, shown in Figure 3.11. Each joint of the arm contains a magnetic encoder that measures the angle. Based on the 3 angles and the distance of each segment of the arm, the center of the sphere at the tip can be localized relative to the base of the arm. Therefore the localization arm can be used to identify the template position and orientation relative to the scanning system by

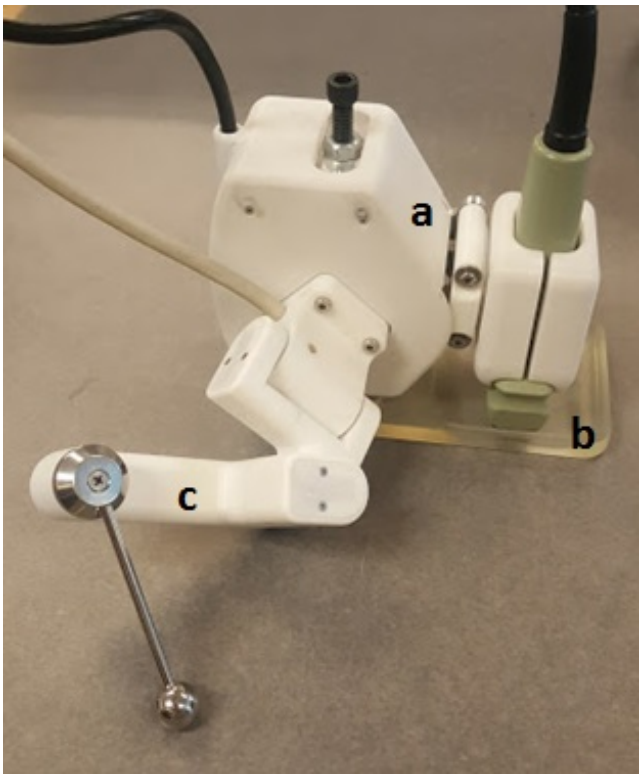

Figure 3.11: 3DUS scanning system designed for PBSI intra-operative guidance. (a) The scanner housing contains a motor which drives the mounted transducer across the (b) TPX plate. (c) The localization arm with 3 encoded joints and a spherical tip is mounted to the side of the scanner, used for template registration. The images, scanner position, and arm encoder values are recorded by a separate computer which reconstructs the image.

measuring the positions of the tip at known locations relative to the template.

Template visualization in the 3D volume is performed by the transformation of the template coordinates into the imaging coordinate system. The locations of divots used to seat the arm's tip are transformed to the arm's coordinate system using a point-based rigid registration, generating a 3D transformation matrix ($T \rightarrow A$) similar to Equation 3.1. A transformation of the arm's coordinates to the coordinate system established by the scanner ($A \rightarrow S$), with the origin at the center of the TPX, was generated by measuring the locations of divots with the arm at known locations relative to the scanner's origin and registering the points [78]. Finally, a transformation of the scanner's coordinates to the imaging coordinates ($S \rightarrow I$) was generated by mounting the scanner to a test jig with intersecting nylon strings at known locations, identifying the points in the reconstructed image, and performing

a point-based registration [78]. Therefore the location of any point in the template coordinates (x_T, y_T, z_T) (template position and depth) could be transformed to the imaging coordinates (x_I, y_I, z_I) by combining the 3D transformation matrices

$$\begin{bmatrix} x_I \\ y_I \\ z_I \end{bmatrix} = [[T \rightarrow A] \times [A \rightarrow S] \times [S \rightarrow I]] \times \begin{bmatrix} x_T \\ y_T \\ z_T \end{bmatrix} . \tag{3.8}$$

Using this transformation, the extrapolated template positions within the imaging volume can be localized and displayed in the 3D image, analogous to the visualization of the template in prostate brachytherapy, as shown in Figure 3.12.

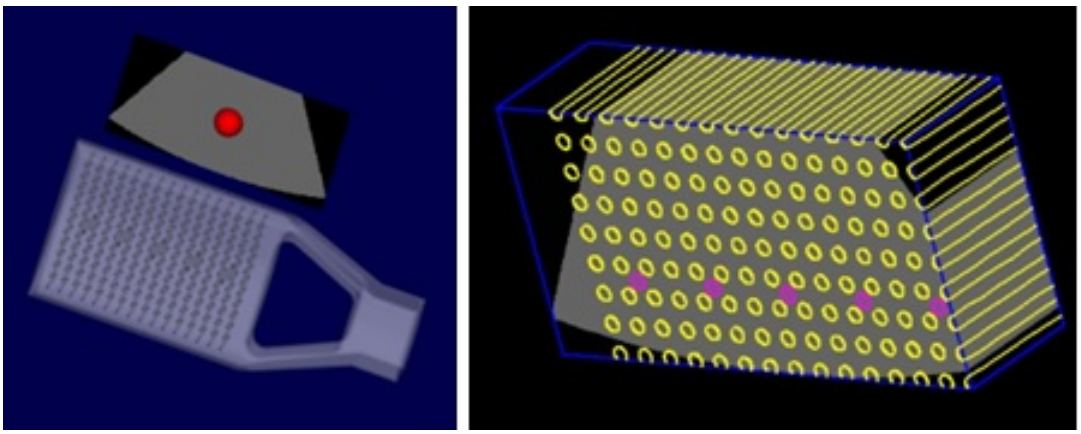

Figure 3.12: Registration of the template with the imaging volume allows for the virtual representation of the template positions throughout the image.

3.3.2 Commissioning

Validation of the image reconstruction methods of the PBSI 3DUS scanning system was previously performed by the developers using linear and volumetric measurements, ensuring that imaged distances in the reconstruction planes accurately represent the actual known distances [78]. Linear reconstruction accuracy was quantified by imaging a grid of nylon stings and comparing the measured and known distances. In order to achieve accurate distance measurements in the 3DUS images, the grid was submerged in fluid composed of water and 7% glycerol by weight, which produces a medium with a speed of sound of 1540 m/s [52, 79–81]. Volumetric accuracy was quantified by embedding known volumes into a solid phantom, composed of water, agar (3.5% by weight) and glycerol (8% by weight) to achieve the correct speed of

sound [52, 79–81]. The segmented volumes were compared to the known volumes, established through titration measurements [78]. The reported median linear reconstruction accuracy for the initial development of the imaging system, using the described methods, was less than 1.4% (95% confidence interval of 2%) in all directions, and the mean volumetric accuracy was 4.1% [78].

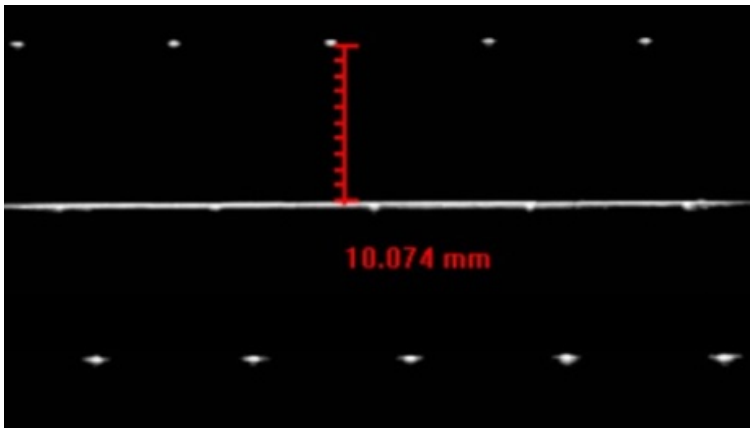

Figure 3.13: Reconstructed 3DUS image of a grid of nylon strings. The distance between strings oriented transverse (dots) and along (line) the plane of imaging is measured to be ∼10.1 mm.

After initial verification of the scanning system, a second 3DUS scanner was produced by the developers, identical in scanning and reconstructing methods, for use in the investigation of improved intra-operative guidance in PBSI (Chapter 7). The use of the scanning system with the clinical ultrasound system (1202 Flex Focus Ultrasound System, BK Ultrasound) and transducer (Linear Array 8811, BK Ultrasound), used in the PBSI procedure and for the presented research, was assessed. QA of the system, described in Section 7.2.1, was performed to ensure reconstruction accuracy consistent with the developer's specifications through linear measurements of a string grid (Figure 3.13) in a glycerol-water solution (as described above), and volume reconstruction of a sphere embedded in a solid agar and glycerol phantom [78, 81].

As discussed further in Chapter 7, imaging of needles was performed to evaluate the template registration accuracy. In order to reduce the uncertainty associated with the bending of a needle as it travels through a solid medium, and non-deflecting liquid medium was used for imaging. By inserting needles through a liquid medium, they could be reasonably assumed to travel in a straight line from the template position. For all subsequent measurements, the medium was composed of water and 7.25% by volume isopropyl alcohol, at $\sim 22^{o}$C. This mixture has been shown to exhibit a

speed of sound of 1540 m/s, ensuring accurate displacement measurements in the US reconstruction [82]. Before each experiment, a subset of measurements in the string grid were performed in order to insure the speed of sound was correct, resulting in distance measurements within 1% of expected values.

Chapter 4

Evaluation of Seed Placement Accuracy in PBSI

Improvements in the PBSI procedure to increase accuracy, confidence, and adaptability first requires an evaluation of the accuracy of the current technique. By identifying the errors and uncertainties in the procedures, the areas which have the greatest impact on the technique can be identified. Initial assessment of the PBSI procedure was performed through an evaluation of seed placement accuracy of a cohort of patients treated with PBSI at the BCCA - Centre for the Southern Interior. This chapter details the analysis of seed placement in the clinical procedure and the resulting impact of seed placement on the treatment. The locations of implanted seeds are assessed relative to the planned positions for the cohort of patients and for individual implants to evaluate any systematic trends in the implant technique and relative to the location within the breast and quantify random uncertainties in seed placement. The resulting impact of seed placement accuracy on the treatment is examined. The presented study has been adapted from the publication of this work by the dissertation's author in the *International Journal of Radiation Oncology, Biology, Physics* (doi:10.1016/j.ijrobp.2016.01.049) [60].

4.1 Introduction

As outlined in Section 2.4.3, initial implementation of PBSI has been successful, with acceptable target coverage and toxicities, and recurrence rates equivalent to established whole breast irradiation techniques. The benefits of this treatment option

for a broad patient population are clear given the early results and the convenience of a single day treatment. However, the procedure has not been widely adopted and concerns have previously been expressed regarding uncertainties in seed placement accuracy [34]. In order to promote implementation, the validity of these concerns must be examined. In this study the issue of seed placement accuracy is addressed by quantifying the differences between the planned and implanted seed positions. The resulting effects of such differences on initial dosimetry are evaluated to determine the impact of seed placement on the treatment.

No assessments of the uncertainties in seed placement accuracy have previously been performed and the sources of error with the greatest effects on the technique are unknown. Developments to improve the PBSI procedure therefore rely on a thorough assessment of the current technique in order to determine the components which must be improved. By quantifying the seed placement accuracy, uncertainties in the treatment delivery may be identified. These uncertainties can be addressed through further developments to improve the overall implant accuracy, potentially increasing the robustness and adaptability of PBSI.

4.2 Methods

4.2.1 Patient Implants

Between May 2012 and October 2015, 30 women were treated with PBSI as part of an ongoing single-institution clinical trial. Patients receiving treatment met the criteria as outlined in Section 2.4.1. All patients had a lumpectomy to remove ductal carcinoma *in situ* or low-risk invasive ductal carcinoma with clear margins and no evidence of metastatic disease. Assessment at the time of CT simulation found the seromas to meet the established technical eligibility requirements including a clearly visible seroma on CT and US that was less than 3 cm in diameter and in a position feasible for implant.

The treatment planning and delivery methods for PBSI were described in Section 2.4.2. The implants evaluated in this study were planned and delivered using the standard procedure. In brief, the seroma was contoured on CT and expanded by 1.25 cm to generate the PTV, cropping to the chest wall and 5 mm from the skin surface. Needle insertion angle and depth were set by the planned fiducial needle. Loaded needle locations and seed positions were planned to achieve optimal dose coverage,

as described in Section 2.4.2. All treatments were planned using a median 2.5 U seed activity (range, 2.4-2.7 U) and line source geometries.

Following the markup procedure, the patients were positioned in the OR and setup adjustments were performed to replicate the simulator positioning. The fiducial needle was inserted under free-hand 2D US guidance. The stranded ^{103}Pd seeds were subsequently implanted to their planned positions and a post-implant CT was performed, replicating positioning from the planning CT using the breast board and tattoos. Day-0 seed positions were identified to perform the standard post-implant verification process. Dose-volume histograms were calculated for the post-implant seroma, and evaluative target volume (ETV) defined as the seroma plus 0.5 cm, and surrounding normal tissue, using point-source calculations. Day-0 CT images are used here to assess initial seed placement and dosimetry.

Seed placement was evaluated for 20 of the 30 implanted patients (13 left breast, 7 right breast). The other implants were excluded from this study owing to any ambiguity in the image registration, intraoperative changes to the plan, or seed matching which may have incorrectly influenced the results of the placement evaluation procedure.

4.2.2 Seed Placement Accuracy

After clinical dosimetry, a retrospective analysis was undertaken to determine the positions of the implanted seeds relative to their planned positions. Using the methods described in Section 3.1.1, a region of interest (ROI) defined as the seroma plus a 1 cm margin was aligned in the planning and day-0 CT images. Registration was quantitatively validated by comparing the pre- and post-implant locations of surgical clips within the ROI in 9 patients, and any noted differences were correlated with differences between the planned and implanted seed positions.

The seed matching software described in Section 3.1.1 was subsequently used to determine the positional differences between the planned and implanted seed positions (seed displacements). Coordinates for both the planned and implanted seed positions, contours, and the transformation matrix derived from the registration of the 2 image sets were exported from MIM Symphony for each implant. The 2 seed clouds were superposed using the transformation matrix (Section 3.1.1) and post-implant seeds for each patient were manually matched to their corresponding planned locations (Figure 4.1). Because of the stranded nature of the seeds, the matching process was

unambiguous for all cases included in this study.

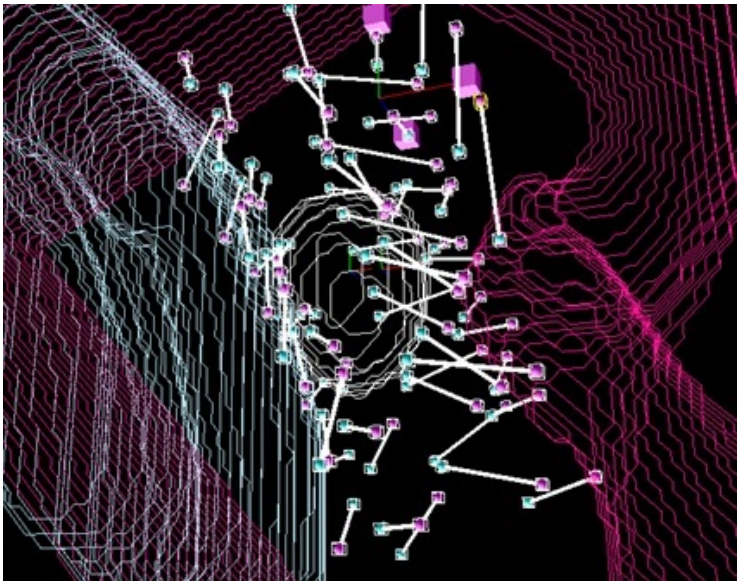

Figure 4.1: Visualization of the matched planned (blue) and implanted (pink) seed positions. Connecting lines (white) indicate matched seed pairs. The purple, blue, and white contours correspond to the skin surface, chest wall, and seroma, respectively.

The displacements of 1370 implanted seeds from 20 patients (median 67 seeds per patient; range 52-94) were determined. Mean total displacements were calculated over all patients and within each individual implant. Directional displacements were evaluated using 2 frames of references, as described in Section 3.1.3 (Figure 3.4): standard room coordinates (ML, AP, SI) and needle coordinates, defined by the insertion direction. Positive values were defined to be in the lateral, anterior, and superior directions in room coordinates, and the shallow, up, and right directions in needle coordinates. Mean directional displacements and the contributions of random errors relative to these systematic displacements were computed using the methods described in Section 3.1.3. Implanted seeds were further classified into 4 anatomic regions (Figure 4.2) seeds in the plane closest to the chest wall (Chest Wall), seeds in the plane closest to the skin (Skin), seed implanted through the seroma (Seroma), and seeds at the anterior boundary of the seroma (Edge of Seroma). Mean values for the total and directional displacements of the seeds, using needle coordinates, were calculated within these regions to determine the effect of anatomic location on placement accuracy.

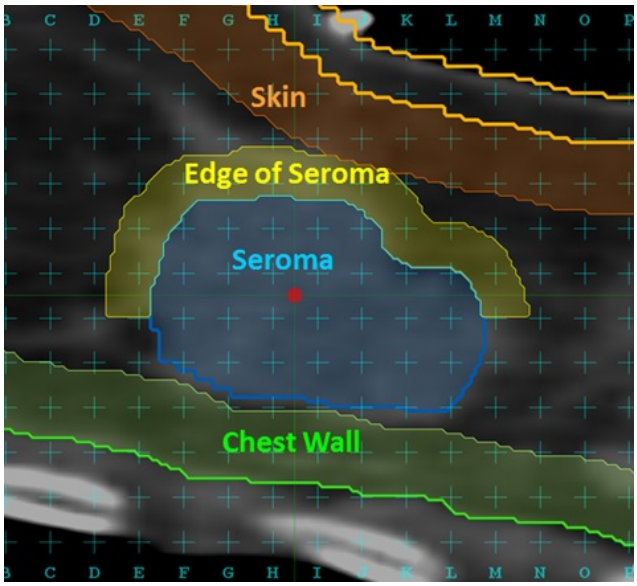

Figure 4.2: Visualization orthogonal to the insertion direction demonstrating the anatomic regions relative to the skin (orange), seroma (blue), and chest wall (green).

4.2.3 Effects of Seed Placement on Treatment

Post-implant dosimetry was assessed on day-0 CT images to evaluate the initial treatment quality relative to the calculated seed displacements. The volume of the ETV receiving at least 90% of the prescribed dose (V_{90}) was calculated, where a V_{90} of >90% is considered acceptable coverage for APBI [83]. The maximum dose delivered to a 0.2 cc volume ($D_{0.2cc}$) in a 2 mm thick skin layer [63], V_{150} and V_{200} within the ETV, and maximum point rib dose were also evaluated to further assess the treatment.

4.3 Results

4.3.1 Image Registration Accuracy

The median (range) time from surgery to planning CT was 60 (37-105) days, and from planning to the day-0 CT was 22 (15-43) days. The mean positional agreement between surgical clips within the region of interest (39 clips total: median 4 clips per patient; range 1-7) from planning to implant was 1 ± 1 mm and was independent of location within the breast. The clip positional agreements from each individual patient are summarized in Table 4.1. The observed clip displacement was consistent

with values recorded previously for clip migration [84] and validates the accuracy of the rigid registration process. A strong correlation between the magnitude of clip displacement and the number of days from the planning CT to the day-0 CT was observed ($r = 0.83$ $p = 0.01$), as shown in Figure 4.3. No correlation was found between displacement of clips and seeds ($r = -0.01$).

Table 4.1: Mean (SD) differences in clip positions for each of the evaluated implants with N identified clips within the registration ROI.

Implant	ML (mm)	AP (mm)	SI (mm)	Total (mm)
N = 4	-1 (2)	-1 (2)	0 (0)	2 (1)
N = 7	1 (1)	2 (1)	0 (1)	3 (1)
N = 4	0 (1)	0 (1)	0 (0)	1 (1)
N = 1	0	-1	0	1
N = 4	0 (0)	0 (1)	0 (0)	1 (0)
N = 6	0 (1)	0 (1)	0 (0)	1 (0)
N = 4	0 (1)	1 (1)	0 (0)	1 (0)
N = 4	0 (1)	0 (0)	0 (1)	1 (0)
N = 5	-1 (2)	1 (1)	0 (0)	2 (1)

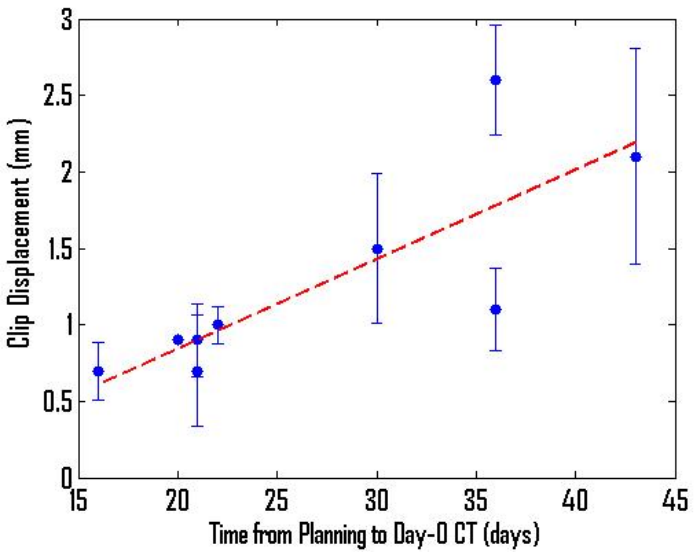

Figure 4.3: Relationship between the magnitude of clip displacement and the number of days from the planning to day-0 CT scans.

4.3.2 Seed Placement Accuracy

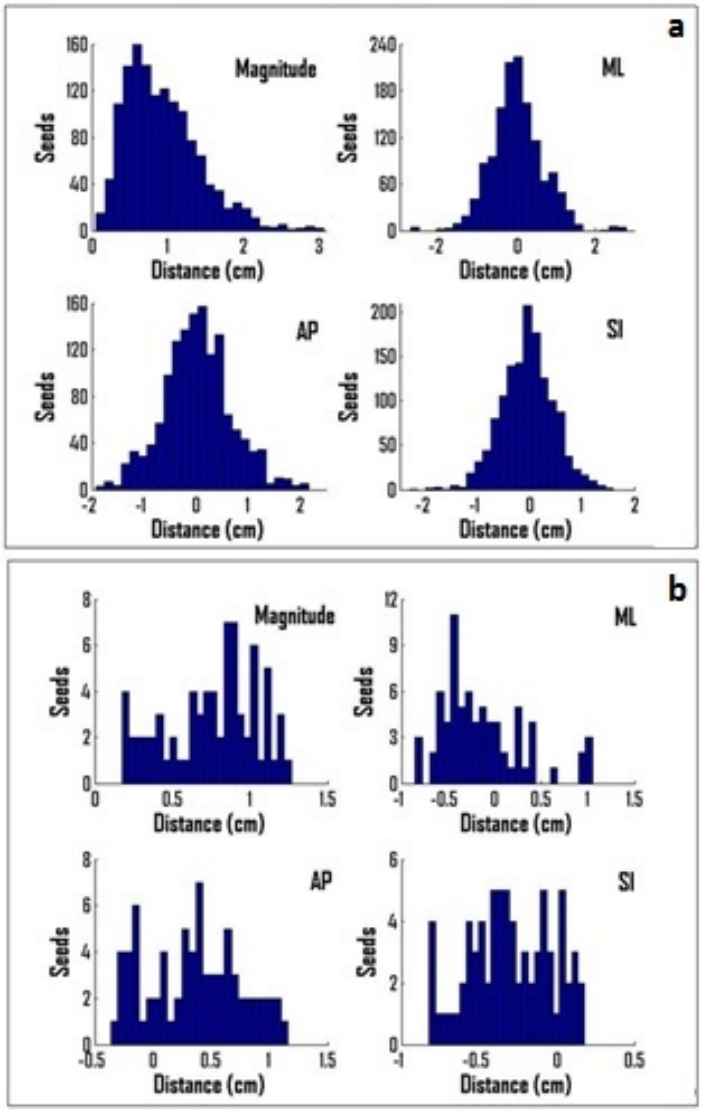

Figure 4.4: Histograms of the magnitude and directional (ML, AP, SI) seed displacements for the (a) cohort seed population and (b) for a single patient. The directional distributions are normal and centered at zero for the cohort but not for the individual patient.

Figure 4.4a shows the total and directional distributions of the aggregate seed population (all patients). The mean (± SD) total displacement was 9 ± 5 mm. There are no systematic displacements in room coordinates, and all directional displacements appear normally distributed around zero; means are 0 ± 7 mm, 0 ± 7 mm, and -1 ± 5 mm in the ML, AP, and SI directions, respectively. For individual

patients, mean total seed displacements ranged from 6 ± 3 mm to 16 ± 6 mm, with individual seeds placed between 1 and 31 mm from their planned positions. In contrast to the whole population, for individual implants systematic displacements are observed, as is shown in Figure 4.4b. In this example, mean shifts in the directional displacement of the seeds are -1 ± 5 mm, 4 ± 4 mm, and -3 ± 4 mm, in the ML, AP, and SI directions, respectively. The mean directional displacements imply that intra-patient systematic offsets do occur during the procedure. However, the magnitude of shifts varied widely among patients (for example, from -7 to 8 mm in the AP direction) and thus do not amount to any inter-patient trends. Subtraction of the mean displacements from the individual implant distributions gives an approximate mean random component to seed displacement of 7 ± 4 mm. This signifies that a significant component of observed seed displacements is due to random variations in seed placement.

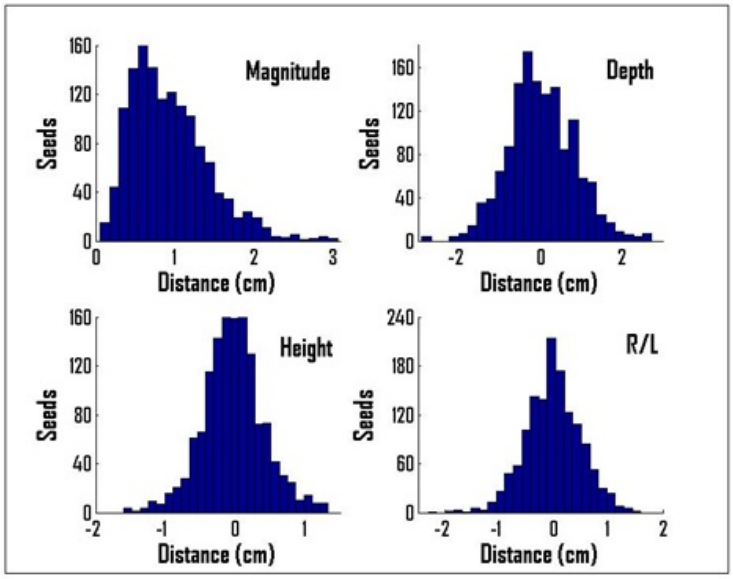

Figure 4.5: Histograms of the magnitude and directional seed displacements in the rotated needle coordinate system for the entire seed cohort.

Figure 4.5 shows seed displacement distributions from the entire seed population in the needle coordinate system. Similar to the room coordinate system (Figure 4.4a), the directional distributions in Figure 4.5 are centered around zero in the depth (0 ± 8 mm), height (0 ± 4 mm), and right-left (0 ± 5) of needle insertion. The spread of the distributions is greatest in the depth direction, owing to variations in the needle insertion distance but was not biased in any particular direction.

4.3.3 Seed Placement within Anatomy

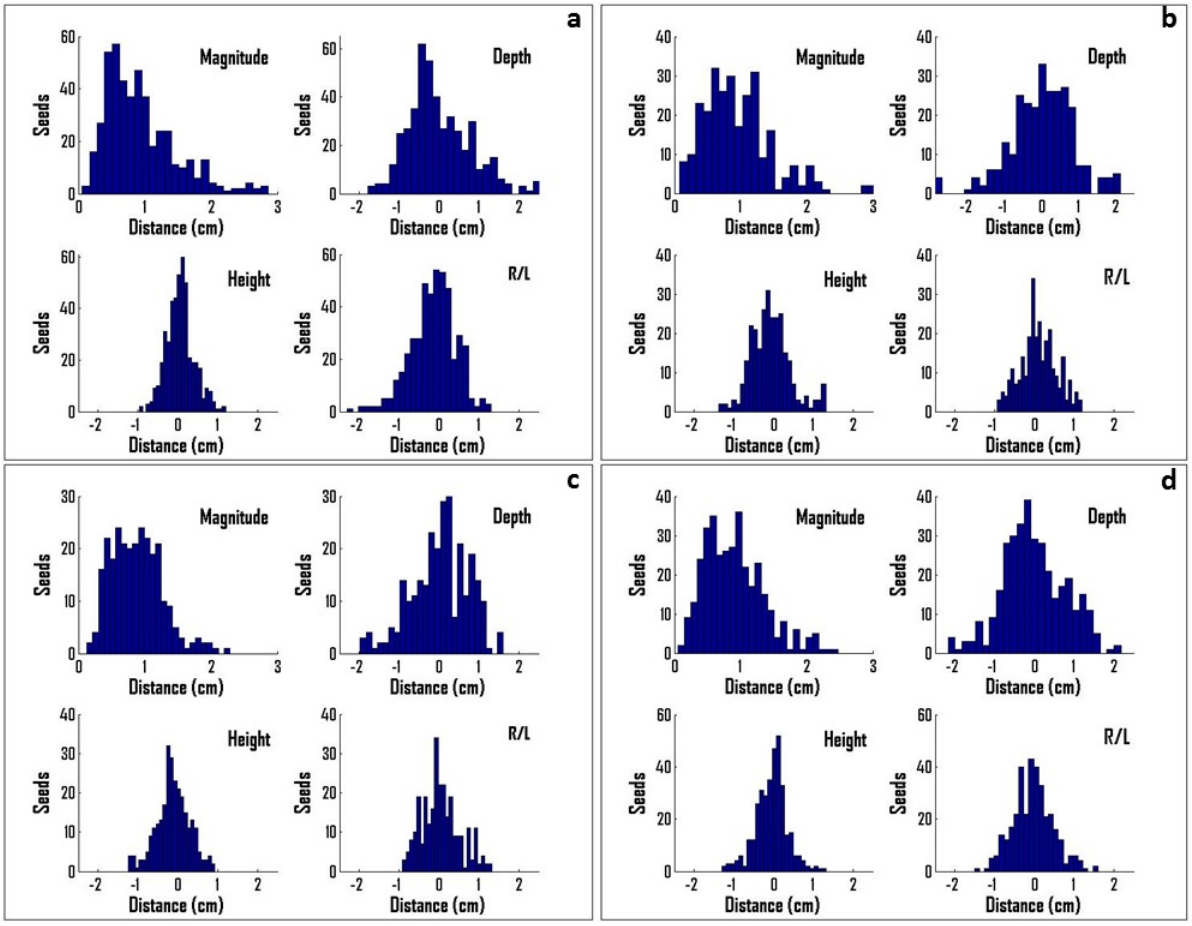

Figure 4.6: Histograms of the total and directional seed displacements, measured in needle coordinates, in the 4 anatomic areas: (a) Chest Wall, (b) Skin, (c) Edge of Seroma, and (d) Seroma.

Mean total displacements were 9 ± 4 mm, 9 ± 4 mm, 9 ± 5 mm, and 10 ± 5 mm for seeds implanted within the Seroma, Edge of Seroma, Chest Wall, and Skin regions, respectively (Table 4.2). Total displacements within the anatomic regions were not significantly different from the mean displacements for all seeds (9 ± 5 mm), regardless of anatomic position ($p = 0.34, 0.07, 0.82$, and 0.68 in the Seroma, Edge of Seroma, Chest Wall, and Skin regions, respectively). The largest variation in placement occurs along the needle insertion direction in all regions. Figure 4.6 shows the total and directional distributions, measured in the needle coordinates, of seed displacement within anatomic regions. The directional distributions within the anatomy contain several small mean direction shifts, most notably in the height of

Table 4.2: Summary of the mean (SD) aggregate seed displacements (total and directional) in the 4 anatomic regions

Region	Depth (mm)	Height (mm)	RL (mm)	Total (mm)
Chest Wall	0 (8)	1 (3)	-1 (6)	9 (5)
Skin	0 (8)	-1 (5)	1 (5)	10 (5)
Edge of Seroma	0 (7)	-1 (4)	0 (4)	9 (4)
Seroma	0 (8)	0 (4)	0 (5)	9 (4)

insertion in Skin and Edge of Seroma seeds (-1 ± 5 mm and -1 ± 4 mm, respectively). Figure 4.6 shows a large number of seeds displaced towards the negative height within these areas, corresponding to seeds implanted downward from their planned positions, away from the skin. Conversely, seeds within the Chest Wall region were seen to be on average implanted upward from their planned position (1 ± 3 mm). Displacement in depth was seen to vary widely within the cohort, but no direction was favored, with a mean of 0 ± 8 mm in all regions except for Edge of Seroma (0 ± 7 mm).

4.3.4 Dosimetry

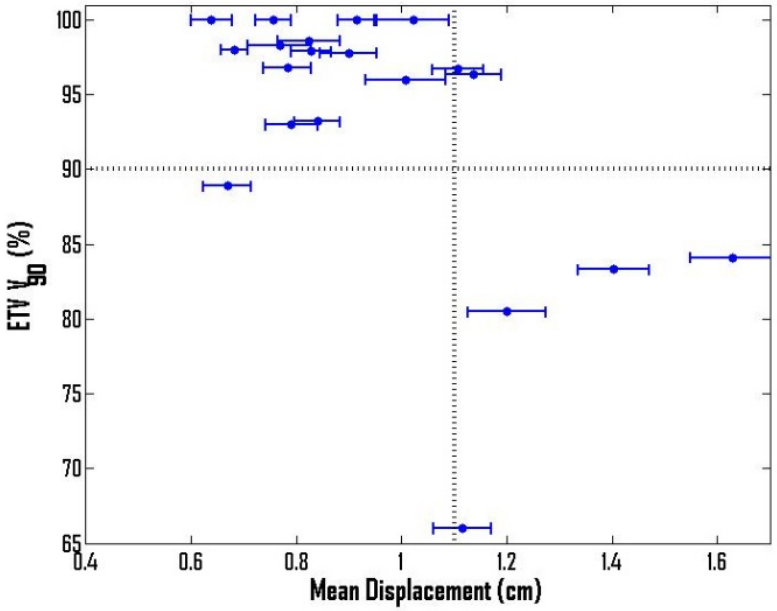

Figure 4.7: The V_{90} of the evaluative target volume (ETV) relative to the mean seed displacement within each patient. Dashed lines represent the target V_{90} of 90% and the maximum displacement observed to give an acceptable dose (1.1 cm), with 2 close outliers.

The ETV V_{90} (Figure 4.7) ranged from 66% to 100% (median 97%) across the 20 implants assessed in this study. A $V_{90} > 90\%$ was achieved in 15 patients, and $> 95\%$ in 13 patients. Figure 4.7 also shows how dosimetry may be affected by the distance of the seeds from their planned positions. The maximum mean displacement observed that resulted in acceptable dosimetry was 11 ± 4 mm. One implant with a mean seed displacement lower than this value (7 ± 3 mm) had ETV coverage falling into the unacceptable range, but at 89% was only very slightly below the acceptable value (90%). Median ETV V_{150} and V_{200} were 75% (43%-97%) and 50% (23%-66%), respectively. Dose to normal tissues was also observed to be acceptable for the patients within this study. The median $D_{0.2cc}$ to the 2 mm thick skin layer was 80% (9%-202%) of the prescription dose, and the median maximum point dose to the ribs was 101% (2%-437%). The immediate post-implant dosimetry achieved within this study was consistent with previously reported data observing post-implant PTV V_{100} and V_{200} of 86 ± 10% and 36 ± 14%, respectively [9].

4.4 Discussion

Concern has previously been expressed regarding the uncertainty in seed placement and thus in the safety and efficacy of PBSI [34]. This stems from the assertion that large seed placement errors may result in reduced coverage of the target volume and increased chance of recurrence, or increased radiation hot spots resulting in undesirable radiation side effects, neither of which has been observed in published experience to date [10]. This study examined the validity of these concerns by evaluating the placement accuracy of seeds in the current PBSI procedure, to determine the magnitude of such placement errors and their effect on treatment dosimetry, as well as to expose any potential systematic errors affecting the treatment.

The results presented in Figures 4.4 and 4.5 show that no significant inter-patient systematic errors occur in the placement of seeds, in either coordinate system. Although systematic placement errors are absent, an overall mean displacement of 9 ± 5 mm exists in the evaluated seeds. Despite this, acceptable implant dosimetry of ETV V_{90} exceeding 90% [83] is largely maintained. Random variations in seed placement, which were shown to form a large portion of the seed displacements, do not result in net displacement, and because good ETV coverage was achieved it is unlikely that they have a significant effect on the dosimetry. The results of this study indicate that normal tissue tolerance and acceptable treatment dosimetry are achieved immediately

after the implant within the limits of the seed placement accuracy of the current PBSI procedure. A learning curve in the PBSI implant technique has been previously observed [8, 10], so placement accuracy and target coverage could potentially improve beyond the initial patients included in this study.

In contrast to the lack of systematic directional displacements observed across the entire patient cohort, mean directional displacements do occur within each individual implant. One possible explanation is that individual patient setup inconsistencies between planning and implant contribute to the seed displacements. Time lag between planning and implant could affect seroma size and shape and therefore how seeds are implanted relative to the plan, and breast density or tissue type (scar vs skin) may impact tissue deformation and needle bending during the insertion. A primary contributing factor may be the use of 2 different imaging techniques within the PBSI procedure: CT for treatment planning and US guidance for implant. Although US image guidance is used to match the patient treatment position to the planned position, the US-delineated seroma can vary in size, shape, and position compared with the seroma contoured on planning CT [36, 73, 85, 86]. Therefore, shifting the plan to align it to the US image may create a discrepancy between treatment delivery and planning location, thus introducing offsets to the seed placements.

A component of the systematic displacements could be related to the accuracy of the image registration used for seed placement analysis. However, the clips on the day-0 images were observed to be located, on average, 1 ± 1 mm from their position on the planning CT images, validating the accuracy of the registration within the target volume. Due to the finite slice thickness on the CT images (2 mm), clips were generally localized on the same SI slice, potentially artificially increasing the apparent accuracy. Clip displacements may not only be related to the registration accuracy as clip migration is a common occurrence within the breast caused by a variety of anatomical factors [84, 87]. Migration of clips over the course of EBRT (28 fractions) has previously been observed to average 1.4 mm (maximum 5.8 mm) in the direction of the center of the excision cavity [84]. Due to the correlation observed between the clip displacement and the time from planning to implant, migration is likely a factor in the observed discrepancies between the positions on the 2 CT images.

The results given in Figure 4.6 show that the anatomic location does not affect the magnitude of the displacement of the implanted seeds, thus refuting the hypothesis [34] that seeds within certain anatomic areas are prone to larger displacements immediately after their implant. A small mean vertical displacement of the anterior edge

of the seroma may indicate the seeds settling towards the seroma, but seeds placed directly in the seroma did not experience any greater displacement compared with the seeds placed in the other anatomic areas. The only notable trend was the small vertical displacements of seeds away from the chest wall and skin. This difference may indicate an operator bias to intentionally direct needles to avoid penetrating the lungs or distal skin.

Seed placement in prostate brachytherapy is estimated to be accurate to approximately 3 to 6 mm [88–91]. Although relatively smaller than the PBSI displacement observed in this study, the prostate brachytherapy procedure has advantages such as the use of US for both planning implant guidance, and the use of an US stabilizer and stepper to provide a fixed reference for implant coordinates. Thus greater accuracy in the established prostate brachytherapy technique is expected. Additionally, the robust method used in this study of registering the CT data according to the anatomy and manually performing the seed matching is more rigorous than previously presented evaluations of prostate seed implant accuracy via orthogonal films or automatic registration of the seed clouds [89, 91]. A favourable result of this study in comparison with prostate brachytherapy evaluations was the lack of any systematic displacements. Multiple prostate brachytherapy sector dosimetry studies have shown systematic under-dosing of the prostate anterior base [92–94]. Seeds being pulled toward the apex during implant, in part owing to needle drag [92], did not have an analog in this study, and thus PBSI seed displacement seems to be more random and unique to each individual patient.

The success of the PBSI procedure relies not only on the accurate placement of seeds, but whether the seeds remain in the desired location over the course of the delivery. Pignol *et al.* have observed an increase in the V_{100} and V_{200} within the PTV day 0 to day 60, likely due to the reduction of edema over time bringing the seeds closer together [31, 95]. Later-date dosimetry will be influenced by seed motion. Determination of how seeds migrate owing to factors such as recovery or motion of the breast, and how migration relates to initial seed placement is left for future exploration.

Continued technique developments in PBSI may provide improvements in seed placement accuracy. The results of this study have shown significant contributions of both random and systematic placement errors to the overall accuracy. As mentioned above, biases associated with attempting to center the CT-planned implant on the US visualized seroma could potentially be reduced by implementing co-registered 3DUS

imaging into the planning procedure, thus allowing patient setup to be performed using more analogous images. Random uncertainties were observed to be relatively consistent among the different implants, and were particularly apparent in the depth of needle insertion. Improved image guidance during the treatment delivery, similarly to the well-established prostate brachytherapy techniques, may further reduce seed displacements by providing precise needle and plan localization at depth. These methods to potentially reduce systematic and random displacements are explored in the following chapters.

4.5 Conclusions

Permanent breast seed implant brachytherapy seeds were found to be placed, on average, 9 ± 5 mm from their planned locations. No significant trends or systematic errors were observed in the placement of seeds, including seeds implanted directly into the seroma cavity. Even with the observed discrepancies in seed placement, acceptable post-implant dosimetry was achieved.

Recorded differences in seed positions before and after implant appear to be related to both intra-patient systematic uncertainties and random placement errors. Systematic displacements may be related to necessary adjustments made during the implant procedure based on US guidance. The relationship between seed placement and imaging in treatment planning are are explored in the following 2 chapters.

Chapter 5

Incorporating 3D Ultrasound Into Permanent Breast Seed Implant Treatment Planning

The results from Chapter 4 indicated that systematic displacements occur that are unique to each individual implant. These results are potentially related to setup adjustments that are made during the implant since differences from the planned setup position would result in global displacements of all implanted seeds. Treatment setup is based on the visualization of the seroma in the OR, and therefore differences between the planning CT and US guidance can potentially result in these displacements. This study assesses the potential impact of such visualization differences and assess the feasibility of incorporating 3DUS into the treatment planning procedure to reduce such uncertainties. Using spatially registered CT and US images, the impact of standard planning methods on US-defined target volumes is quantified, as well as the potential impact of intra-operative adjustments by shifting the plan to centre on the seroma visualized on US. Implementation of 3DUS into the planning procedure to compensate for uncertainties in the visualization and the potential effects on the treatment margins are explored. The presented study has been adapted from the publication of this work by the dissertation's author in *Brachytherapy* (doi:10.1016/j.brachy.2016.09.007) [96].

5.1 Introduction

As discussed previously, the widespread implementation of PBSI may only be realized through continued technique developments, resulting in a more standardized and transferable procedure. The results from Chapter 4 have indicated that uncertainties in the procedure exist which can potentially inhibit the accuracy of the delivery. These uncertainties may be related to deficiencies in the current PBSI methods. It is important to address the unique technical challenges of PBSI to enable this technique to be widely adopted with confidence. One challenge in PBSI is the use of two different imaging modalities within the treatment process: CT for treatment planning and freehand 2D US for implant guidance [10, 32]. The target in treatment planning is the post-lumpectomy seroma defined on CT, which is the clinical standard for partial breast irradiation [5, 10, 62, 97, 98]. Seroma visualization also aids in the implant procedure, where US imaging provides intraoperative guidance to ensure that the plan is correctly positioned on the seroma. Inherent differences in the visualization of the seroma on US and CT can result in variability in the size and shape when observed on the two modalities, potentially resulting in deviation of their centroid positions within the breast [36, 73, 86, 99]. Therefore, using these different modalities for planning and delivery means the CT-based treatment plan may not translate directly to the OR under US guidance without intraoperative adjustments [32]. Any such repositioning of the implant relative to the seroma visualized under US guidance could affect the dosimetry to the original target, planned on CT. Integrating 3DUS into the planning process alongside CT may help to address this challenge by using the same imaging modality for planning and intra-operative guidance.

3DUS has been shown to be a potentially useful addition to CT-based planning in external beam partial breast radiation therapy, in part because of improved seroma visibility and high inter-user consistency of contouring on US compared with CT [36]. However, its application and potential impact in PBSI treatment planning is currently unknown. Through retrospective analysis of coregistered CT and 3DUS images, the potential dosimetric effects resulting from planning and delivery using different imaging modalities, because of the differences in seroma visualization between CT and US, are evaluated. In addition, this study assesses the impact that the addition of 3DUS into PBSI treatment planning may have on the resulting treatment plans.

5.2 Methods

5.2.1 Registered CT and US Images

Patient images and contours acquired by Berrang *et al.* [36] to assess the role of 3DUS in treatment planning for partial breast EBRT were re-examined for this study, with approval from the University of British Columbia Research Ethics Board. In this previous study, for 20 consecutive early breast cancer patients, 3DUS imaging was also performed at the time of CT, with identical patient positioning, using the Clarity (Resonant Medical) ultrasound system described in Section 3.2.1. The tracked system acquires US images in a shared coordinate system as the CT scan, allowing for implicit registration of the images when acquired in the same patient positioning. Minimal compression was used during US image acquisition to reduce breast deformation, and registration of the image sets was validated by assessing the alignment of the skin and chest wall in this previous study [36].

The CT and US seroma contours used in this study were consensus volumes defined by Berrang *et al.* [36]. In the previous study, seroma contouring on the US and CT images was performed independently by three radiation oncologists, blinded to the corresponding image set, using standard clinical guidelines [36, 62]. Consensus seromas were defined for each modality using the methods described in Section 3.2.3. The three contours were overlayed and the middle contour was traced in order to produce a volume representing an average delineated seroma. Based on the size and location within the breast of the consensus seroma defined on CT, 10 patients (6 right and 4 left breast) were selected for this study. All eligible seromas had volumes smaller than 30 cc and were less than 3 cm wide orthogonal to the needle insertion direction to conform to PBSI criteria.

5.2.2 Contour and Treatment Plan Evaluation

The CT and 3DUS image sets complete with consensus contours were imported into MIM Symphony for PBSI planning on CT. 3DUS contours were transferred to the CT images using the implicit ridged registration between the image sets, as shown in Figure 5.1. The consensus seromas contoured on CT and US were used to define clinical target volumes CTV_{CT} and CTV_{US}, respectively. The CTVs were expanded by 1.25 cm and cropped at the chest wall contoured on the CT and 5 mm from the skin surface to create planning target volumes PTV_{CT} and PTV_{US}. PBSI treatment

plans were generated following the standard planning procedure outline in Section 2.4.2. Treatment plans were created based on the CT volumes alone, as is standard for clinical practice, using ^{103}Pd seeds with 2.5 U activity and a 90 Gy prescription dose. Planning goals included CTV_{CT} V_{100} of 100% and PTV_{CT} V_{100} of greater than 95%, limiting PTV coverage to $V_{150} < 70\%$ and $V_{200} < 25\%$, and dose over a 1 cm^2 area of the skin margin to $< 90\%$ of the prescription [9, 63].

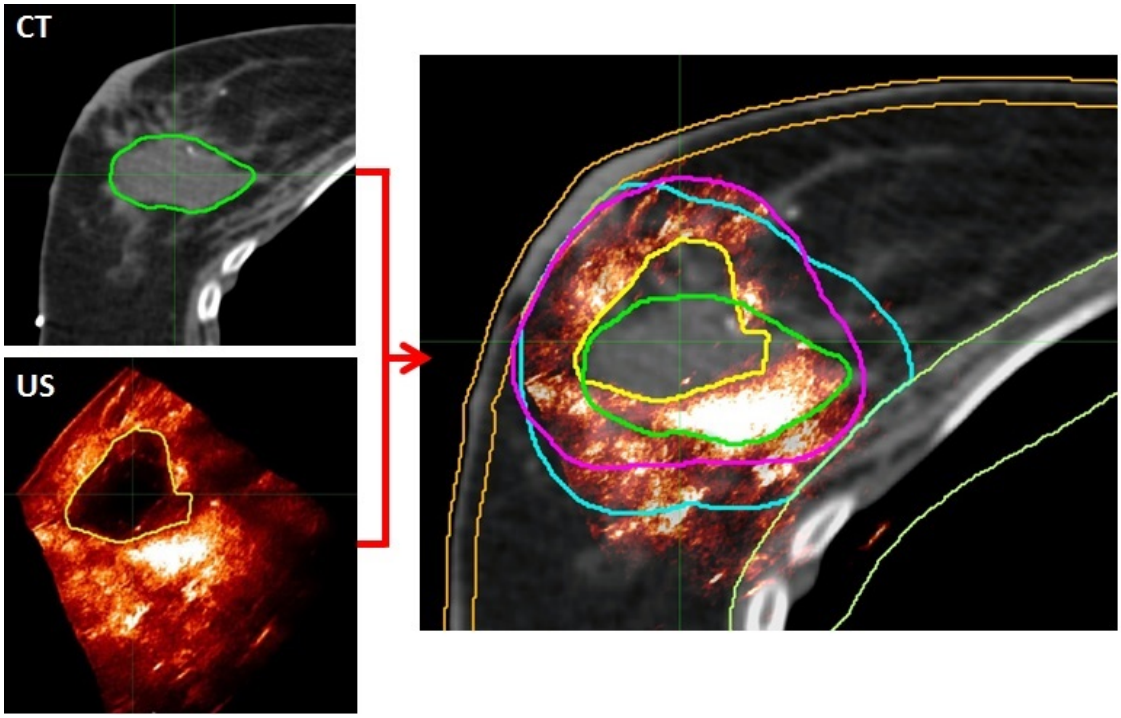

Figure 5.1: Fusion of CT and spatially registered 3DUS images. Consensus contours CTV_{CT} (green) and CTV_{US} (yellow) are expanded by 1.25 cm to create PTV_{CT} (blue) and PTV_{US} (pink), respectively, cropped to the chest wall and 5 mm from the skin surface.

After plan creation and optimization, the plan was re-evaluated using the 3DUS contours, which were transferred to the CT images. DVHs were computed for the US-defined contours CTV_{US} and PTV_{US}, and the coverage of these structures was evaluated to determine how CT-based planning, the standard PBSI procedure, provides coverage to volumes defined on US. In addition, correlations between the observed differences in the size and position of the CT and US contours and the dose differences between PTV_{CT} and PTV_{US} were evaluated.

The conformity index (CI), calculated as described in Section 3.2.3, was used to quantify the agreement of the CT and US contours. Disparity in the CTV and PTV

positions was also examined by calculating the differences in the centroid (center of mass) positions. The mean centroid difference between imaging modalities was calculated as well as the mean directional differences to identify any systematic offsets in seroma visualization that may exist.

5.2.3 Simulation of US Guided Procedure

After CT-based treatment planning, the PBSI implant procedure uses freehand 2DUS to guide needle insertion in the OR, as described in Section 2.4.2 [8–10]. The planned fiducial entry position is initially marked on the patient's skin based on the treatment plan using measured distances from external landmarks [10, 32]. During the implantation procedure, adjustments may be made to the entry point position to center the fiducial needle in the seroma as visualized on 2DUS. To simulate this practice, treatment plans were shifted by the calculated distance between CTV_{CT} and CTV_{US} centroids to mimic any manual adjustment of the fiducial needle entry point based on US guidance. The resulting mean relative change in coverage of CTV_{CT}, CTV_{US}, PTV_{CT}, and PTV_{US} was evaluated to assess the potential influence of visualization-based adjustments made in the OR on the planned dosimetry.

5.2.4 US Assisted Planning

One means to ensure adequate coverage of targets observed on both US and CT would be to plan using a PTV defined by considering both imaging modalities. This was tested by regenerating plans for each image set where the total volume encompassed by the CT and US CTVs was contoured and defined as CTV_{CT+US}, as shown in Figure 5.2. CTV_{CT+US} was expanded by a 1.25 cm margin to create a planning volume PTV_{CT+US}, cropped at the chest wall and skin margins as mentioned previously. The relative increase in volume from the original PTV_{CT} was calculated. Treatment plans were created using the same PBSI planning procedure as the CT-based plans but optimized to cover PTV_{CT+US} rather than PTV_{CT} alone. Coverage of the modality specific PTVs, PTV_{CT} and PTV_{US}, was also evaluated with the new plan. The mean relative increase in the number of additional seeds and needles required to treat PTV_{CT+US} compared to PTV_{CT} alone was calculated.

The effects of planning using PTV_{CT+US} on normal tissue dosimetry compared to PTV_{CT} alone were also examined. The planned skin dose was determined by calculating the $\text{D}_{0.2cc}$ to a 2 mm thick internal skin layer [63] for both PTV_{CT} and

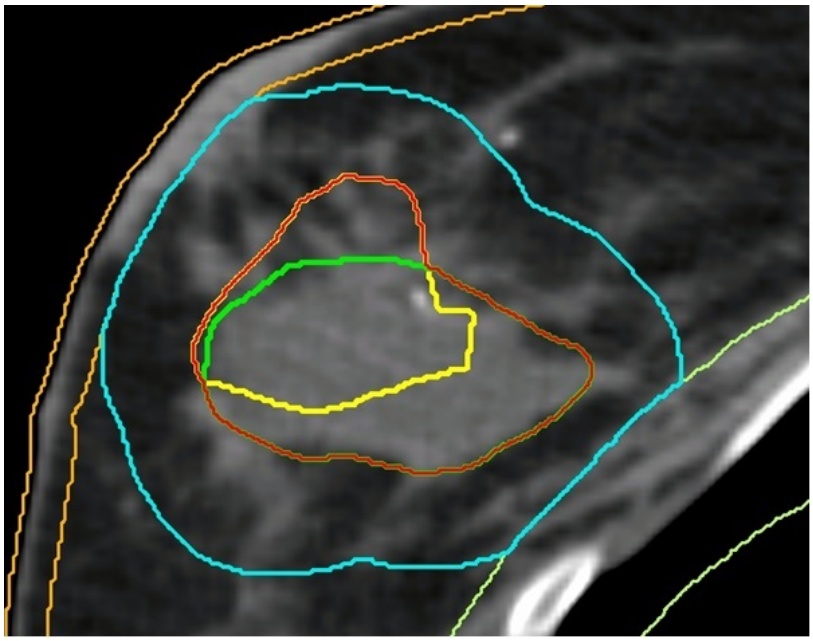

Figure 5.2: The total volume encompassed by CTV_{CT} (green) and CTV_{US} (yellow) is used to define CTV_{CT+US} (red) and resulting PTV_{CT+US} (blue).

PTV_{CT+US} based plans, and the mean relative difference was assessed. In addition, the differences in V_{100} and V_{200} within the breast were measured.

5.3 Results

5.3.1 Comparison of CT and US Contours

The volumes and positional differences for the evaluated CTVs are given in Table 5.1 The median (range) volumes of CTV_{CT} and CTV_{US} were 23.0 cc (7.9-38.4) and 20.8 cc (5.3-27.8), respectively. A strong positive correlation between volumes of the CT and US CTVs was observed ($r = 0.84$, $p = 0.003$). In nine of the 10 cases, CTV_{CT} was larger than CTV_{US}; median volume difference was 29.8% (4.5-69.9%). One was 5.5% smaller.

The CTV_{CT} and CTV_{US} generally exhibited low conformity, with a median CI of 0.51 (0.32-0.65) and difference (mean $\pm$ SD) in centroid position of 7 $\pm$ 3 mm. Mean directional difference was 5 $\pm$ 3 mm in the inferior direction and 1 $\pm$ 3 mm in the medial and anterior directions. The centroids of all CTVs were contained within the CTV of the other modality. No correlation was observed between the centroid shift

and the difference in the volumes of the CTVs ($r = 0.01$, $p = 0.99$).

Table 5.1: Volumes (SD) and positional differences of 10 consensus seromas evaluated using US and CT. Centroid shifts represents the distance of the US seroma centroid from the CT seroma centroid in standard ML AP SI coordinates.

	Volume (cc)		Centroid Shift (mm)			
Patient	CTV_{US}	CTV_{CT}	ML	AP	SI	Total
1	22 (1)	23 (7)	5.2	-2.8	-3.9	7.1
2	23 (6)	38 (5)	-4.2	-4.9	-8.5	10.6
3	21 (4)	23 (11)	2.8	-3.7	-10.2	11.2
4	16 (8)	22 (6)	2.5	-0.5	-4.7	5.3
5	21 (1)	26 (1)	-1.0	-1.1	-2.9	3.3
6	5 (2)	8 (2)	2.8	4.6	-2.6	5.9
7	28 (6)	31 (4)	-0.9	1.9	-4.7	5.1
8	17 (9)	16 (5)	-1.7	2.1	-6.0	6.5
9	25 (5)	32 (3)	5.7	-2.1	-3.8	7.2
10	13 (2)	21 (3)	1.1	-0.6	-3.3	7.2
Mean	19.0	24.0	1.2	-0.7	-5.1	6.6
SD	6.5	8.5	3.2	2.9	3.5	2.6

Table 5.2: Volume and conformity indices of PTVs based on the seromas on US and CT.

	Volume (cc)		
Patient	PTV_{US}	PTV_{CT}	CI
1	95.8	99.2	0.76
2	141.0	177.7	0.58
3	113.8	115.0	0.63
4	103.0	120.6	0.75
5	86.2	93.8	0.82
6	58.7	72.7	0.67
7	146.1	153.3	0.74
8	85.4	97.2	0.69
9	106.5	132.2	0.67
10	75.0	97.5	0.75
Mean	115.4	101.4	0.71
SD	31.3	27.4	0.07

As shown in Table 5.2, CT and US PTVs were observed to have substantially improved conformity than the respective CTVs with a median CI of 0.72 (0.58-0.82). Correlation between the volumes of the PTVs was also higher than the CTVs ($r =$

0.93, $p < 0.001$). All PTV_{CT} were larger than PTV_{US}, but the relative volume difference was much smaller than the differences in CTV size, 15.5% (0.7-30.0%), in part because of the cropping of the PTVs. The mean difference in centroid position between the PTVs was also 7 ± 3 mm, and the directional differences were equal to those observed in the CTVs.

5.3.2 PBSI Plan Dosimetry

Although plans were generated to cover CTV_{CT} with V_{100} of 100%, the CT-based planning also, in general, resulted in good coverage of the CTV_{US}: median V_{100} of 100% (97.0-100%). As shown in Figure 5.3a, the planned PTV_{CT} V_{100} was 95.6% (93.3-97.3%), and the resulting PTV_{US} coverage from these plans was 91.5% (80.5-97.9%). The mean relative difference in V_{100} between PTV_{US} and PTV_{CT} was -5 ± 6%, resulting in planned coverage of PTV_{US} being less than optimal (V_{100} <95%) in 7 of 10 plans.

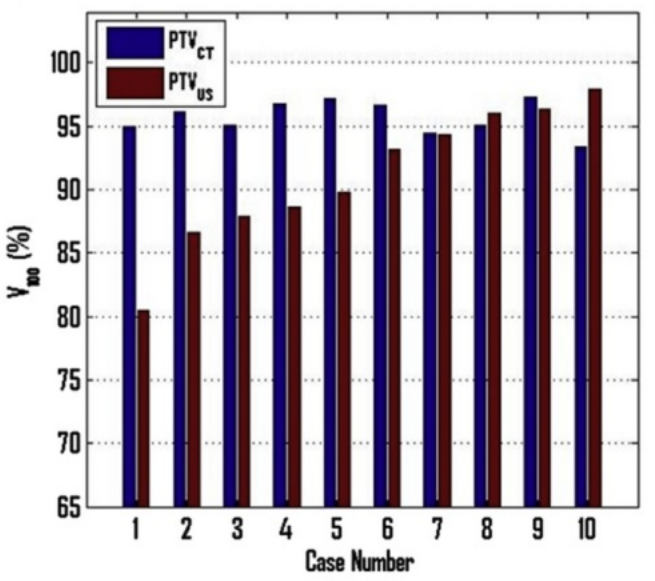

Figure 5.3: CT-based V_{100} plan coverage to PTV_{CT} and PTV_{US} volumes.

Figure 5.4a shows how differences in visualization of the seroma can lead to a portion of the PTV_{US} being under-dosed. Only weak correlations between the PTV V_{100} relative dose difference and CTV or PTV volume differences were observed. However, strong correlations were seen between the dose difference and the difference in centroid position of the CTVs ($r = 0.75$, $p = 0.01$) and PTVs ($r = 0.77$, $p = 0.01$),

highlighting how a difference in the volumes' positions impacts the coverage to the different targets and can leave regions under-dosed in treatment planning.

5.3.3 Simulation of US Guided Procedure

Shifting the CT-based treatment plans to be centered on CTV_{US} reduced the CTV_{CT} V_{100} coverage in three cases (0.4%, 0.9%, and 8.3%) and maintained 100% coverage in the others. Conversely, CTV_{US} V_{100} was increased in all cases where 100% coverage was not already achieved. In one case, CTV_{US} V_{100} decreased from 100% to 92.4%, where a large portion of the contour extended toward the lumpectomy scar away from the centroid of the seroma. Thus, CTV_{US} coverage was 100% in 8 of 10 plans (99.6% in the other).

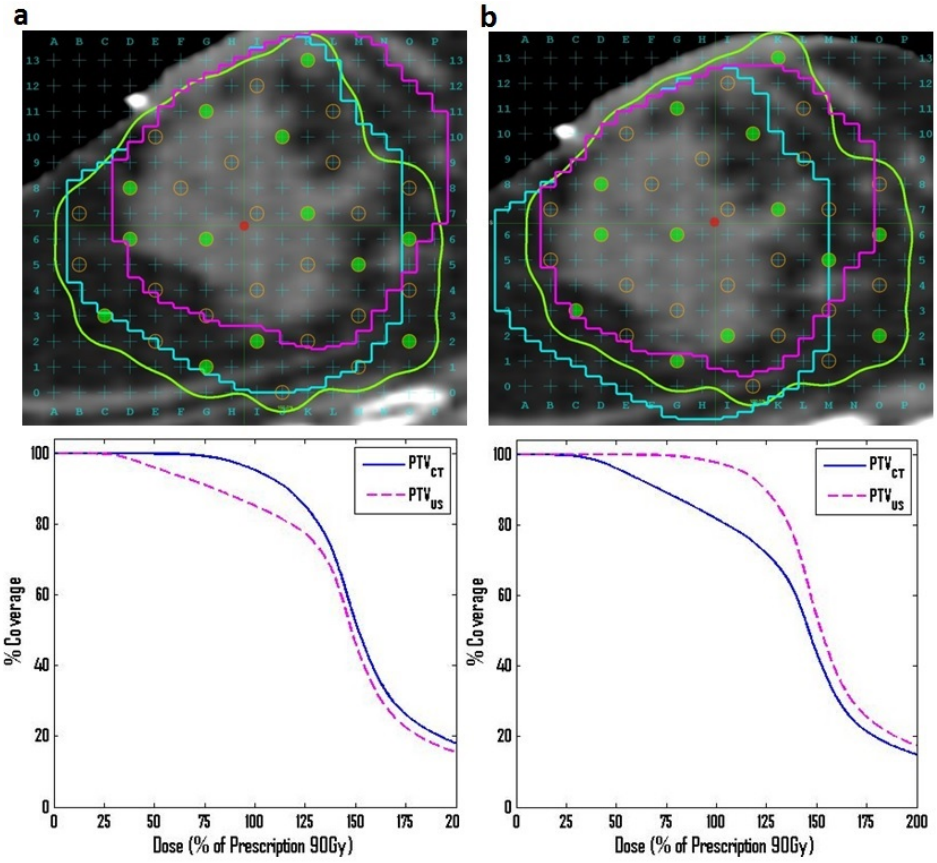

Figure 5.4: (a) The isodose line representing the volume to receive 100% of the prescription 90 Gy dose (green) planned and CT results in acceptable dosimetry to PTV_{CT} (blue) but under-doses PTV_{US} (pink). (b) Shifting the plan to center on the US seroma results in increased (and acceptable) coverage to the PTV_{US}, whereas resulting in an unacceptable decrease in the dose received by PTV_{CT}.

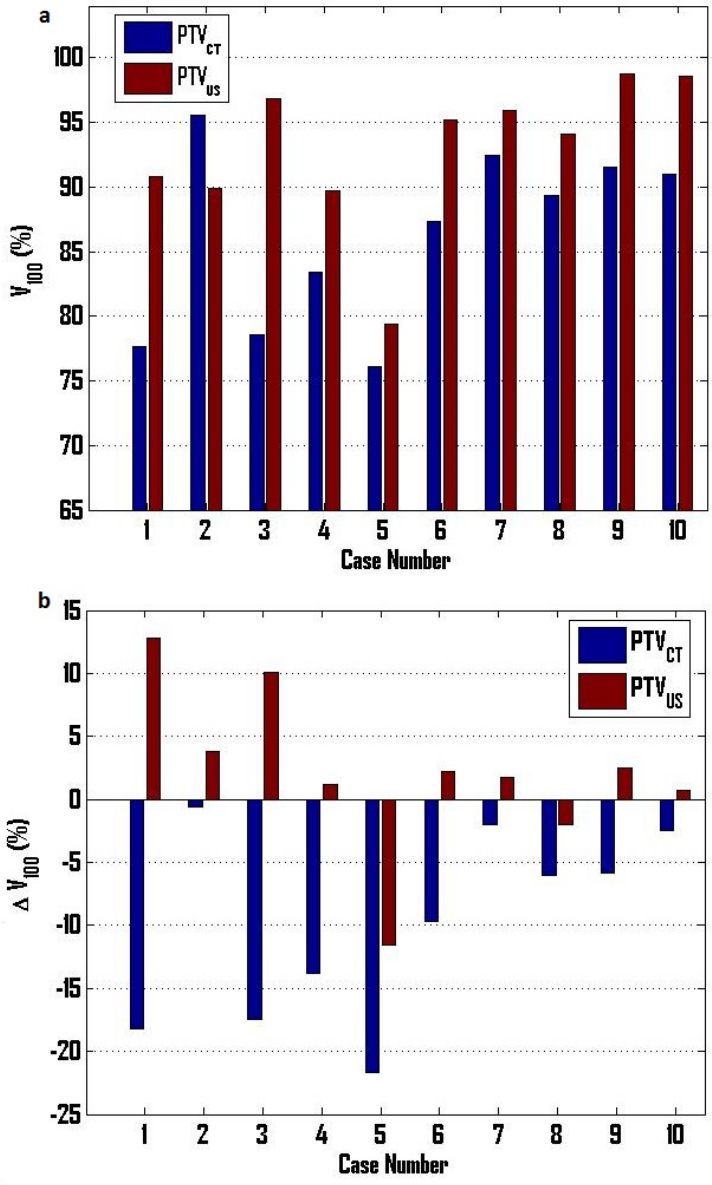

Figure 5.5: (a) Resulting PTV_{CT} and PTV_{US} coverage after shifting the plan to center of CTV_{US} and (b) the change to the coverage from the original plan

Figure 5.4b shows an example of how centering the CT-based plan to the CTV_{US} can result in decreased coverage to PTV_{CT} while increasing coverage to PTV_{US}. Figure 5.5a shows the PTV coverage following the treatment plan shifts. Such plan shifts resulted in decreased PTV_{CT} coverage in all the patients, with a mean relative decrease in V_{100} of -10 $\pm$ 8%, as shown in Figure 5.5b. However, V_{100} coverage to PTV_{US} increased in 8 of 10 patients (mean 5 $\pm$ 4%), with a 2.0% and 11.6% relative decrease in the others. After the shift, only one plan had optimal PTV_{CT} coverage

(median 88.3%; range 76.1-95.5%), and 6 of 10 plans had optimal PTV_{US} coverage (median 94.7%; range 79.4-98.8%), as shown in Figure 5.5a. The mean difference in $D_{0.2cc}$ to the 2 mm skin layer from the original to the shifted plan was 3 ± 45%; thus, no systematic effect on skin dose was observed.

5.3.4 Assessment of 3DUS Assisted Planning

Planning the treatment using a PTV that encompasses the volume of both PTV_{CT} and PTV_{US} resulted in a mean 9 ± 6% increase in the volume of the PTV (Table 5.3) and required a mean 7 ± 8% more seeds and 5 ± 5% more needles (average of an additional 10 seeds and 2 needles). PTV_{CT+US} V_{100} was 95.5% (93.3-96.3%) and PTV_{CT} and PTV_{US} coverage was 95.9% (93.3-97.3%) and 97.0% (94.7-98.5%), respectively. Achieving acceptable dosimetry in PTV_{CT+US} therefore resulted in adequate coverage to the individual PTV_{CT} and PTV_{US} volumes.

Table 5.3: The increase in the volume of the PTV (ΔPTV) when planning on PTV_{CT+US} relative to PTV_{CT} alone, and the resulting increase to the skin dose ($\Delta D_{0.2cc}$) and the total breast volume receiving 100% and 200% of the prescription dose (ΔV_{100} and ΔV_{200})

Patient	ΔPTV (%)	$\Delta D_{0.2cc}$ (%)	ΔV_{100} (%)	ΔV_{200} (%)
1	13.3	22.9	10.1	9.5
2	13.1	0.9	12.1	7.6
3	21.7	31.4	19.6	14.7
4	5.9	8.2	-3.4	-4.8
5	5.6	2.9	14.1	6.3
6	8.1	-22.1	-1.2	4.9
7	12.1	67.5	15.0	18.9
8	0.6	5.3	-5.1	-3.0
9	12.1	-1.8	8.8	8.7
10	1.0	-0.2	-0.3	-0.7
Mean	9.3	11.5	7.0	6.2
SD	6.4	24.4	8.8	7.5

Expansion of the PTV resulted in additional dose to normal tissues. The median $D_{0.2cc}$ to the 2 mm thick skin layer was 91.0% (57.1 - 108.3%) of the prescription dose. The plans based on PTV_{CT} alone had median skin dose of 79.8% (54.0-99.6%), representing a mean 11 ± 24% relative increase in the skin dose when planning on PTV_{CT+US}, shown in Table 5.3. The V_{100} and V_{200} within the breast also increased

by a mean 10 ± 12 cc and 2 ± 3 cc, respectively (mean relative increases of 7 ± 9% and 6 ± 8%).

5.4 Discussion

PBSI treatment planning is based on CT imaging because current clinical standards define the target for partial breast irradiation as the post-lumpectomy seroma delineated on CT, and CT provides a fixed coordinate system for treatment planning [5, 10, 62, 97, 98]. Imaging the patient in the external beam treatment position, on an angled breast board, with the ipsilateral arm supported in an abducted and extended position allows for a treatment plan to be created with an optimal needle insertion angle and fiducial needle entry point that can be reproduced when the patient is in the OR. However, once the patient is positioned in the OR, the seroma is visualized with US and, if necessary, the plan will be shifted slightly to provide accurate positioning with respect to the US-visualized seroma, while maintaining the same angle of entry [32]. These adjustments potentially create the patient-specific seed displacements during the treatment delivery which were observed in the previous Chapter [60]. This study suggests that part of the reason this shift may be required is in fact because of the different appreciation of the seroma on CT and US. Because the CT-defined seroma is the clinical target, the plan cannot confidently be adjusted to the seroma observed on US. However, the seroma that is observed in the OR cannot be ignored if discrepancies from the plan exist. The dosimetric variations that arise from seroma visualization and the potential impact of transferring the CT-based plan to an US-guided procedure were investigated in this study. Several studies have assessed the use of US to assist in seroma identification for external beam partial breast irradiation and generally conclude US imaging to be a useful addition to the planning procedure [36, 73, 86, 99–101]. To improve the efficacy of the PBSI treatment, 3DUS can be implemented into the planning procedure to aid in identifying the seroma on US before entering the OR and can be used to adjust the plan to target areas of uncertainty resulting from seroma visualization.

CTVs visualized using CT and US were observed to have overall low conformity. Differences in contour positions result in low conformity, but even cases with small centroid differences lacked conformity because of the large volume differences and thus small overlapping volumes. Despite the observed low CTV conformity, previous work has shown that an average of 72% of the CTV_{US} is contained within CTV_{CT}

[36] and is therefore located within the clinically relevant planning regions. The inter-modality CI is limited by the accuracy of the image registration, which was previously validated to be within 2 mm for all cases included in this study [36].

PTV contours did not suffer from the same lack of conformity, where the CI of these contours was 0.73 (0.58-0.82) and a mean 49% higher than the CTV CI. Improved conformity and smaller relative volume difference of the PTVs are expected as cropping of the contours at the chest wall and skin eliminates the differences between the two modalities in these regions. CT-based plans were therefore still able to provide V_{100} coverage greater than 95% to PTV_{US} in 3 of 10 cases but were suboptimal in the others.

Systematic differences in seed placement relative to their planned positions within individual patients were demonstrated in Chapter 4, implying that intra-patient offsets occur in the delivery [60]. Despite under-dosing PTV_{US} in treatment planning, it is likely that the visualization of the seroma using US during the implant results in the setup being shifted to the center of CTV_{US} rather than CTV_{CT} during implant. Simulating this plan shift, as shown in Section 5.3.3, maintained acceptable coverage in both CTVs in most cases. As expected, small decreases to CTV_{CT} were observed as the plan was shifted away, resulting in small increases to the CTV_{US} dose. In one case, the original treatment plan conformed to the changes in the skin contour near the lumpectomy scar. When the plan was shifted to centre on CTV_{US}, away from the skin, a portion which extended towards the scar was left outside of the 100% isodose region. Changes to PTV coverage were much greater than the CTVs, coverage of PTV_{CT} was reduced in all cases by a mean $10 \pm 8\%$. Conversely, the shift resulted in an increased PTV_{US} coverage in 8 of 10 implants.

To ensure adequate dose to the target volumes defined by both US and CT, this study showed that the total encompassing volume of PTV_{CT+US} could be treated to achieve acceptable coverage in both PTV_{CT} and PTV_{US}. Creating a plan on the increased volume only required one to two additional needles and an average of 10 more seeds, a small increase relative to the mean 26 needles and 119 seeds used in the CT-based plans. The mean 9% increase in volume from PTV_{CT} to PTV_{CT+US} resulted in 5 of 10 plans over the 120 cc PTV limit [10]. However, volumes used for planning in this study were generally much larger than those observed in actual PBSI treatments (mean 115 cc vs. approximately 60 cc [9, 35]), and therefore similar relative volume increases would not be concerning for average PBSI PTVs. The mean 6% (2 cc) increase in V_{200} is small relative to the 20-30% PTV V_{200} planning target,

but skin dose increased by a mean 11% resulting in 6 of 10 plans exceeding the target 90% of the prescription to a 1 cm^2 area [63]. The increase was a direct result of a greater surface area of PTV adjacent to skin for the expanded volume, PTV_{CT+US}. Planning the treatment on the combined volumes, although feasible, represents an upper limit of how dosimetry may change when implementing 3DUS into the planning procedure. Although this method has shown to be acceptable in this retrospective planning study, more extensive analysis into the appropriate application of 3DUS in PBSI planning is required.

Partial breast irradiation aims to reduce the irradiated breast volume, relative to whole breast irradiation, by treating only the lumpectomy cavity and adjacent margins where the risk of recurrence is greatest [27, 61, 102–104]. The margins used to define the PTV beyond the seroma visualized on CT for APBI range from 0 to 3 cm in various studies and techniques, with a general consensus within the 1-2 cm range [7, 10, 27, 51, 103–105]. The PTVs in this study were defined as a 1.25 cm expansion of the seroma contour. Increasing the margins to 1.5 and 2 cm would result in mean $9 \pm 6\%$ and $47 \pm 14\%$ larger PTVs than PTV_{CT+US}, respectively, and thus PTV_{CT+US} is not unacceptably large compared with clinically accepted margins.

PBSI stands to benefit from improved 3DUS procedures for both treatment planning and image-guided delivery, but such integrated US tools for breast are not yet widely available. Although this study has shown that the differences in seroma visualization can result in intra-operative shifts of the treatment plan, with potential dosimetric effects, the true impact of the differences between the two modalities on seed placement accuracy in the PBSI procedure has not been determined. A prospective evaluation of CT and US seroma visualization and the relationship to seed placement accuracy in PBSI patients may highlight specific factors in treatment planning which predict for inaccuracies in the delivery and is examined further in the following chapter.

5.5 Conclusion

Inherent differences in the visualization of the seroma on CT and US have dosimetric effects in the PBSI procedure. Planning PBSI treatments using CT alone to define target volumes can result in under-dosage of the target volumes observed on US. In addition, a positional difference of the seroma centers between the two modalities, resulting from the visualization, reduces coverage to the CT-defined targets when

adapting the plan to an US guided procedure. Implementing 3DUS into the planning procedure can potentially be used to compensate for the differences in seroma delineation.

Chapter 6

Identifying Impact of Seroma Delineation on Seed Placement Accuracy

The previous two chapters have quantified the seed placement accuracy in PBSI and evaluated the potential impact of visualization differences between CT and US in treatment planning. The intra-patient systematic displacements observed during this analysis may be related in part to such visualization differences. This chapter prospectively evaluates the impact of seroma delineation on seed placement accuracy to quantify the effects of visualization on the PBSI procedure. At the time of the planning CT scan for prospective PBSI patients, 3DUS images were acquired. The seromas on CT and US were delineated by multiple users to quantify the visualization and differences between the two modalities and the relationships between these metrics and the seed placement accuracy is evaluated.

6.1 Introduction

Accurate seroma delineation for APBI treatment planning is critical to accurate target definition and, thus, successful treatment [6, 98, 106]. PBSI brachytherapy delivery accuracy may be particularly sensitive to seroma delineation uncertainties as it is pre-planned using CT imaging [5, 10, 97, 98] and uses ultrasound (US) for implant guidance [10, 32]. Variability in seroma delineation in APBI treatment planning on CT has been observed and shown to be associated with clarity of seroma visualization

[62, 76, 77, 105, 107]. Additionally, it is well established that seromas observed on CT vary in size and shape from those observed on US as demonstrated in Chapter 5 [36, 73, 86, 96, 99]. Both effects may influence PBSI delivery accuracy by requiring unplanned intra-operative adjustments to adequately treat the target as observed during the treatment.

The study presented in Chapter 5 showed that inter-modality differences in seroma definition leads to different target centroid positions [96]. As PBSI seed distributions are centered on a fiducial needle inserted at or near the target centroid, it is hypothesized that these inter-modality differences may contribute to the observed seed placement uncertainties in PBSI, demonstrated in Chapter 4 [60]. This study prospectively evaluates the relationship of seed placement accuracy in PBSI with both the differences in target definition between the two modalities and seroma delineation variability. By identifying factors related to seroma delineation which may predict for seed placement uncertainties, the accuracy and confidence in the procedure may be increased.

6.2 Methods

6.2.1 Patient Selection

Early-stage breast cancer patients are considered for PBSI after meeting the established eligibility criteria described in Section 2.4.1. The patients in this study were greater than 60 years of age with low risk Stage 0 or 1 breast cancer, clear margins and visible seroma less than 3 cm in diameter [9, 60, 63]. Ten patients who received PBSI at CCSI were included in this study (4 left, 6 right breast) to prospectively acquire and evaluate 3DUS images independently of the regular treatment procedure. Participation was approved by the University of British Columbia Research Ethics Board and patients provided informed consent to have 3DUS imaging performed at the time of their planning CT-simulation.

6.2.2 Image Acquisition

The Clarity US system used for image acquisition for the study presented in Chapter 5 was used here to acquire 3DUS images for PBSI patients. As discussed in Section 3.2.1, the infrared imaging system tracks the location of the US transducer as it

is swept freely across the breast such that, when acquired in the CT setup, the reconstructed 3DUS volumes share a coordinate system with the CT scanner and registration between CT and US images is implicit. The US system was calibrated daily prior to each imaging session and US localization was accurate to within 1 mm directionally, consistent with the system's expectations [75].

As for the standard clinical procedure, patients were positioned in CT on an angled breast board with the ipsilateral arm in an abducted and extended position, as for CT simulation. The seroma was initially assessed for visibility and suitability for implant using 2DUS to determine seroma size, depth, and approximate location. If deemed potentially eligible for PBSI, the CT scan was performed. The patient was instructed to remain still after the CT and the 3DUS scan was performed within 2 minutes to ensure identical positioning. US images were acquired by a skilled radiation oncologist using coupling gel and minimal breast compression to reduce deformation. Multiple scans were acquired in different sweeping directions to ensure acquisition of a high-quality image without loss of contact. The co-registered images were transferred to MIM Symphony. PBSI treatments were planned and delivered using the standard clinical procedure and equipment (Section 2.4.2), without the aid of the 3DUS images.

6.2.3 Seroma Assessment

Independently of treatment planning, seromas were contoured on the CT and US images by three radiation oncologists specialized in breast radiation therapy. The individual users were blinded to corresponding image sets and to other users' contours. Seroma contouring was performed using the standard clinical guidelines described in Section 3.2.3, defining the seroma by the evident dense region on CT and the dark anechoic region and surrounding hypoechoic wall on US [36, 62]. The treating oncologist repeated the contouring on CT twice more at different times, blinded to the previous contours, to quantify the intra-user variability and further assess the confidence in the defined clinical target. In all cases, consensus contours, CTV_{CT} and CTV_{US} were defined on CT and US, respectively (Figure 6.1), from the 3 individual contours by selecting the median contour as described in Section 3.2.3 [36, 96].

Intra-user, inter-user, and inter-modality variations in seroma delineation were quantified by their conformity indices, calculated using the methods described in Section 3.2.3. Intra-user CIs were assessed on CT alone, as US is not used in the

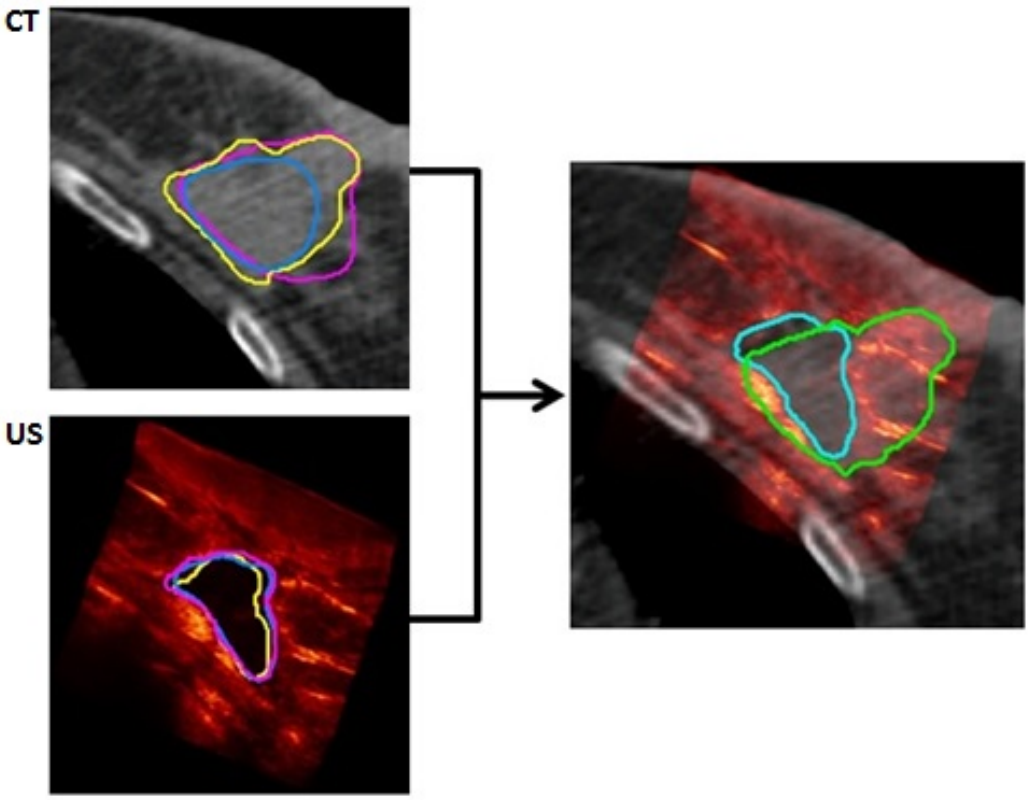

Figure 6.1: Seromas contoured by multiple users independently on CT and US (blue, purple, yellow) are used to create consensus volumes CTV_{CT} (cyan) and CTV_{US} (green), and fused using the implicit registration of the 3DUS system.

planning procedure, and the inter-user CI was calculated on both imaging modalities. Inter-modality differences were assessed by transferring CTV_{US} to the CT images using the implicit registration of the 3DUS system (Figure 6.1). The volumes, centroid positions, and CI of the consensus seromas were recorded and any differences between CTV_{CT} and CTV_{US} were evaluated. Additionally, the percent volume of CTV_{US} contained within CTV_{CT}, and vice versa, was assessed.

6.2.4 Relationship Between Seroma Delineation and Seed Placement

Following the implants and standard post-implant dosimetry verification, the day-0 CTs were analysed to evaluate the differences between the planned and implanted seed positions using the methods described in Section 3.1 [60]. The same registration procedure, using a 1 cm ROI around the planning and post-implant seromas, used

for the study in Chapter 4 was performed to align the image sets. The resulting transformation matrix was applied to the post-implant seed positions, which were then paired to their planned positions using the seed matching process (Section 3.1.2) to evaluate the seed displacements.

For each patient, several metrics of seed displacement were calculated: the mean total displacement, directional displacements, the systematic displacements, and the random displacements. The mean total displacement of all implanted seeds was determined to quantify overall seed placement accuracy for each implant. Directional displacements, assessed as the mean placement differences in the ML, AP, and SI directions imply intra-patient shifts in seed displacement, as described in Chapter 4. The norm of these directional shifts, and the resulting residual displacements approximated the systematic and random components of the seed placement accuracy, respectively (Section 3.1.3).

Associations between variability in seroma definition and seed placement accuracy were examined by assessing the correlations between the intra- and inter-user CIs and the total seed displacements. Differences in the centroid positions between CTV_{CT} and CTV_{US} were compared to the directional displacements. The impact of the agreement between the two imaging modalities on total seed placement accuracy was also assessed by the correlations with the inter-modality CI, and the volume difference of CTV_{CT} and CTV_{US}.

Analysis was repeated using the systematic displacements only to assess the relationship between seroma definition and the intra-patient systematic displacements in the delivery. Similarly, the effect of the seroma delineation on the random displacements was evaluated. Correlations between all metrics were analysed using Pearson correlation statistics to establish whether seroma delineation differences could predict for larger seed displacements.

6.3 Results

6.3.1 Seroma Delineation Analysis

The median (range) intra-user CI was 0.60 (0.46-0.72). Inter-user CI were 0.46 (0.38-0.58) and 0.50 (0.29-0.67) on CT and US, respectively, in accord with previously observed results using the Clarity system [36]. Seroma contours on US had higher inter-user CI than CT in 6 out of 10 cases (equal in 1), shown in Table 6.1. Similar

to those in Chapter 5, consensus seroma volumes varied widely between CT and US; median CTV_{CT} and CTV_{US} volumes were 7.2 cc (3.8-13.0 cc) and 2.7 cc (0.5-6.4 cc), respectively. CTV_{US} was smaller than CTV_{CT} in every case, with a mean (±SD) volume difference of 68 ± 12% ($p < 0.0001$). The delineation differences between the two modalities resulted in apparent positional differences, with a mean magnitude difference in centroid location of 8 ± 3 mm. Mean medial, anterior, and inferior directional differences in centroid position (CT to US) were 2 ± 5 mm, 2 ± 4 mm, and 4 ± 5 mm, respectively.

Table 6.1: The volumes (SD) of consensus contours and the inter-user CI on CT and US for the 10 cases in this study.

	CT		US	
Patient	Volume (cc)	CI	Volume (cc)	CI
1	13 (2)	0.58	6 (2)	0.54
2	6 (1)	0.43	2 (1)	0.48
3	4 (1)	0.48	1 (1)	0.29
4	7 (2)	0.45	2 (1)	0.45
5	7 (3)	0.39	2 (1)	0.49
6	12 (5)	0.38	3 (1)	0.50
7	11 (3)	0.53	3 (1)	0.52
8	6 (2)	0.44	1 (0)	0.49
9	10 (2)	0.56	5 (1)	0.59
10	8 (2)	0.49	3 (0)	0.67

Inter-modality CI, determined from CTV_{CT} and CTV_{US}, was only 0.14 (0.11 - 0.29). This low conformity was, however, due primarily to the large volume difference between the contours, as a mean of 67 ± 20% of CTV_{US} was contained within CTV_{CT}, opposed to a mean 20 ± 8% of CTV_{CT} contained within CTV_{US}. For example, Figure 6.2 shows CTV_{US} completely contained within CTV_{CT} with only 3 mm centroid difference, but the 85% volume difference results in a CI of only 0.14.

6.3.2 Seed Placement Accuracy

Seeds implanted for the entire 10 patient cohort (701 total) were placed a mean 10 ± 5 mm from their planned locations, with individual seeds placed between 0 and 31 mm, which is consistent with the results obtained in Chapter 4 [60]. As shown in Figure 6.3, mean directional displacements in the AP and SI directions were 1 ± 6 mm and 1 ± 4 mm, respectively. A small offset in the ML directional distribution is observed (mean

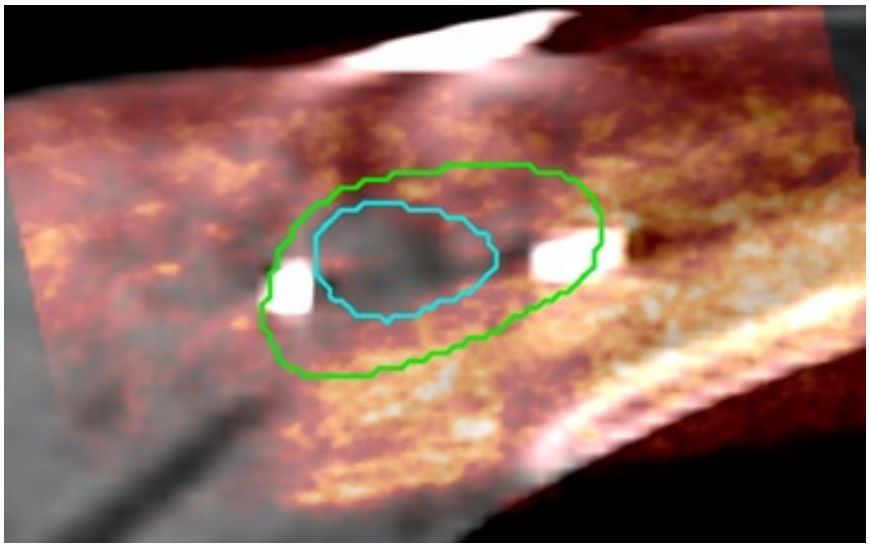

Figure 6.2: Image fusion shows low conformity between two imaging modalities that can result despite CTV_{US} (cyan) being entirely contained within CTV_{CT} (green).

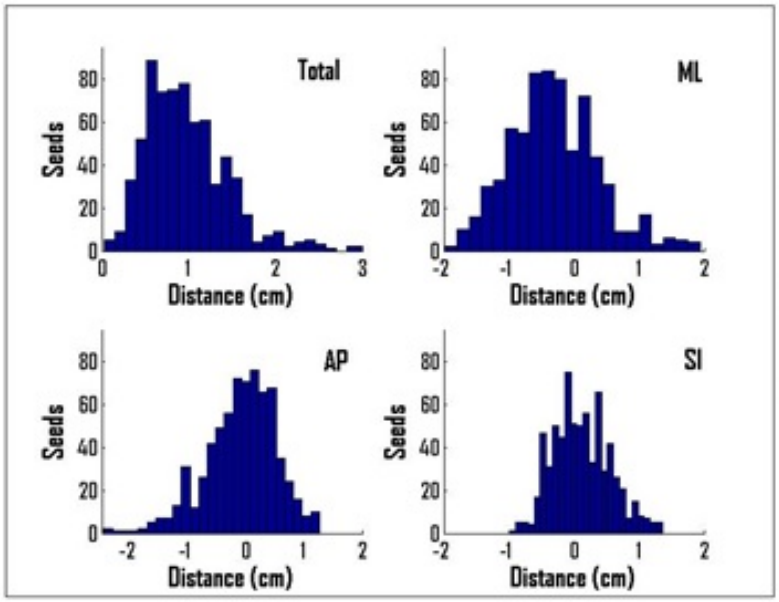

Figure 6.3: Histograms of the total and directional (ML, AP, SI) differences in the planned and implanted seed positions for all seeds in the 10 implants.

3 ± 7 mm), as seen by the large amount of seed displaced in the lateral direction. Individual implants' total seed displacements ranged from 7 ± 2 mm to 12 ± 6 mm. Intra-patient directional displacements were observed, implying global offsets in the delivery, and ranged from -9 to 3 mm in the ML and AP directions, and from -2 to 6 mm in the SI direction. Across all implants, mean systematic displacement was 6

± 3 mm, while mean random displacement was 7 ± 1 mm, as shown in Figure 6.4.

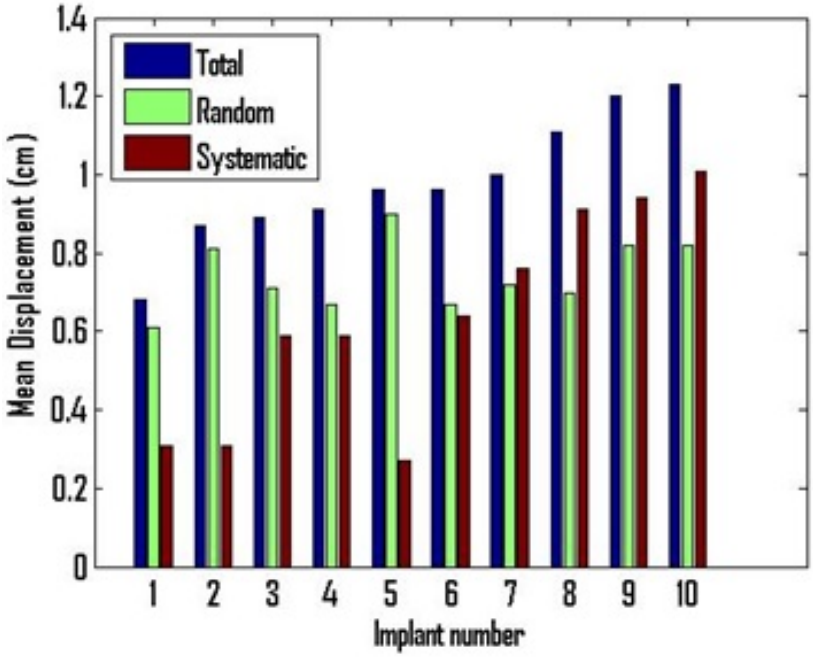

Figure 6.4: The total seed displacement for each implant and the corresponding random and systematic components of the displacements.

6.3.3 Correlations Between Delineation Differences and Seed Placement

No significant correlations between the intra-user CI and the total seed displacement was observed ($r = 0.11$, $p = 0.75$). Inter-user US CI also did not correlate with total seed displacement ($r = 0.25$, $p = 0.48$). However, as shown in Figure 6.6a, a strong correlation was observed between total seed displacement and the inter-user CI on CT ($r = 0.74$, $p = 0.01$).

Total seed displacements were not significantly correlated with the difference in centroid position of CTV_{CT} and CTV_{US} ($r = 0.46$, $p = 0.18$) (Figure 6.5a), and there was no observed association between directional seed displacements and directional differences in centroid position between the two modalities. Similarly, no correlation between the total seed displacement and inter-modality CI was observed ($r = 0.32$, $p = 0.36$), as shown in Figure 6.5b. Although low conformity of the consensus seromas did not associate with larger displacements, a moderate correlation was observed be-

Table 6.2: Correlation of seroma delineation metrics with the total, systematic, and random seed displacements. Significant correlations are highlighted in bold.

	Total		Systematic		Random	
	r	p	r	p	r	p
Intra-user CI (CT)	0.11	0.75	0.34	0.34	0.43	0.21
Inter-user CI (CT)	**0.74**	**0.01**	**0.67**	**0.03**	0.19	0.61
Inter-user CI (US)	0.25	0.48	0.51	0.13	0.38	0.28
CTV_{CT}-CTV_{US} Position (mm)	0.46	0.18	0.43	0.21	0.22	0.54
CTV_{CT}-CTV_{US} CI	0.32	0.36	0.33	0.35	0.06	0.87
CTV_{CT}-CTV_{US} Volume (%)	**0.65**	**0.04**	**0.64**	**0.05**	0.18	0.62

tween total seed displacement and the volume difference between CTV_{CT} and CTV_{US} ($r = 0.65$, $p = 0.04$), shown in Figure 6.6b.

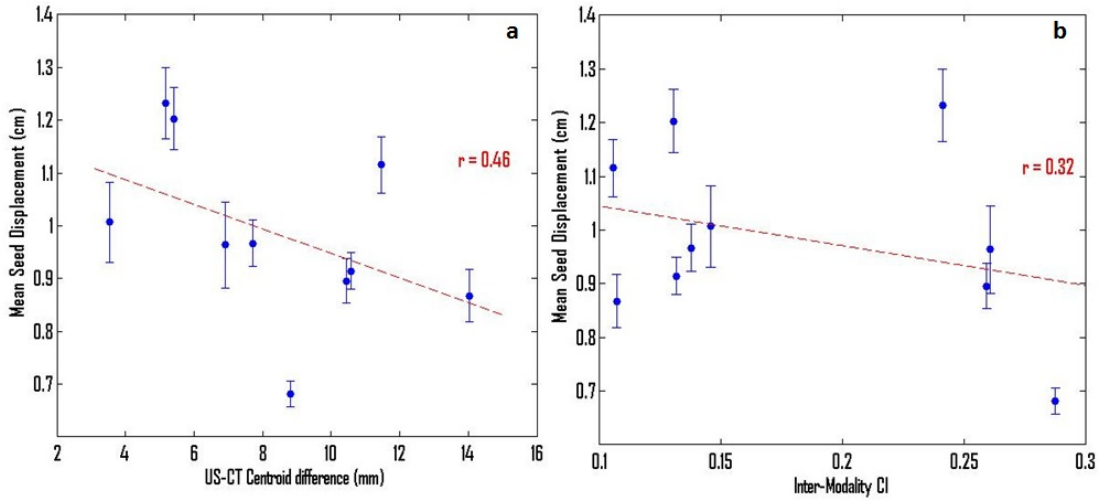

Figure 6.5: Relationship between the total seed displacement and (a) the difference in the centroid positions of CTV_{CT} and CTV_{US} and (b) the inter-modality CI.

Similar relationships between the seroma visualization uncertainties and the total seed displacements were also observed with the systematic components of the seed displacements. Intra-user CI on CT and inter-user CI on US, as well as the inter-modality CI and centroid differences were not observed to be significantly correlated with systematic component of the displacement, as shown in Table 6.2. However, systematic displacements were significantly correlated with the inter-user CT CI ($r = 0.67$, $p = 0.03$) and the volume difference between CTV_{CT} and CTV_{US} ($r = 0.64$, $p = 0.05$) (Figure 6.7). Conversely, there was no correlation between the random component of seed displacement and inter-user CI ($r = 0.19$, $p = 0.61$) or volume

difference ($r = 0.18$, $p = 0.62$).

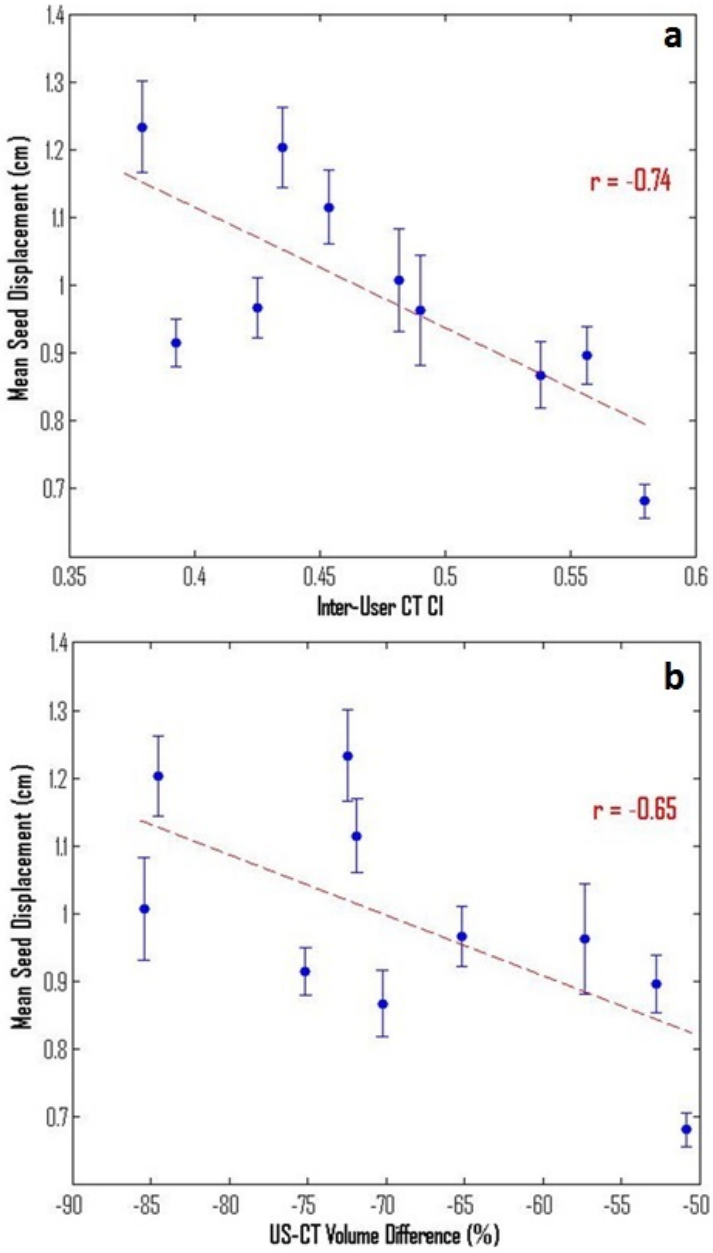

Figure 6.6: Relationship between the total seed displacement and (a) the inter-user CI of seromas contoured on CT and (b) the volume difference between CTV_{CT} and CTV_{US}.

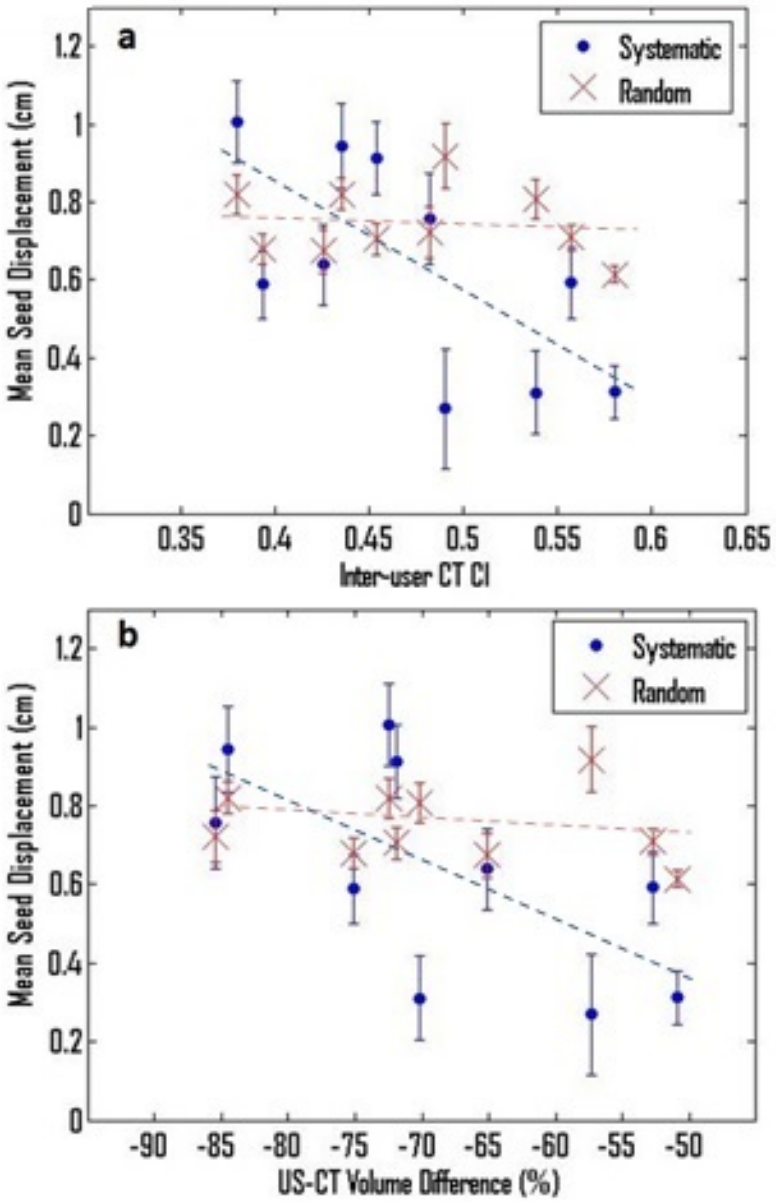

Figure 6.7: Relationship of the random and systematic components of the seed displacements with the (a) inter-user CI of the seromas contoured on CT and (b) the volume difference between CTV_{CT} and CTV_{US}.

6.4 Discussion

PBSI is subject to several unique technical factors which can make the procedure challenging and inhibit adoption and implementation of the technique. One such factor may be related to deficiencies in imaging. Subjective interpretations of the target, specifically the seroma in the breast, potentially increases user-dependence

of the procedure and can introduce uncertainties in the delivery. Like other APBI techniques, the success of the PBSI procedure relies on accurate delineation of the seroma [5, 97, 98]. Target volume delineation is performed on CT and during the delivery the seroma is visualized on US to guide the implant and to potentially adjust the needle positions based on the intra-operative visualization. While small physical changes in the seroma likely occur from planning to implant [61, 98, 108], additional factors leading to these adjustments may be uncertainties in seroma delineation in treatment planning and the inherent seroma visualization differences between CT and US. In the clinical experience at CSI, such adjustments are sometimes necessary to adequately treat the volume observed during the procedure. However, as shown in this study, uncertainties in seroma delineation itself may influence differences between the planned and implanted seed positions.

Variability in seroma contouring was observed between imaging modalities, multiple observes, and even within a single user. The inter-user variability in seroma contouring observed was consistent with similar visualization studies [36, 62, 76, 77, 105, 107]. This was despite the significantly smaller volumes used in PBSI than in other forms of APBI, with a median CTV_{CT} volume of 7.2 cc compared to, for example, 32 cc and 49 cc observed by Berrang *et al.* [36] and Petersen *et al* [76], respectively. However, the inter-modality (CT to US) conformity, 0.14 (0.11-0.29), was much smaller than observed for the volumes examined in Chapter 5 where inter-modality conformity was 0.51 (0.32-0.65) [96]. Given differences in centroid positioning were similar (7 mm) in the two studies, the lower inter-modality CI observed in this chapter can be attributed to the small PBSI volumes since contour discrepancies translate into larger relative volume differences and lower CI for smaller volumes.

The implants analysed in this study had total seed placement accuracy that was consistent with evaluations of independent cohorts, such as in Chapter 4 [60, 109]. Figure 6.3 shows no significant trends in the directional displacements across the cohort and Figures 6.4 and 6.7 show that the random displacements are consistent between implants. Thus, differences in the accuracy of seed placement observed between implants results primarily from the systematic component of the displacements.

The systematic seed displacements for each implant significantly correlated with the inter-user conformity of seroma contouring on CT (Figure 6.6a). Therefore, the precision with which the target can be defined in planning does appear to influence seed placement accuracy. Similarly, the volume difference between CTV_{US} and CTV_{CT} was significantly correlated with the systematic displacements. Although

these are not causative relationships, as the uncertainty in target definition and the differences between the seromas on CT and US increase, larger intra-operative adjustments may be required to treat the volume observed during implant, therefore increasing the magnitude of systematic seed displacements. In contrast, the inter-user CI of seromas defined on US did not correlate with the seed displacements, nor did intra-user conformity.

The results from Chapter 4 and 5 suggested that apparent positional difference of the seroma centroid observed on US and CT, resulting from inherent visualization differences [36, 73, 86, 99], could result in plan shifts during delivery, equivalent to the CTV_{CT}-CTV_{US} centroid differences [60, 96]. However, correlations between total and directional seed displacements and the inter-modality centroid position differences, in either magnitude or direction, were not observed in this study, indicating that the shift in centroid position between modalities does not capture all of the decision process in making intra-operative adjustments to PBSI plans.

In Chapter 4 it was demonstrated that total seed displacements of less than approximately 11 ± 4 mm were more likely to result in implants where target dosimetry goals (ETV V_{90} >90%) were met [60]. Similar results were observed in this study, with 8 of the 10 implants achieving the ETV coverage goal. Two of the 3 implants with displacements greater than 1.1 cm had ETV coverage of 86 and 71%. This study has also shown that low inter-user CI on CT is associated with increased total seed displacements and that all implants with total displacement above this threshold had inter-user CI of less than 0.45. It is well established that as both seroma clarity and seroma volume decrease, so dose the inter-user CI of CT-contours [36, 77, 105]. This second factor is particularly relevant to PBSI as the treatment is limited to seromas with an equivalent sphere diameter of less than 3 cm [10], making PBSI seromas smaller than those selected for other forms of APBI [36, 76]. These factors all motivate improved delineation of the seromas for PBSI planning. 3DUS seroma delineation variability does not appear to be affected by many of the factors that confound CT delineation [36], particularly seroma size. Ultrasound-based delineation has been shown to be useful in localizing the tumour bed for external beam APBI, especially in cases with poor CT-seroma clarity [36, 99]. Thus, implementation of 3DUS into the planning procedure can mitigate factors contributing to delineation uncertainties and may therefore increase seed placement accuracy [36, 96, 99].

While uncertainties in the seroma delineation have been shown to correlate with the systematic component of seed displacement, total displacements are equally af-

fected by random variations in seed placement. Random displacements can result from needle deviations due to the beveled tip, tissue motion during the implant, or seed deposition inaccuracies, such as when greater than normal force is required to dislodge the seeds from the needle. Improved techniques for treatment delivery are required to reduce the magnitude of these random errors. Implementation of a 3DUS guidance system for the implant with a template projected at depth, analogous to that available for prostate seed implants, could be used to track the needle positions during insertion, relative to their planned positions and surrounding anatomy, thus allowing for corrections to be made before seeds are deposited. Such a system could also be useful in assisting in treatment setup, and could serve to improve the overall accuracy of the PBSI procedure beyond the systematic uncertainties relating to seroma delineation. An initial investigation of the potential benefits of an intra-operative guidance system for PBSI is described in the following chapter.

6.5 Conclusion

Uncertainties in seroma delineation, quantified by the variability in contouring on CT and inter-modality differences, can impact the accuracy of seed placement in PBSI as they are significantly correlated with patient specific systematic seed displacements. Random errors in seed placement are independent of factors in target delineation and may only be reduced through improved implant techniques, as will be described in Chapter 7. Efforts to improve seroma visualization in PBSI and to reduce visualization differences between planning and implant should be pursed to improve implant accuracy and confidence in PBSI. As described in Chapter 5, 3DUS may be implemented in the planning procedure, thus allowing for improved target delineation and providing analogous images for the different phases of the procedure.

Chapter 7

3D Ultrasound Implant Guidance System

The results presented in Chapters 4 and 6 have shown that random seed displacements occur during PBSI delivery, independent of systematic uncertainties relating to visualization. These random uncertainties can contribute significantly to some of the inaccuracies that may be observed. This chapter presents work to explore the potential benefits of improved image guidance in the PBSI procedure to reduce random uncertainties in PBSI delivery. A novel 3DUS scanning system designed specifically for PBSI, described in Section 3.3.1, is validated for use in needle guidance. The uncertainties associated with needle insertion are defined, and the accuracy of the registration between the treatment template and the imaging volume is evaluated. The potential benefits of implementing 3DUS into the implant procedure is assessed through an implantation of seeds into a phantom and comparing the accuracy to an implant performed following the standard clinical procedure.

7.1 Introduction

As discussed in Chapters 4 and 6, PBSI is susceptible to random errors in the delivery which can reduce implant accuracy and potentially increase user dependence and impede the adaptability of PBSI. The current PBSI procedure involves setting up the implant and inserting loaded needles into the breast through the pre-planned template positions with the aid of free-hand 2DUS. Successful delivery relies on the ability to accurately deposit the seeds close to their planned locations. The previous

chapters assessed how the differences in visualization of the seroma from planning to implant may result in intra-operative adjustments being made to the setup. Such adjustments can potentially contribute to the observed displacements of the seeds from their planned positions, although a significant component of the displacements was shown to be related to random uncertainties in the placement of seeds.

Unlike in prostate brachytherapy (Section 2.3.2), PBSI currently lacks advanced image guidance. The reliance on free-hand 2DUS requires needles to be inserted using only subjective appreciation of the limited observable anatomy. There is no virtual representation of the template at depth for needle targeting, making it challenging to ensure that needles are inserted to their planned positions, especially for peripheral needles where no spatial information from the seroma or fiducial needle is available. The lack of spatial information within the imaging volume may lead to needles being misdirected and random deviations may not be realized until after the implant is complete. Without a method to guide the implant and assess the quality during the procedure, PBSI is susceptible to user errors which can affect the accuracy of the treatment.

Errors related to the random seed displacements may be reduced by incorporating improved image guidance into the PBSI procedure. Improvements to the implant technique using advanced image guidance may improve the accuracy of the procedure and facilitate implementation. This study assesses a novel 3DUS scanning system specifically designed for PBSI implant guidance and investigates the potential impact on seed placement accuracy. The reconstruction of the system is validated and the accuracy of the registration of the PBSI template to the imaging system is evaluated. Through assessments of needle insertion accuracy into phantoms and examining the accuracy of seed placement relative to implants guided using the standard free-hand 2DUS technique, the potential benefits of 3DUS image guidance can be quantified and serve as a benchmark for clinical implementation.

7.2 Methods

7.2.1 3DUS Scanning System

The 3DUS scanning system that was used in this study was described in Section 3.3.1. In brief, the US transducer is mounted to the system which mechanically translates the probe and acquires images at known positions. Based on the scanning

geometry and positional information, the images are reconstructed into a 3D volume. The accuracy of the reconstruction was previously validated by the developers, as described in Section 3.3.2 [78].

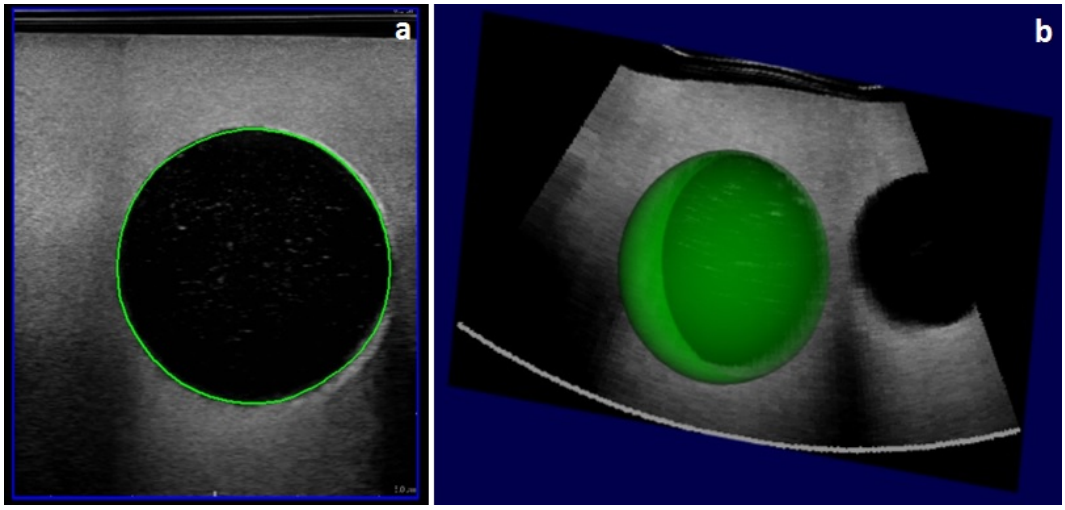

Figure 7.1: (a) Image of a sphere embedded in a solid phantom, automatically segmented, and (b) the reconstructed segmentation in 3D.

Commissioning of the 3DUS scanner was performed to ensure reconstruction accuracy of the system was consistent with the developer's specification, using the methods described in Section 3.3.2. Linear measurements of a grid of nylon strings spaced 10 mm apart, submerged in a glycerol-water solution, imaged with the system were performed to validate the linear reconstruction accuracy. A total of 160 distance measurements were manually performed in each direction, 20 at 8 different scanner depth settings ranging from 30 to 80 mm. Volumetric reconstruction was validated by imaging a sphere (diameter of 35 mm) composed of agar and glycerol embedded in a solid phantom. The sphere was segmented using the system's semi-automatic segmentation software (Figure 7.1) and the reconstructed volume was compared to the physical measurement.

7.2.2 Template Registration Evaluation

Registration of the template with the scanning system is performed by measuring the location of points with a localization arm and transforming the positions into the imaging coordinate system, as descibed in Section 3.3.1. By registering the location of the template relative to the scanning volume, the virtual template positions can

be displayed throughout the image to provide needle insertion guidance. In order to facilitate registration of the clinical PBSI template, a registration plate was constructed to provide points for the localization arm to detect, shown in Figure 7.2. The registration plate contains 1.3 mm pins at positions 27.5 mm and 37.5 mm vertically and laterally, respectively, corresponding to the corner positions of the template. The pins can therefore be used to fix the registration plate to the template at a known and reproducible position. Divots were precisely machined into the registration plate (2 on each the top and left side) such that when the localization arm is positioned at each divot location the coordinates of the centre of the spherical tip are known relative to the centre of the face of the template. The registration process from the template coordinates to the imaging coordinates described in Section 3.3.1 is then performed in order to display the template positions in the 3D image.

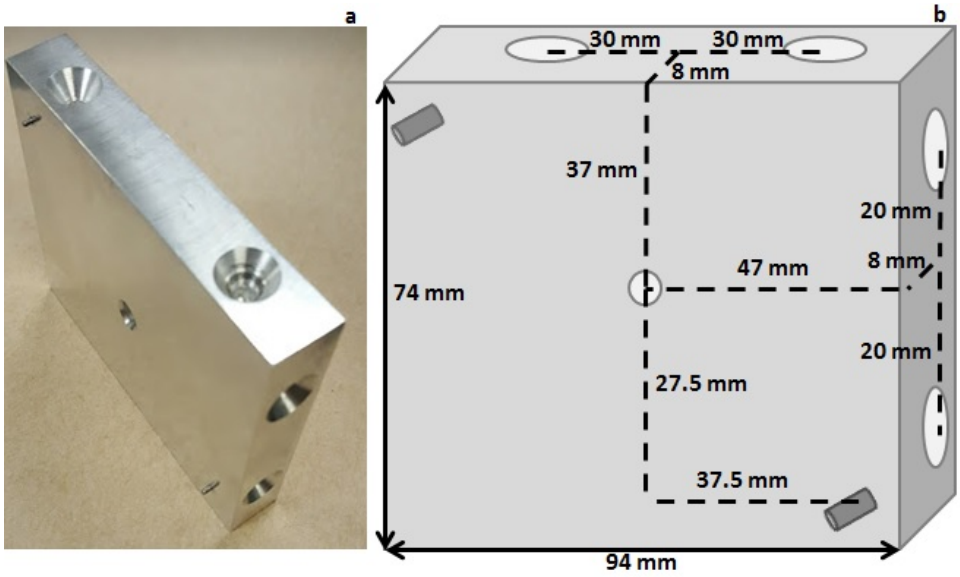

Figure 7.2: (a) Registration plate used for localize the template with the scanning system. Divots for the localization arm's spherical tip are machined at precise locations relative to the center and pins in the corner fix the plate to the PBSI template. (b) Schematic of the registration plate.

Validation of the template registration process using the registration plate was performed to ensure accurate extrapolation of the template positions in the image. In order to evaluate the position of the virtual template positions in the imaging volume relative to the actual positions, a QA jig was constructed which positions the scanner orthogonally to the template plane. The face of the QA jig had holes machined with the width of the fiducial needle in precise locations corresponding

to 8 template grid positions and could accommodate the registration plate as if the template was positioned in front of it. The registration plate was placed on the front face of the jig and the localization arm was used to measure the location of the divots and perform the registration (Figure 7.3a). To assess the registration, needles were inserted through the jig in a liquid medium (to prevent deformation), thus representing a straight line from the template plane into the imaging volume (Figure 7.3b). Plastic sleeves on the needles were positioned in order to achieve known and consistent implant depths. The needles were imaged in a solution of water and isopropyl alcohol (7.25% by volume) to achieve a speed of sound of ∼1540 m/s [82] in order to produce accurate localization of the needles in the imaging volume.

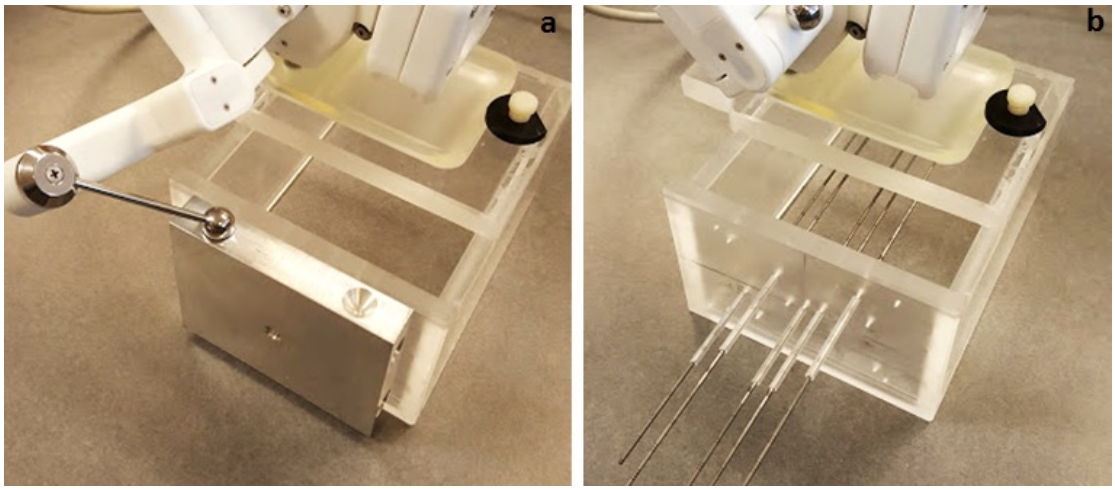

Figure 7.3: (a) The registration plate on the face of the QA jig used to localize the virtual template position. (b) Needles inserted through the QA jig at various positions into the imaging volume. Sleeves on the needles ensure consistent insertion depth.

The needles in the images were segmented using the automatic segmentation tools in the 3DUS software (Figure 7.4) and compared to the virtual template positions. The trajectory separation, measured as the mean distance from the segmented needle to the template position across the length of the needle, was determined as well as the angular separation between the two trajectories ($\Delta\theta$) calculated by

$$\Delta\theta = \arccos\left(\frac{\vec{N}\cdot\vec{T}}{\|\vec{N}\|\|\vec{T}\|}\right) \tag{7.1}$$

where $\vec{N}$ and $\vec{T}$ are the vectors of the needle and template trajectories being compared [53]. Additionally, as needles were inserted to known distances from the QA jig face,

the position and depth of the needle tips were compared to the expected position based on the coordinate transformation.

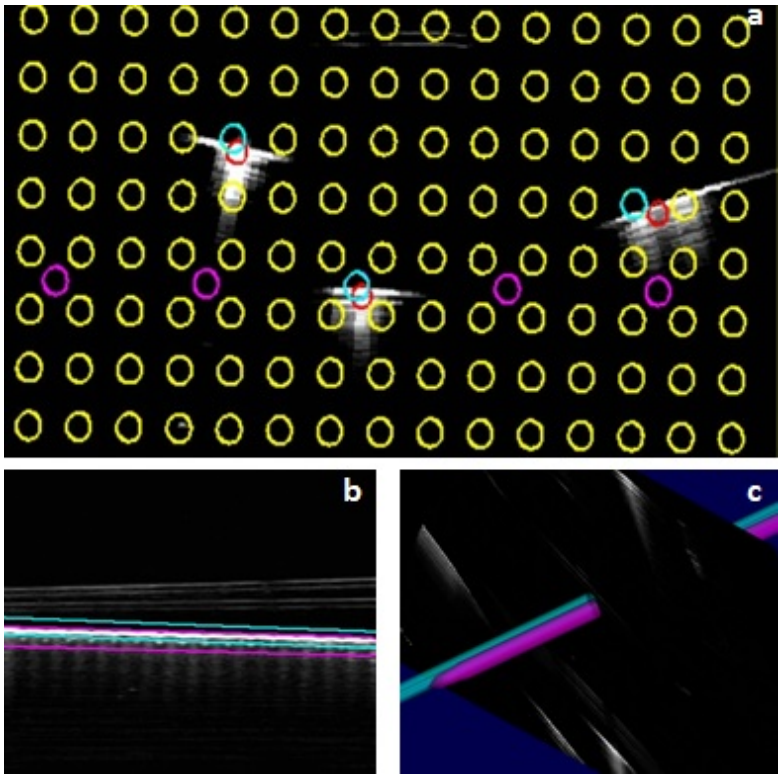

Figure 7.4: (a) Virtual representation of the template in the QA jig geometry. Needles (red) are inserted into the template positions highlighted in blue. A segmented needle (purple) relative to the template position (blue) (b) along the length of the needle and (c) in a 3D visualization.

Registration of the template positions within the imaging volume was further validated using the clinical PBSI template in 3 different orientations relative to the scanner: orthogonally and 9 cm from the scanning center (Orthogonal), at a 5° angle in the insertion direction and 12 cm distance (Tilt), and 13° insertion angle and 10 cm distance with 10° lateral angle and 4° rotation in the template plane (Oblique), shown in Figure 7.5. The template was submerged in the isopropyl-water solution and the scanner was mounted at the liquid's surface. The registration plate was fixed to the template face and the localization measurements performed. The registration plate was removed and needles were inserted into several of the template holes. Needles inserted through the central holes were of the same design as the fiducial needle, and could be locked into place using the mechanisms of the template. Needles in the other template positions were the beveled needles used for seed deposition. Needles were

subsequently imaged, segmented, and compared to their respective virtual template positions to assess the accuracy of the template visualization.

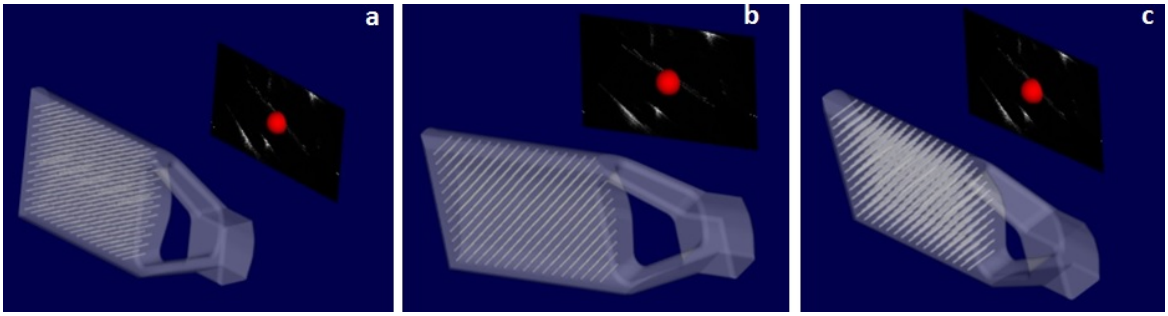

Figure 7.5: The template positioned in the (a) Orthogonal, (b) Tilt, and (c) Oblique positions relative to the scanning volume. The scanning plane represents the central slice of the 3DUS reconstruction, and the red sphere is at the center of the imaging volume.

7.2.3 Needle Insertion Characterization

In order to characterize the magnitude of the random uncertainties that may occur in needle insertion and assess the potential benefits of the 3DUS guidance system on placement accuracy, needle insertions were performed in an anthropomorphic breast phantom (Blue Phantom, CAE Healthcare, Sarasota, FL). The scanning system was positioned on the breast phantom, ensuring good contact of the TPX plate and the phantom surface, and the template was fixed on the lateral side, as for real implants (Figure 7.6). The template registration was performed using the registration plate, and needles were subsequently inserted into the phantom without the assistance of the 3DUS guidance by a non-expert user. 3DUS images were acquired of the needles after they had been inserted and their resulting positions relative to the extrapolated template positions were evaluated. Based on a qualitative assessment of the imaged needles relative to their planned template positions after the scan, the needles were retracted and re-inserted in order to attempt to improve the accuracy of the insertion. After re-insertion, the needles were again imaged and their accuracy evaluated relative to the template position. The reduction in the insertion error from the original insertion with no guidance to a single re-insertion with the assistance of the guidance were assessed by comparing the trajectory separations.

Figure 7.6: Registration of the scanning system with the PBSI template before insertion into an anthropomorphic breast phantom.

7.2.4 3DUS Guided Seed Placement

The overall effect of improved image guidance on the seed placement accuracy was evaluated by implanting inert seeds into phantoms with and without the aide of the 3DUS guidance system. The phantoms were blocks (13×12×10 cm) composed of agar and glycerol (80 mL and 35 g per L of water, respectively) to achieve a speed of sound of ∼1540 m/s, as described in Section 3.3.2 [78, 81]. For contrast, 12 g of psyllium hydrophilic mucilloid fiber was added per litre of solution [74]. The phantoms were created by pouring the agar solution into a mold, letting it solidify, and then pouring another layer in order to create a boundary region which could aide in implant guidance, similar to how the seroma is used to guide the implant depth in PBSI. A CT scan of the phantoms was performed to create an implant plan (Figure 7.7).

A treatment plan, resembling a clinical PBSI plan, was created following the standard planning procedure outlined in Section 2.4.2. A 3 × 3 grid of needles spaced 1 cm apart centred around the fiducial needle was planned with a total of 40 seeds. The fiducial needle entry point was defined at known locations on the phantom and the insertion direction was perpendicular to the phantom surface in order to minimize systematic errors related to the setup. A treatment plan report

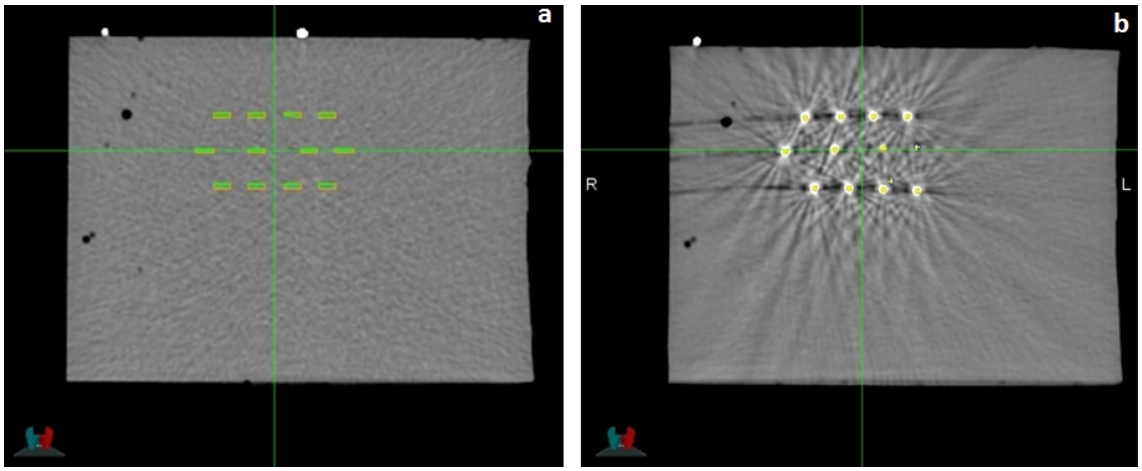

Figure 7.7: (a) Planning CT of the block phantom and the planned seed locations (green). The boundary region, under the marker at the centre of the block, is not visible in the CT image. (b) Post-implant CT of the block phantom.

was generated that identified which needles were to be implanted into which positions and the corresponding depth. Needles loaded with inert seeds based on the treatment plan were used for the phantom implants.

For the implant procedure, the fiducial needle entry point was marked at the planned location on the phantom and the template was positioned orthogonally to the block. The procedure was first performed using the 3DUS guidance system. The template position was registered to the imaging system, as described in Section 3.3.1, and the fiducial needle was inserted and scanned for verification. The boundary region was not clear in the US images, thus the implant depth was set only on physical measurements of the needle protrusion to match the treatment plan. Needle insertion was performed by an expert oncologist skilled in brachytherapy. The bottom row of needles were inserted into the planned template positions and a scan was performed to assess the accuracy of the needle positions relative to the extrapolated template positions at depth. Based on the visualized locations of the needles, the insertion was adjusted by redirecting the needles to achieve final positions that were closer to the planned location. After final verification, the needles were positioned at the correct depth and the inert seeds were deposited. The insertion process was repeated for each subsequent row.

Following the completion of the implant, the procedure was repeated using only free-hand 2DUS guidance. Based on the needles observed under 2DUS, the insertion was adjusted to make the trajectories approximately parallel to the fiducial needle,

with no guidance to the actual template position at depth.

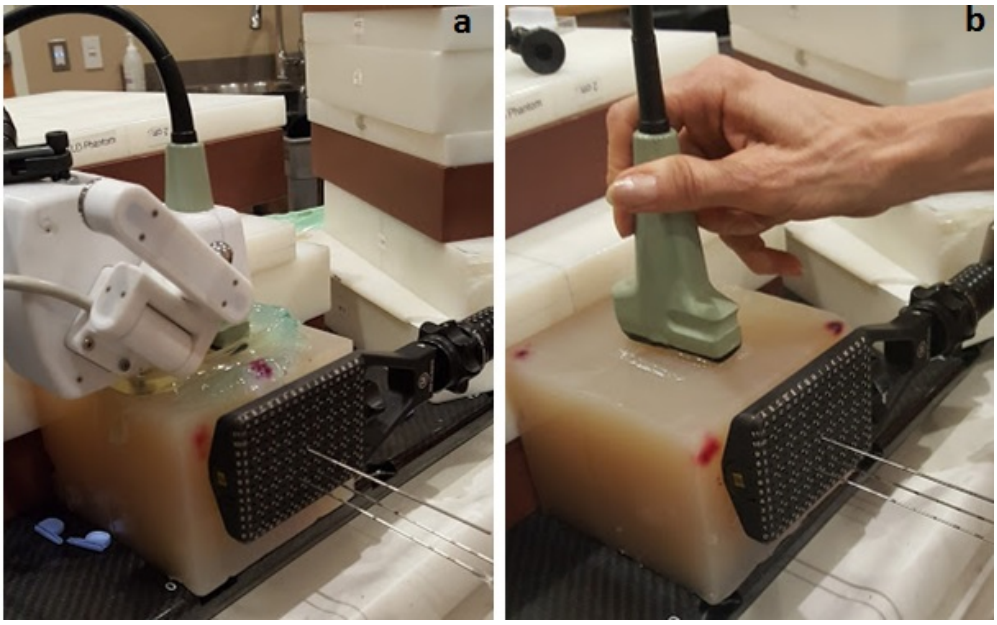

Figure 7.8: Implant of seeds into a block phantom using (a) 3DUS guidance and (b) free-hand 2DUS guidance.

Following the implants, a CT scan was performed for each phantom (Figure 7.7b). Seed positions were unambiguously identified on the post-implant CTs. The phantoms were non-deformed blocks and thus rigid registration of the planning and post-implant CTs was trivial. The planned and implanted seed positions and the transformation matrix were exported and the seed matching process described in Section 3.1.2 was used to evaluate the accuracy of each implant.

7.3 Results

7.3.1 Image Reconstruction Validation

Table 7.1 summarizes the measured separations between the strings in the grid, measured at 8 different US scanning depth settings. The mean (± SD) measured grid separations were 10.1 ± 0.1 mm, 10.0 ± 0.2 mm, and 10.0 ± 0.1 mm in the elevational, axial, and lateral directions, respectively. All measurements were within 2% of the expected value in the axial and lateral directions and 3% in the elevational direction. The measured values were not significantly different from the expected 10 mm separation in each direction, and no significant differences between directions or

Table 7.1: Mean (SD) linear measurements of the distance between strings spaced 10 mm apart in grid imaged with the 3DUS scanning system performed at 8 different US depth settings. 20 measurements were performed in each direction at each depth.

Depth (mm)	Elevational (mm)	Axial (mm)	Lateral (mm)
30	10.0 (0.2)	10.1 (0.1)	10.1 (0.1)
35	10.1 (0.1)	10.0 (0.1)	10.1 (0.1)
40	10.1 (0.1)	10.0 (0.2)	10.0 (0.1)
46	10.1 (0.2)	10.0 (0.2)	10.0 (0.1)
52	10.1 (0.2)	10.0 (0.2)	10.1 (0.1)
60	10.1 (0.2)	10.0 (0.2)	10.0 (0.1)
69	10.1 (0.2)	10.0 (0.2)	9.9 (0.1)
80	10.0 (0.1)	10.0 (0.1)	9.9 (0.1)
Mean	10.1	10.0	10.0
SD	0.1	0.2	0.1

imaging depths were observed. The measured segmented volume of the embedded sphere was 21.9 ± 0.3 cm^3 and was a mean 3 ± 1% smaller than the expected value (22.4 cm^3).

7.3.2 Template Registration Accuracy

The mean (± SD) angular separation of the calculated template trajectories and the imaged needle positions in the QA jig was 0.8 ± 0.3° and the mean positional difference of the trajectories along the visible length of the needle was 1.4 ± 0.2 mm, as shown in Table 7.2. No significant trends between the trajectory positional differences and the location within the image was observed, however the most lateral needles appeared to have the greatest angular separation (1.1 ± 0.1° and 1.1 ± 0.6°) relative to the central needles (∼ 0.8°). The mean difference in needle tip location from the calculated location based on the insertion depth was 1.5 ± 0.3 mm. Similar to the mean trajectory difference, no significant correlations were observed between the tip positional agreement and the template position.

Registration with the PBSI template in different orientations resulted in similar agreement with the imaged needles as the QA jig, summarized in Table 7.3. Mean positional agreement of the calculated trajectories and needles was 1.3 ± 0.9 mm, with mean angular separation of 0.9 ± 0.5°. No significant difference were observed between trajectory separations in the axial and lateral directions, and no systematic directional differences were observed. Mean trajectory differences were 1.6 ± 1.2 mm,

Table 7.2: Mean (SD) angular separation ($\Delta\theta$), trajectory separation, and difference in needle tip position of needles imaged in the QA jig relative to the calculated template positions given by the distance from the template centre (up/down, right/left).

Position (mm)	$\Delta\theta$ (deg)	Trajectory separation (mm)	Needle tip difference (mm)
0, 0	0.8 (0.2)	1.2 (0.6)	1.7 (0.6)
2.5, 7.5	0.7 (0.2)	1.3 (0.6)	1.2 (0.4)
-2.5, -7.5	0.8 (0.3)	1.1 (0.5)	1.1 (0.3)
12.5, -12.5	0.7 (0.5)	1.5 (0.2)	1.4 (0.3)
-12.5, 12.5	0.4 (0.3)	1.5 (0.6)	1.4 (0.1)
22.5, 22.5	0.5 (0.2)	1.4 (0.6)	1.9 (0.3)
7.5, 27.5	1.1 (0.1)	1.4 (0.3)	1.5 (0.3)
-7.5, -27.5	1.1 (0.6)	1.7 (0.1)	1.2 (0.2)
Mean	0.8	1.4	1.5
SD	0.3	0.2	0.3

Table 7.3: Mean (SD) total and directional (axial [Δy] and elevational [Δz]) trajectory separation difference between the visualized template positions and imaged needle positions for 3 different template orientations relative to the scanner. Needle locations are given by the distance to the template center (up/down, right/left).

	Position (mm)	Δy (mm)	Δz (mm)	Total (mm)	$\Delta\theta$ (deg)
Orthogonal	0, 0	-0.1 (0.1)	0.4 (0.3)	0.5 (0.2)	1.2
	0, -15	0.8 (0.0)	0.1 (0.1)	0.8 (0.1)	0.3
	0, 30	0.4 (0.0)	3.3 (0.2)	3.4 (0.2)	0.5
	12.5, -22.5	-0.5 (0.0)	0.3 (0.0)	0.6 (0.1)	0.2
	-7.5, 12.5	-0.8 (0.2)	1.2 (0.1)	1.5 (0.1)	0.7
Tilt	0, 0	0.6 (0.3)	-0.8 (0.4)	1.1 (0.1)	1.9
	0, -15	0.0 (0.2)	-1.1 (0.2)	1.1 (0.2)	1.1
	12.5, -17.5	-1.9 (0.4)	-0.4 (0.1)	2.0 (0.4)	1.8
	-7.5, 12.5	-0.2 (0.1)	0.4 (0.1)	0.5 (0.1)	0.8
Oblique	0, 0	0.3 (0.1)	0.8 (0.2)	0.9 (0.2)	1.1
	0, -15	0.0 (0.1)	0.5 (0.0)	0.5 (0.0)	0.3
	0, 30	-0.1 (0.1)	1.5 (0.2)	1.6 (0.2)	0.9
	-7.5, 12.5	-1.2 (0.3)	0.7 (0.1)	1.5 (0.2)	1.4
	-12.5, -7.5	0.9 (0.1)	1.4 (0.2)	1.7 (0.1)	0.8
	Mean	-0.3	0.6	1.3	0.9
	SD	0.7	1.2	0.9	0.5

1.2 ± 0.6 mm, and 1.2 ± 0.5 mm in the Orthogonal, Tilt, and Oblique orientations, respectively, and thus the positions and orientations evaluate did not appear to affect

the registration accuracy. No trends between the trajectory separation or angular separation and the needle position were observed

7.3.3 Insertion Characterization

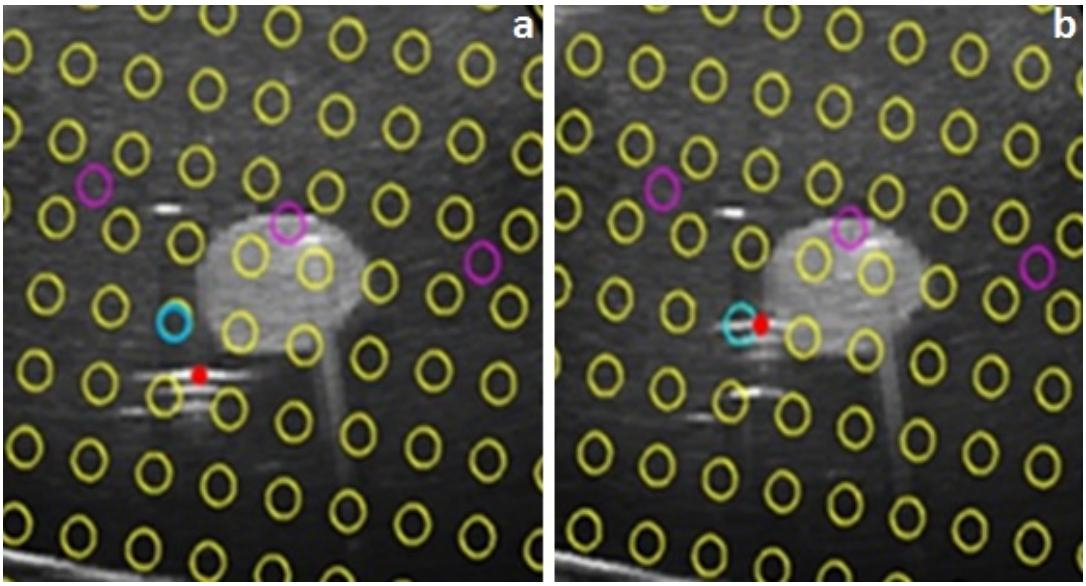

Figure 7.9: (a) Insertion of a needle (red) into an anthropomorphic breast phantom though a template hole (blue). (b) Re-insertion of the needle with adjustment after assessment with 3DUS guidance achieves an implanted position closer to the target.

Needles were inserted into the anthropomorphic breast phantom in 5 different template positions (3 separate template orientations). Insertions without the aide of imaging has a mean positional agreement with the template trajectories within the image of 3.7 ± 1.4 mm, and a mean angular separation of 4.2 ± 0.9°. Such differences in the planned to implanted needle positions represent the magnitude of random uncertainties that can occur from needle insertion alone, contributing to the seed displacements observed in Chapter 4. Following a qualitative evaluation with the 3DUS guidance system, then needles were re-inserted to achieve a mean positional agreement with the template positions of 2.0 ± 0.9 mm. Overall, the trajectory separation was reduced by a mean 1.6 ± 0.7 mm, representing a mean 47 ± 16% increase in the needle insertion accuracy. Mean angular separation for the re-insertion was reduced to 2.7 ± 1.3° compared to the original insertions.

Figure 7.9 shows how the 3DUS guidance system can potentially improve the accuracy of implanted needles. In this example, the original needle insertion was a

mean 3.9 ± 0.5 mm from the planned template position due to the random uncertainties associated with needle insertion. After evaluation of the positioning with the 3DUS system, the needle was re-inserted by directing it upwards and to the left of the original insertion. The resulting position was a mean 1.7 ± 1 mm from the target, decreasing the mean distance from the target position by 55% and improving angular trajectory separation from 2.9° to 1.2°.

7.3.4 Implant Accuracy With 3DUS Guidance

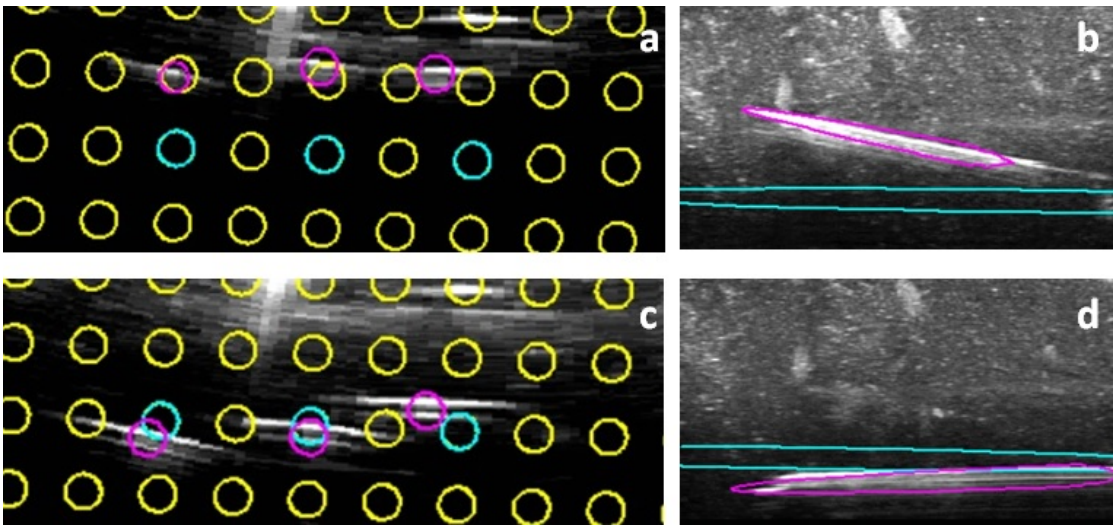

Figure 7.10: (a) Original insertion of needles (purple) implanted into the block phantom through template position (blue) in the needles-eye-view. (b) Trajectory separation between the segmented needle position (purple) and the template position (blue) visualized along the length of a needle. (c) Re-insertion of the needles following assessment of the original insertion with 3DUS guidance, and (d) the resulting improvement of the needle position.

The needles implanted into the block phantom before imaging were a mean 3 ± 2 mm from the expected template positions with a mean 5 ± 4° trajectory separation. Following imaging, 4 needles were re-inserted with adjustments based on their visualized positions in the image: the first 3 needles and 1 needle in the top row. As demonstrated in Figure 7.10a, the initial insertion of the bottom row of needles varied greatly in position and direction from the extrapolated template positions. The adjusted needles were a mean 5 ± 2 mm from the template positions in the original insertion, which improved to 1.3 ± 0.9 mm after re-insertion. Overall, implant

accuracy was improved by a mean 74 ± 16% for the re-inserted needles. Angular separation additionally improved from a mean 9 ± 4° to 2 ± 1°.

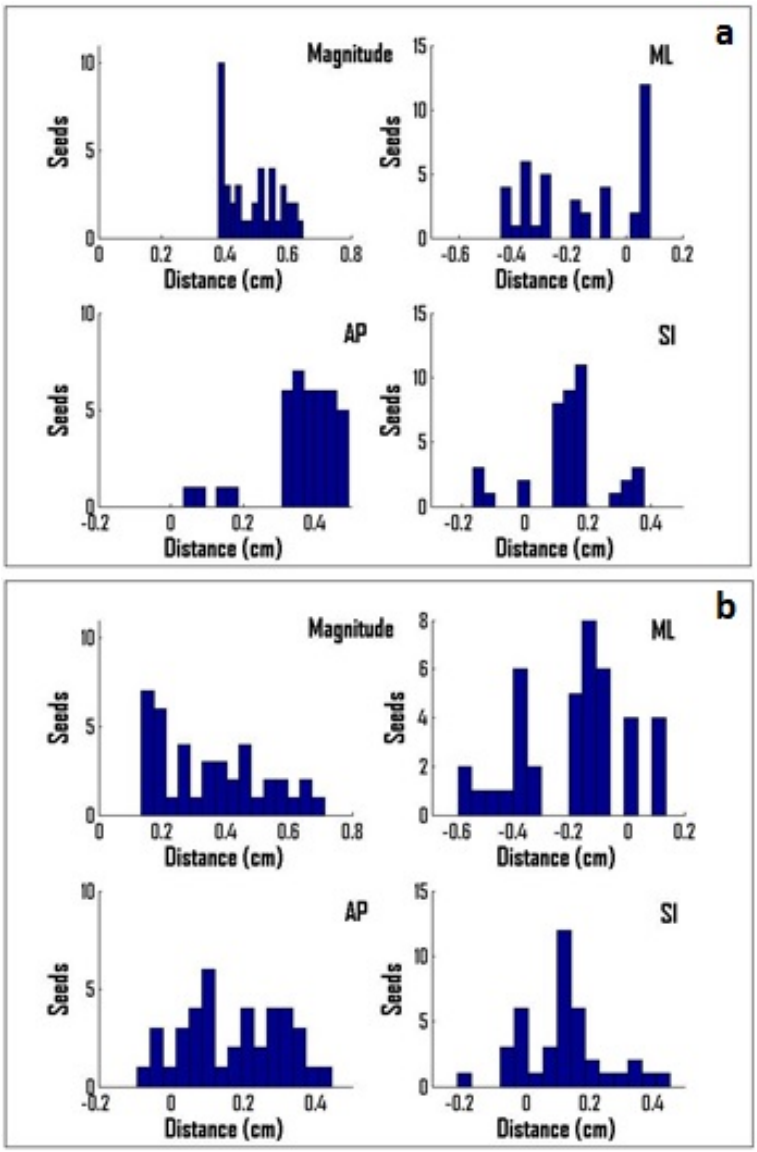

Figure 7.11: Histograms of the total and directional (ML, AP, SI) seed displacements for implants in a block phantom using (a) free-hand 2DUS guidance, and (b) 3DUS guidance.

Figure 7.11a shows the total and direction distributions of seeds implanted using only free-hand 2DUS guidance. The seeds were implanted a mean 5 ± 1 mm from their planned position, with individual seeds displacements between 3.8 and 6.5 mm. Mean directional displacements were -1 ± 2 mm, 4 ± 1 mm, and 1 ± 1 mm in the ML, AP, and SI directions, respectively. As can be seen in Figure 7.11a, a

large number of seeds are displaced in the anterior direction, while displacements in the other directions are more even distributed close to zero. The mean random component of the seed displacement was 3 ± 1 mm. The implant using the 3DUS guidance system had a mean total seed displacement of 3 ± 2 mm, as shown in Figure 7.11b, with individual displacements ranging from 1.3 to 7.1 mm. Mean directional displacements were -2 ± 2 mm, 2 ± 1 mm, and 1 ± 1 mm in the ML, AP, and SI directions, respectively. The random component of the seed displacement for this implant was 2 ± 1 mm.

While systematic offsets were minimal in both implants relative to those seen in clinical implants (Chapter 4), small mean directional displacements did occur in both implants. The largest systematic displacement occurred in the AP direction in both implants, potentially related to positioning of the fiducial entry point on the phantom. Greater displacements in the ML direction were observed in the 3DUS implant compared to the 2DUS implant, corresponding to variations in the depth of the implant. Overall, seeds were implanted more accurately in the 3DUS guided implant ($p < 0.001$), although the magnitude of the random displacements was not significantly different ($p = 0.3$).

7.4 Discussion

The results of Chapters 4 and 6 have shown that seed displacements occur during the PBSI procedure that are not associated with systematic uncertainties in the delivery, and which may not be reduced through improved planning and setup methods. These random seed displacements can contribute significantly to the overall accuracy of seed placement in PBSI. Without a system to guide needle insertion, such as the TRUS guidance used in prostate seed implant brachytherapy, needle insertion is susceptible to random errors, characterized in Section 7.3.3. The overall accuracy of the seed implant procedure is therefore highly reliant of the skills of the delivering oncologist to achieve accurate needle positioning. Such user dependence can potentially impede adoption of the procedure by less experience practitioners and limit the overall accuracy of the technique. The novel 3DUS scanning system for PBSI presented in this chapter provides a method to guide implant and make intra-operative adjustments to needle positioning before seeds are deposited. This study assessed the accuracy of template registration with the scanning system in order to ensure accurate target positioning in PBSI implant guidance, and assess the potential benefits of system's

implementation into the implant procedure.

The results presented in Section 7.3.2 showed that the template could be accurately registered to the imaging volume using the registration plate and localization arm. Overall, the virtual template positions were a mean 1.4 ± 0.2 and 1.3 ± 0.9 mm from the imaged needles in the QA jig and template setups, respectively. The AAPM TG-128 guide for prostate brachytherapy ultrasound QA defines the tolerance of template visualization relative to needles inserted in a liquid medium to be a maximum of 3 mm [110]. The imaged positions in the validation of the PBSI system were consistently within this limit. The current PBSI procedure uses a projection of the PTV on the skin surface orthogonal to the needle insertion direction as a guide for imaging. Therefore, the scanning system would likely be positioned orthogonally to the template in clinical implementation. However, adjustments to the orientation (Figure 7.5) were examined to ensure accurate registration outside of orthogonal setups. The orientation did not appear to affect the accuracy of the template visualization and all virtual template positions were within 3 mm of the imaged needle position.

The registration of the template to the imaging volume involves the combination of each of the individual transformation described in Section 3.3.1, each of which is susceptible to errors during the development process. Several other uncertainties in the validation process likely contributed to the overall differences in trajectories observed in this study. Motion of the template after localization, particularly due to attaching and removing the registration plate, or instability of the localization arm when recording the position will additionally contribute to the accuracy of the template visualization. The needles were assumed to be inserted through the QA jig and template in a straight line to provide a true measure of the template positions, but needles sagged in the imaging field, especially at greater depths, which can potentially contribute to the discrepancies observed from the extrapolated template positions. Additionally, the lateral needles were often blurred in the images, as seen in Figure 7.4, which made precise localization uncertain.

The implants described in Sections 7.3.3 and 7.3.4 show the magnitude of random displacements can result from the insertion of needles into solid material. Despite inserting the needle in the correct template position, the needles in the simulated implant were a mean 5 ± 2 mm from the target position with an angular separation of $9 \pm 4^\circ$ before re-insertion. Similar deviations would therefore contribute significantly to the random seed displacements that were observed in clinical implants in Chapters 4 and 6 [60]. While adjustments to the needle trajectory can be made with 2DUS

imaging, based on the observed needle trajectory relative to the fiducial needle, the final trajectories would only be approximations based on the user's interpretations. The 3DUS guidance system can therefore reduce operator dependence by eliminating the need for subjective assessment of the needle positioning.

Overall seed placement accuracy for the 3DUS guided implant and the free-hand US guided implant was 3 ± 2 mm and 5 ± 1 mm, respectively. Greater overall displacement was observed in the free-hand implant, but was primarily due to the magnitude of systematic displacements, particularly in the AP direction. Mean random displacements were not significantly different between the two implants. Re-insertions were performed with 4 of the 9 implanted needles after observation with the 3DUS guidance system, thus decreasing the displacements that would have result from their initial insertions. Three of the adjusted needles were in the first implanted row, all of which needed to be directed downwards. Based on the required needle adjustments after the original insertion, the expert user modified the insertion technique for subsequent needles, deliberately directing needles downwards. As a result, the middle row required no adjustments and the top row required only one needle to be re-inserted. Since the free-hand US guided implant was performed immediately following the 3DUS guided implant, insertion may have been biased to achieve a higher level of accuracy compared to if the implant was performed completely independently. A more extensive evaluation of the 3DUS guidance system's impact on the seed placement accuracy is required to accurately quantify the reduction in random uncertainties that may be achieved through improved image guidance, as discussed further in Section 8.2. In addition, an assessment of the feasibility for clinical implementation through more clinically relevant implant simulations should be pursued.

Random seed displacements were shown to average approximately 7 mm in clinical PBSI implants (Chapters 4 and 6) [60]. Greater overall accuracy is expected in simulated implants due to the absence of anatomical motion, minimal systematic uncertainties, and the simple geometry of the block phantom. However, the validation and simulated implant in this chapter have shown that the random displacements can be reduced with the 3DUS implant guidance system, accurate to less than 3 mm, thus allowing for a significant increase in seed placement accuracy. As shown in Chapter 4, a limit to the mean total seed displacement in an implant which allows for acceptable dosimetry exists. Reduction of random displacements through the implementation of 3DUS guidance can potentially improve implant dosimetry, and may help to achieve more acceptable coverage in implants where greater displacements would otherwise

be occur.

7.5 Conclusions

A novel 3DUS system designed specifically for PBSI implant guidance was validated to achieve accurate registration of the template positions within the imaging volume. Random uncertainties in needle insertion exist, independent of systematic setup errors. Large deviations in the implanted needle position relative to the target position can therefore occur without the aide of image guidance, potentially reducing the accuracy of seed placement during implant. The 3DUS guidance system shows potential for improved needle insertion accuracy by allowing for adjustments to be made to deposit seeds closer to their intended position. Implementation into the PBSI procedure can therefore reduce user dependence and improve the overall accuracy and confidence of the technique.

Chapter 8

Conclusions and Future Considerations

PBSI is a promising technique that can significantly benefit many women with early stage breast cancer due to the reduced treatment burden relative to other forms of breast conserving therapy. As stated in Section 1.3, adoption of PBSI has been limited and implementation may be facilitated through an improved, standardized procedure which reduces user dependence in the technique. The goal of the work presented in this dissertation was to quantify uncertainties in the current PBSI treatment planning and delivery procedures and define the methods which can improve the treatment accuracy, reduce user dependence, and promote implementation of the technique. This chapter summarizes the conclusions of the presented work which establish the foundation for improvements in the PBSI brachytherapy technique. Based on the results of this work and the necessary steps required to bridge the gap between development and clinical implementation, future considerations and suggestions for further work are discussed.

8.1 Conclusions

As a novel treatment option, PBSI has not been comprehensively evaluated and no thorough assessment of the uncertainties in the procedure have been performed. Although the technique has been successfully implemented by a few expert practitioners, this work was motivated by the fact that PBSI has not been widely adopted and concerns in the adaptability of the procedure have currently not been addressed. The

study presented in Chapter 4 was the first to perform a comprehensive assessment of the accuracy of seed placement in PBSI. Based on a cohort of 20 implants, the mean seed displacement from the planned positions was 9 ± 5 mm. Overall, no significant trends or systematic errors were observed in the entire cohort, including seeds implanted into the different anatomical regions of the breast (near the chest wall, skin, and seroma), thus refuting reported concerns that seeds implanted in these regions may be susceptible to greater errors in accuracy [34]. The seed placement accuracy, in general, was not observed to significantly impact the resulting post-implant dosimetry, thus PBSI was shown to provide a safe and effective treatment within the limits of the implant uncertainties. However, implants with mean seed displacements greater than approximately 11 mm were more likely to result in less than optimal ETV coverage, suggesting that minimizing seed displacements may stand to improve treatments. The effects of seed placement on treatment dosimetry were similarly observed in an independent cohort of implants presented in Chapter 6.

Evaluation of seed placement accuracy identified the magnitude of systematic and random uncertainties that occur during implant. In contrast to the cohort population, within individual patients systematic displacements were observed. Directional shifts in the directional displacement distributions varied widely between implants, with no inter-patient trends. Mean random displacements in the cohort was 7 ± 4 mm, contributing significantly to the overall displacements. Based on the displacements observed in this study, potential improvements to the procedure were explored to address the individual components and improve implant accuracy.

The analysis performed in Chapter 5 examined the theoretical effects of seroma visualization on implant accuracy and treatment dosimetry. Inherent differences in the size and positions of seromas delineated on CT and US, with a median (range) CI of 0.51 (0.32 - 0.65), resulted in significant under-dosing of the PTV defined based on US when planning PBSI treatments using CT alone. Intra-operative adjustments to the needle positioning are sometimes necessary during clinical implants due to the location of the seroma observed on US during implant. This study showed that adjusting the treatment plan to center on the seroma visualized on US reduced the coverage to the CT-defined PTV in all cases (mean 10 ± 8%). Centroid positional differences resulting in the plan shifts were a mean 7 ± 3 mm, similar to the magnitude of the systematic displacements observed in the seed displacement in Chapter 4. Therefore, the visualization differences can potentially result in reduced treatment and seed placement accuracy when adapting the CT-based plan to the US-guided

procedure. Incorporating 3DUS into the treatment planning procedure was shown to be able to compensate for these visualization differences by ensuring acceptable coverage to target volumes on CT and US, with a moderate increase in the overall treated volume, while providing a treatment plan that may more accurately translate to the OR.

The impact of seroma delineation on seed placement accuracy in PBSI was directly investigated in Chapter 6. Correlations were observed between the mean seed displacement and the inter-user CI of seromas delineated on CT ($r = 0.74, p = 0.01$) and between the seroma volume difference between US and CT ($r = 0.65, p = 0.04$). These results indicate that as the clarity of seroma on CT decreases and the differences between the two modalities increases, the accuracy of seed placement may be reduced. The correlations were maintained when assessing the relationships with only the systematic component of the seed displacements, supporting the hypothesis that uncertainties in the visualization can contribute to systematic errors in treatment setup and delivery. Improved seroma visualization in treatment planning through the implementation of 3DUS into the planning procedure, as described in Chapter 5, may therefore decrease the need for subjective intra-operative adjustments and potentially improve implant accuracy and reduce user-dependence in the delivery.

Unlike the systematic displacements observed in Chapter 6, the random component of the seed placement accuracy was not found to be dependent on factors relating to target delineation. Therefore, it is unlikely that improved visualization in treatment planning would result in a reduction of these random uncertainties. Chapter 7 demonstrated the magnitude of errors that can occur during needle insertion, where the random deflecting and bending of needles would result in the displacement of seeds from their intended position. A 3DUS system designed for PBSI image guidance was validated to provide accurate target localization for needle insertion. The virtual representation of the template at depth allows for adjustment and re-insertion of needles to achieve a significant reduction in the random needle insertion errors. Re-insertion by an expert practitioner improved the trajectory separation of needles from their planned positions by a mean $74 \pm 16\%$, representing a significant reduction in the seed displacements that could occur in the absence of image guidance. Random displacements between implants performed with the 3DUS guidance system and using the standard free-hand 2DUS technique were not observed to be significantly different ($p = 0.3$), although a more comprehensive comparison of the two techniques is required to determine the impact of the guidance system on seed placement accu-

racy. However, improvements to the needle insertion accuracy with the assistance of 3DUS indicate that overall treatment accuracy may be improved through the clinical implementation of such a system.

PBSI has been shown to be a safe and effective treatment for select early-stage breast cancer patients through a limited number of clinical trials but, as shown in this work, is susceptible to errors in the delivery which can potentially impact treatment accuracy and impede the implementation of the technique as a standard treatment option. This dissertation highlighted some of the areas where uncertainties in the procedure exist and assessed methods to mitigate these factors. Through the integration of advanced US imaging in both treatment planning and delivery, a more standardized technique can be achieved. With the potential increase to the accuracy and confidence in PBSI, widespread adoption may be facilitated, thus introducing a new treatment option to many breast cancer patients.

8.2 Future Considerations

While the goal of this research was to establish the necessary steps to improve PBSI and promote widespread adoption, there exists a large gap between the development and clinical implementation of tools and procedures aiming to improve PBSI. Continued developments and investigations are required before these steps can be integrated within the clinical PBSI procedure. The results presented in Chapters 5 and 6 demonstrated that variability of seroma delineation can result in intra-operative adjustments to the treatment plan and, subsequently, systematic displacements of seeds from their planned positions. An accurate and reliable method to acquire 3DUS images and register them to the planning system is required in order to make US imaging a standard component of PBSI treatment planning. For example, the novel 3DUS scanning system, or a similar device, could be integrated into the planning CT procedure, as was performed with the now obsolete Clarity US system in Chapter 6. The localization arm of the 3DUS scanning system could provide a method of tracking known locations in the CT image. Based on their locations in the US image coordinate system, a rigid registration between the two image sets could be performed, thus allowing the visualization of the seroma on US to be used in the planning procedure. One potential challenge in the registration process is deformation of the anatomy when acquiring 3DUS images, which should be taken into careful consideration when integrating the US images into the planning procedure. While the TPX plate of the scanning system

can minimize the pressure required to obtain a clear image, limited contact with the breast surface may require more force to be applied. The magnitude of deformation is not currently know, but could be quantified by performing CT imaging with and without the scanning system in place and evaluating the differences in the anatomy, particularly the seroma shape and location. Based on the mutual information of the CT and US images, a non-rigid, deformable registration between the two modalities could theoretically be performed. A registration algorithm would provide a faster and more convenient method of registration, potentially eliminating the need for images to be acquired in identical patient positioning.

An initial assessment of the 3DUS image guidance system was presented in Chapter 6, but more work is required before the scanner can be confidently implemented in the delivery procedure. The comparison of the accuracy of the system to the standard free-hand US guided technique was performed in a single implant in a simple block phantom. A comprehensive comparison of the two techniques should be performed using multiple implants in anthropomorphic breast phantoms. Simulations using clinically realistic setups would provide a more accurate assessment of the system in the implant procedure. Additionally, implants should be randomized and multiple users could perform implants in order to reduce bias between the two delivery techniques. A thorough comparison of the two techniques would provide an accurate evaluation of the guidance system relative to the current procedure and allow for an assessment of the clinical utility and feasibility of such a system. Upon validation, an initial study of several clinical patient implants can be performed to demonstrate the usability of the system during clinical implants, while further assessing template registration and needle localization accuracy, and ensuring that implants guided with 3DUS can provide improved treatment accuracy relative to the standard technique.

While the guidance system as presented can provide a significant benefit to PBSI, it also creates opportunities for further developments. As discussed in Chapter 2, 3DUS imaging has facilitated advanced software modules in other brachytherapy techniques. Real-time image guidance would be useful in PBSI to more rapidly assess needle positioning over the system assessed in this work. Needle and seroma segmentation would provide a means to more thoroughly evaluate the quality of the implant, and could be used to perform intra-operative dosimetry. Based on the coverage to the seroma from the actual implanted needle positions, intra-operative adjustments to the treatment plan could automatically be performed to optimized the positions of the remaining needles. Ultimately, a planning procedure based entirely on intra-

operative imaging would eliminate uncertainties in the delivery related to setup and visualization, ensuring precise delivery and treatment of the target volumes as intended.

Overall, PBSI stands to benefit from improved imaging in the planning and delivery procedures. The presented work provides a foundation for continued developments in the technique. Future advancements in image acquisition and delivery guidance can result in improvements to the treatment accuracy and further allow for PBSI to be adapted by a greater number of practitioners.

Bibliography

[1] A. Taghian, B. Smith, and J. Erban, *Breast Cancer - A Multidisciplinary Approach to Diagnosis and Management*. New York: demos Medical, 2010.

[2] E. Elkin, C. Hudis, C. Begg, and D. Schrag, "The effect of changes in tumor size on breast carcinoma survival in the U.S.: 1975-1999." *Cancer*, vol. 104, pp. 1149–57, 2005.

[3] B. Fisher, S. Anderson, J. Bryant, and R. Margolses, "Twenty-year follow-up of a randomized trial comparing total mastectomy, lumpectomy, and lumpectomy plus irradiation for the treatment of invasive breast cancer," *N. Engl. J. Med*, vol. 347, pp. 1233–1241, 2002.

[4] U. Veronesi, N. Cascinelli, L. Mariani, M. Greco, and R. Saccozzi, "Twenty-year follow-up of a randomized study comparing breast-conserving surgery with radical mastectomy for early breast cancer," *N. Engl. J. Med*, vol. 347, pp. 1227–1232, 2002.

[5] F. Vicini, K. Winter, W. Straube, J. Wong, H. Pass, R. Rabinovitch, S. Chafe, D. Arthur, I. Petersen, and B. McCormick, "A phase I/II trial to evaluate three-dimensional conformal radiation therapy confined to the region of the lumpectomy cavity for stage I/II breast carcinoma: Initial report of feasibility and reproducibility of RTOG study 0319," *Int. J. Radiat. Oncol. Biol. Phys.*, vol. 63, pp. 1531–1537, 2005.

[6] F. Vicini, C. Shah, R. Tendulkar, J. Wobb, D. Arthur, A. Khan, D. Wazer, and M. Keisch, "Accelerated partial breast irradiation: An update on published Level I evidence," *Brachytherapy*, vol. 15, pp. 607–615, 2016.

[7] C. Shah, F. Vicini, D. Wazer, D. Arthur, and R. Patel, "The American

Brachytherapy Society consensus statement for accelerated partial breast irradiation." *Brachytherapy*, vol. 12, pp. 267–277, 2013.

[8] J.-P. Pignol, B. Keller, E. Rakovitch, R. Sankreacha, H. Easton, and W. Que, "First report of a permanent breast 103Pd seed implant as adjuvant radiation treatment for early-stage breast cancer." *Int. J. Radiat. Oncol. Biol. Phys.*, vol. 64, pp. 176–181, 2006.

[9] B. Keller, A. Ravi, R. Sankreacha, and J.-P. Pignol, "Permanent breast seed implant dosimetry quality assurance." *Int. J. Radiat. Oncol. Biol. Phys.*, vol. 83, pp. 84–92, 2012.

[10] J.-P. Pignol, J.-M. Caudrelier, J. Crook, C. McCann, P. Truong, and H. a. Verkooijen, "Report on the Clinical Outcomes of Permanent Breast Seed Implant for Early-Stage Breast Cancers," *Int. J. Radiat. Oncol. Biol. Phys.*, vol. 93, pp. 614–621, 2015.

[11] M. McGuffin, T. Merino, B. Keller, and J.-P. Pignol, "Who Should Bear the Cost of Convenience? A Cost-effectiveness Analysis Comparing External Beam and Brachytherapy Radiotherapy Techniques for Early Stage Breast Cancer," *Clinical Oncology*, vol. 29, pp. e57–e63, 2016.

[12] J. Michael, J. Crook, D. Morton, D. Batchelar, M. Hilts, and A. Fenster, "Who Should Bear the Cost of Convenience? A Cost-effectiveness Analysis Comparing External Beam and Brachytherapy Radiotherapy Techniques for Early Stage Breast Cancer," *Clinical Oncology*, vol. 29, pp. 392–393, 2016.

[13] W. J. Meredith, "40 Years of Development in Radiotherapy," *Phys. Med. Biol.*, vol. 29, pp. 115–120, 1984.

[14] H. E. Johns, L. M. Bates, and T. A. Watson, "1000 Curie cobalt units for radiation therapy," *British Journal of Radiology*, vol. 25, pp. 296–302, 1952.

[15] H. E. Johns and J. R. Cunningham, *The Physics of Radiology*, 4th ed. Springfiled: Charles C Thomas, 1983.

[16] E. B. Podgorsak, *Radiation Physics for Medical Physicists*, 2nd ed. Hidelberg: Springer, 2010.

[17] A. Joiner, MC and van der Kogel, Ed., *Basic Clinical Radiobiology*, 4th ed. Hodder Arnold, London UK, 2009.

[18] C. Washington and D. Leaver, Eds., *Principles and Practices of Radiation Therapy*, 2nd ed. St. Louis: Mosby, 2004.

[19] S. Webb, *The Physics of Conformal Radiotherapy: Advances in Technology*. Bristol: Institute of Physics Publishing, 1997.

[20] S. H. Levitt, J. A. Purdy, C. A. Perez, and P. Poortmans, Eds., *Technical Basis of Radiation Therapy*, 5th ed. Hidelberg: Springer, 2012.

[21] J. Venselaar, D. Baltas, A. Meigooni, and P. Hoskin, *Comprehensive Brachytherapy. Physical and Clinical Aspects*. Boca Raton: Taylor & Francis, 2013.

[22] R. Mould, J. Battermann, A. Martinex, and B. Speiser, Eds., *Brachytherapy from Radium to Optimization*. Veenendaal: Nucletron International, 1994.

[23] D. Batchelar, H. Chung, A. Loblaw, N. Law, T. Cisecki, and G. Morton, "Intraoperative ultrasound-based planning can effectively replace postoperative CT-based planning for high-dose-rate brachytherapy for prostate cancer," *Brachytherapy*, vol. 15, pp. 399–405, 2016.

[24] M. Schmid, J. Crook, D. Batchelar, C. Araujo, D. Petrik, D. Kim, and R. Halperin, "A phantom study to assess accuracy of needle identification in real-time planning of ultrasound-guided high-dose-rate prostate implants," *Brachytherapy*, vol. 12, pp. 56–64, 2013.

[25] D. Wazer, D. Arthur, and F. Vicini, Eds., *Accelerated Partial Breast Irradiation Techniques and Clinical Implementations*. Berlin: Springer-Verlag, 2006.

[26] W. Athas, M. Adams-Cameron, W. Hunt, A. Amir-Fazil, and C. Key, "Travel distance to radiation therapy and receipt of radiotherapy following breast-conserving surgery," *J Natl Cancer Inst*, vol. 92, pp. 269–271, 2000.

[27] D. Arthur, D. Koo, R. Zwicker, S. Tong, H. Bear, B. Kaplan, B. Kavanagh, L. Warwicke, D. Holdford, C. Amir, K. Archer, and R. Schmidt-Ullrich, "Partial breast brachytherapy after lumpectomy: Low-dose-rate and high-dose-rate experience," *Int. J. Radiat. Oncol. Biol. Phys.*, vol. 56, pp. 681–689, 2003.

[28] C. Polgár, E. Limbergen, R. Pötter, G. Kovács, A. Polo, J. Lyczek, G. Hildebrandt, P. Niehoff, J. L. Guinot, F. Guedea, B. Johansson, O. Ott, T. Major, and V. Strnad, "Patient selection for accelerated partial-breast irradiation (APBI) after breast-conserving surgery: Recommendations of the GEC-ESTRO breast cancer working group," *Radiotherapy and Oncology*, vol. 94, pp. 264–273, 2010.

[29] F. Vicini, L. Kestin, and N. Goldstein, "Defining the clinical target volume for patients with early-stage breast cancer treated with lumpectomy and accelerated partial breast irradiation: A pathologic analysis," *Int. J. Radiat. Oncol. Biol. Phys.*, vol. 60, pp. 722–730, 2004.

[30] B. Smith, D. Arthur, T. Buchholz, B. Haffty, C. Hahn, P. Hardenbergh, T. Julian, L. Marks, D. Todor, F. Vicini, T. Whelan, J. White, J. Wo, and J. Harris, "Accelerated partial breast irradiation consensus statement from the American Society for Radiation Oncology (ASTRO)." *Int. J. Radiat. Oncol. Biol. Phys.*, vol. 74, pp. 987–1001, 2009.

[31] B. Keller, R. Sankreacha, E. Rakovitch, P. O'brien, and J.-P. Pignol, "A permanent breast seed implant as partial breast radiation therapy for early-stage patients: a comparison of palladium-103 and iodine-125 isotopes based on radiation safety considerations." *Int. J. Radiat. Oncol. Biol. Phys.*, vol. 62, pp. 358–365, 2005.

[32] D. Batchelar, M. Hilts, T. Rose, M. Brandel, E. Garcia, J. Yanchuk, and J. Crook, "Simulation and intraoperaive checks for improved standardization and reproducibility of partial breast seed implant technique [Abstract]," *Brachytherapy*, vol. 13, no. Suppl. 1, p. S84, 2014.

[33] J.-P. Pignol, E. Rakovitch, B. M. Keller, R. Sankreacha, and C. Chartier, "Tolerance and acceptance results of a palladium-103 permanent breast seed implant Phase I/II study." *Int. J. Radiat. Oncol. Biol. Phys.*, vol. 73, pp. 1482–1488, 2009.

[34] J. Godinez and E. C. Gombos, "A permanent breast seed implant as partial-breast radiation therapy for early-stage patients: in regards to Keller et al. (Int J Radiat Oncol Biol Phys 2005;62:358-365)." *Int. J. Radiat. Oncol. Biol. Phys.*, vol. 64, p. 1611, 2006.

[35] D. Batchelar, M. Hilts, M.-P. Milette, and J. Crook, "Starting a Pd-103 Permanent Breast Seed Implant Program: Dosimetric Results for Our First 25 Cases [Abstract]," *Brachytherapy*, vol. 15, no. Suppl. 1, p. S45, 2016.

[36] T. Berrang, P. Truong, C. Popescu, L. Drever, H. Kader, M. Hilts, T. Mitchell, S. Y. Soh, L. Sands, S. Silver, and I. Olivotto, "3D ultrasound can contribute to planning CT to define the target for partial breast radiotherapy." *Int. J. Radiat. Oncol. Biol. Phys.*, vol. 73, pp. 375–383, 2009.

[37] F. Khan, *The Physics of Radiation Therapy*, 4th ed. Philadelphia: Lippincott Williams & Wilkins, 2010.

[38] J. Bushberg, A. Seibery, E. Leidholdt, and J. Boone, *The Essential Physics of Medical Imaging*, 3rd ed., C. Mitchell, Ed. Philadelphia: Lippincott Williams & Wilkins, 2012.

[39] P. Mayles, A. Nahum, and J. Rosenwald, Eds., *Handbook of Radiotherapy Physics: Theory and Practice*. New York: Taylor & Francis, 2007.

[40] D. De Frenne, "Nuclear Data Sheets for A = 103," *Nuclear Data Sheets*, vol. 110, pp. 2081–2256, 2009.

[41] Brookhaven National Laboratory, "National Nuclear Data Center - Decay Radiation Results 103Pd," 2009. [Online]. Available: www.nndc.bnl.gov/chart/decaysearchdirect.jsp?nuc=103PD&unc=nds

[42] D. Downey, A. Fenster, and J. Williams, "Clinical utility of three-dimensional US." *Radiographics*, vol. 20, pp. 559–571, 2000.

[43] A. Fenster, D. B. Downey, and H. N. Cardinal, "Three-dimensional ultrasound imaging," *Phys. Med. Biol.*, vol. 46, pp. R67–R99, 2001.

[44] J. Beutel, H. L. Kundel, and R. L. Van Metter, Eds., *Handbook of Medical Imaging: Volume 1. Physics and Psychophysics*. Bellingham: SPIE, 2000.

[45] J. Williamson, B. Thomadsen, and R. Nath, Eds., *Brachytherapy Physics*. Madison: Medical Physics Publishing Corporation, 1994.

[46] R. Nath, L. Anderson, G. Luxton, K. Weaver, and J. Williamson, "Dosimetry of interstitial brachytherapy sources: recommendations of the AAPM Radiation

Therapy Committee Task Group No. 43. American Association of Physicists in Medicine." *Med. Phys.*, vol. 22, pp. 209–234, 1995.

[47] P. Devlin, Ed., *Brachytherapy Applications and Techniques*. Philadelphia: Lippincott Williams & Wilkins, 2007.

[48] J. Crook, J. Borg, A. Evans, A. Toi, E. P. Saibishkumar, S. Fung, and C. Ma, "10-year experience with I-125 prostate brachytherapy at the Princess Margaret Hospital: Results for 1,100 Patients," *Int. J. Radiat. Oncol. Biol. Phys.*, vol. 80, pp. 1323–1329, 2011.

[49] S. Tong, D. Downey, H. Cardinal, and A. Fenster, "A three-dimensional ultrasound prostate imaging system," *Ultrasound in Med. & Biol.*, vol. 22, pp. 735–746, 1996.

[50] R. Nath, W. Bice, W. Butler, Z. Chen, A. Meigooni, V. Narayana, M. Rivard, and Y. Yu, "AAPM recommendations on dose prescription and reporting methods for permanent interstitial brachytherapy for prostate cancer: report of Task Group 137." *Med. Phys.*, vol. 36, pp. 5310–5322, 2009.

[51] T. A. King, J. S. Bolton, R. R. Kuske, G. M. Fuhrman, T. G. Scroggins, and X. Z. Jiang, "Long-term results of wide-field brachytherapy as the sole method of radiation therapy after segmental mastectomy for T(is,1,2) breast cancer," *American Journal of Surgery*, vol. 180, pp. 299–304, 2000.

[52] P. De Jean, L. Beaulieu, and A. Fenster, "Three-dimensional ultrasound system for guided breast brachytherapy," *Med. Phys.*, vol. 36, no. 11, p. 5099, 2009.

[53] E. Poulin, L. Gardi, K. Barker, J. Montreuil, A. Fenster, and L. Beaulieu, "Validation of a novel system for real-time planning and guidance of breast interstitial HDR brachytherapy," *Med. Phys.*, vol. 6830, pp. 1–23, 2015.

[54] H. M. Ladak, F. Mao, Y. Wang, D. B. Downey, D. Steinman, and A. Fenster, "Prostate boundary segmentation from 2D ultrasound images." *Med. Phys.*, vol. 27, pp. 1777–1788, 2000.

[55] Y. Wang, H. Cardinal, D. Downey, and A. Fenster, "Semiautomatic three-dimensional segmentation of the prostate using two-dimensional ultrasound images." *Med. Phys.*, vol. 30, pp. 887–897, 2003.

[56] W. Qiu, M. Yuchi, M. Ding, D. Tessier, and A. Fenster, "Needle segmentation using 3D Hough transform in 3D TRUS guided prostate transperineal therapy." *Med. Phys.*, vol. 40, p. 042902, 2013.

[57] M. Ding, Z. Wei, L. Gardi, D. B. Downey, and A. Fenster, "Needle and seed segmentation in intra-operative 3D ultrasound-guided prostate brachytherapy." *Ultrasonics*, vol. 44, pp. e331–e336, 2006.

[58] E. Poulin, L. Gardi, A. Fenster, J. Pouliot, and L. Beaulieu, "Towards real-time 3D ultrasound planning and personalized 3D printing for breast HDR brachytherapy treatment," *Radiotherapy and Oncology*, vol. 114, pp. 335–338, 2015.

[59] M. Hilts, D. Batchelar, J. Rose, and J. Crook, "Deformable image registration for defining the postimplant seroma in permanent breast seed implant brachytherapy," *Brachytherapy*, vol. 14, pp. 409–418, 2015.

[60] D. Morton, M. Hilts, D. Batchelar, and J. Crook, "Seed Placement in Permanent Breast Seed Implant Brachytherapy: Are Concerns Over Accuracy Valid?" *Int. J. Radiat. Oncol. Biol. Phys.*, vol. 95, pp. 1050–1057, 2016.

[61] H. Kader, P. Truong, R. Pai, M. Panades, S. Jones, W. Ansbacher, and I. Olivotto, "When Is CT-Based Postoperative Seroma Most Useful to Plan Partial Breast Radiotherapy? Evaluation of Clinical Factors Affecting Seroma Volume and Clarity," *Int. J. Radiat. Oncol. Biol. Phys.*, vol. 72, pp. 1064–1069, 2008.

[62] E. Wong, P. Truong, H. Kader, A. Nichol, L. Salter, R. Petersen, E. Wai, L. Weir, and I. Olivotto, "Consistency in seroma contouring for partial breast radiotherapy: impact of guidelines." *Int. J. Radiat. Oncol. Biol. Phys.*, vol. 66, pp. 372–6, 2006.

[63] M. Hilts, H. Halperin, D. Morton, D. Batchelar, F. Bachand, R. Chowdhury, and J. Crook, "Skin dose in breast brachytherapy: Defining a robust metric," *Brachytherapy*, vol. 14, pp. 970–978, 2015.

[64] B. M. Keller, J.-P. Pignol, E. Rakovitch, R. Sankreacha, and P. O'Brien, "A radiation badge survey for family members living with patients treated with a (103)Pd permanent breast seed implant." *Int. J. Radiat. Oncol. Biol. Phys.*, vol. 70, no. 1, pp. 267–71, 2008.

[65] J. Rebekah Shin, M. McGuffin, J. Pignol, B. Keller, and L. D'Alimonte, "Permanent breast seed implant for early-stage breast cancer: Impact of primary tumour location on the overall cosmetic outcome," *Journal of Medical Imaging and Radiation Sciences*, vol. 46, pp. 85–89, 2015.

[66] E. Watt, S. Husain, M. Sia, D. Brown, K. Long, and T. Meyer, "Dosimetric variations in permanent breast seed implant due to patient arm position," *Brachytherapy*, vol. 14, pp. 979–985, 2015.

[67] S. Mashouf, E. Fleury, P. Lai, T. Merino, E. Lechtman, A. Kiss, C. McCann, and J.-P. Pignol, "Clinical Significance of Accounting for Tissue Heterogeneity in Permanent Breast Seed Implant Brachytherapy Planning," *Int. J. Radiat. Oncol. Biol. Phys.*, vol. 94, pp. 816–823, 2016.

[68] D. Bowes, M. Gaztañaga, C. Araujo, D. Kim, B. Parker, D. Batchelar, M.-P. Milette, R. Rajapakshe, D. Petrik, R. Halperin, and J. Crook, "A randomized trial comparing seed displacement of coated seeds to regular loose seeds at 30 days postimplant." *Brachytherapy*, vol. 12, pp. 362–367, 2013.

[69] H. Johnston, M. Hilts, W. Beckham, and E. Berthelet, "3D ultrasound for prostate localization in radiation therapy: a comparison with implanted fiducial markers," *Int. J. Radiat. Oncol. Biol. Phys.*, vol. 35, pp. 2403–2413, 2008.

[70] D. Robinson, D. Liu, S. Steciw, C. Field, H. Daly, E. P. Saibishkumar, G. Fallone, M. Parliament, and J. Amanie, "An evaluation of the Clarity 3D ultrasound system for prostate localization." *Journal of Applied Clinical Medical Physics*, vol. 13, p. 3753, 2012.

[71] F. Cury, G. Shenouda, L. Souhami, M. Duclos, S. Faria, M. David, F. Verhaegen, R. Corns, and T. Falco, "Ultrasound-based image guided radiotherapy for prostate cancer-comparison of cross-modality and intramodality methods for daily localization during external beam radiotherapy," *Int. J. Radiat. Oncol. Biol. Phys.*, vol. 66, pp. 1562–1567, 2006.

[72] R. Heimann, D. Hard, and J. Archambault, "Three dimensional ultrasound (3DUS) image guidance, clips or CT: How to optimally localize the breast lumpectomy cavity volume? [Abstract]," *Int. J. Radiat. Oncol. Biol. Phys.*, vol. 75, no. Suppl. 1, p. S196, 2009.

[73] P. Wong, T. Muanza, E. Reynard, K. Robert, J. Barker, and K. Sultanem, "Use of three-dimensional ultrasound in the detection of breast tumor bed displacement during radiotherapy," *Int. J. Radiat. Oncol. Biol. Phys.*, vol. 79, pp. 39–45, 2011.

[74] R. Bude and R. Adler, "An easily made, low-cost, tissue-like ultrasound phantom material," *Journal of Clinical Ultrasound*, vol. 23, pp. 271–273, may 1995.

[75] L. Drever and M. Hilts, "Daily quality assurance phantom for ultrasound image guided radiation therapy," *Journal of Applied Clinical Medical Physics*, vol. 8, pp. 126–136, 2007.

[76] R. P. Petersen, P. Truong, H. Kader, E. Berthelet, J. C. Lee, M. Hilts, A. Kader, W. Beckham, and I. Olivotto, "Target Volume Delineation for Partial Breast Radiotherapy Planning: Clinical Characteristics Associated with Low Interobserver Concordance," *Int. J. Radiat. Oncol. Biol. Phys.*, vol. 69, pp. 41–48, 2007.

[77] H. Struikmans, C. Wárlám-Rodenhuis, T. Stam, G. Stapper, R. Tersteeg, G. H. Bol, and C. Raaijmakers, "Interobserver variability of clinical target volume delineation of glandular breast tissue and of boost volume in tangential breast irradiation," *Radiother. Oncol.*, vol. 76, pp. 293–299, 2005.

[78] J. Michael, D. Morton, D. Batchelar, M. Hilts, and A. Fenster, "Intraoperative 3D ultrasound guidance system for permanent breast seed implantation," *Proc. SPIE, Medical Imaging*, vol. 101351B, 2017.

[79] D. Rickey, P. Picot, D. Christopher, and A. Fenster, "A wall-less vessel phantom for doppler ultrasound studies," *Ultrasound in Med. & Biol.*, vol. 21, pp. 1163–1176, 1995.

[80] P. DeJean, M. Brackstone, and A. Fenster, "An intraoperative 3D ultrasound system for tumor margin determination in breast cancer surgery." *Med. Phys.*, vol. 37, pp. 564–70, 2010.

[81] J. Kishimoto, S. de Ribaupierre, D. S. C. Lee, R. Mehta, K. St Lawrence, and A. Fenster, "3D ultrasound system to investigate intraventricular hemorrhage in preterm neonates." *Physics in Medicine and Biology*, vol. 58, pp. 7513–7526, 2013.

[82] A. Thouvenot, T. Poepping, T. M. Peters, and E. C. S. Chen, "Characterization of Various Tissue Mimicking Materials for Medical Ultrasound Imaging," *Proc. SPIE, Medical Imaging*, vol. 97835E, 2016.

[83] F. Vicini, J. White, D. Arthur, R. Kuske, and R. Rabinovitch, "NSABP protocol B-39/RTOG protocol 0413: A randomized phase III study of conventional whole breast irradiation (WBI) versus partial breast irradiation for women with stage 0, I, or II breast cancer," 2005. [Online]. Available: www.rtog.org/ClinicalTrials/ProtocolTable/StudyDetails.aspx?study=0413

[84] R. Topolnjak, P. de Ruiter, P. Remeijer, C. van Vliet-Vroegindeweij, C. Rasch, and J. Sonke, "Image-guided radiotherapy for breast cancer patients: surgical clips as surrogate for breast excision cavity." *Int. J. Radiat. Oncol. Biol. Phys.*, vol. 81, pp. e187–195, 2011.

[85] A. Landry, T. Berrang, I. Gagne, C. Popescu, T. Mitchell, H. Vey, L. Sand, S. Y. Soh, J. Wark, I. Olivotto, and W. Beckham, "Investigation of variability in image acquisition and contouring during 3D ultrasound guidance for partial breast irradiation." *Radiation Oncology*, vol. 9, p. 35, 2014.

[86] M. C. Smitt, R. L. Birdwell, and D. R. Goffinet, "Breast electron boost planning: comparison of CT and US." *Radiology*, vol. 219, pp. 203–206, 2001.

[87] L. E. Esserman, M. Cura, and D. DaCosta, "Recognizing pitfalls in early and late migration of clip markers after imaging-guided directional vacuum-assisted biopsy." *Radiographics*, vol. 24, pp. 147–156, 2004.

[88] T. Podder, L. Beaulieu, B. Caldwell, R. Cormack, J. Crass, A. Dicker, A. Fenster, G. Fichtinger, M. Meltsner, M. a. Moerland, R. Nath, M. J. Rivard, T. Salcudean, D. Y. Song, B. R. Thomadsen, and Y. Yu, "AAPM and ESTRO guidelines for image-guided robotic brachytherapy: Report of Task Group 192," *Med. Phys.*, vol. 41, p. 101501, 2014.

[89] R. Taschereau, J. Pouliot, J. Roy, and D. Tremblay, "Seed misplacement and stabilizing needles in transperineal permanent prostate implants," *Radiotherapy and Oncology*, vol. 55, pp. 59–63, 2000.

[90] I. Kaplan, P. Meskell, M. Lieberfarb, B. Saltzman, S. Berg, and E. Holupka, "A comparison of the precision of seeds deposited as loose seeds versus suture embedded seeds: A randomized trial," *Brachytherapy*, vol. 3, pp. 7–9, 2004.

[91] L. Fu, H. Liu, R. Brasacchio, D. Rubens, J. Strang, E. Messing, and Y. Yu, "Clinical observation and modeling of postimplant seed displacement for prostate brachytherapy [Abstract]," *Int. J. Radiat. Oncol. Biol. Phys.*, vol. 63, no. Suppl. 1, pp. S504–S505, 2005.

[92] S. Sidhu, W. J. Morris, I. Spandinger, M. Keyes, M. Hilts, R. Harrison, K. Otto, M. McKenzie, and A. Agranovich, "Prostate brachytherapy postimplant dosimetry: A comparison of prostate quadrants," *Int. J. Radiat. Oncol. Biol. Phys.*, vol. 52, pp. 544–552, 2002.

[93] N. Nasser, Y. Wang, J. Borg, and E. Saibishkumar, "Sector analysis of dosimetry of prostate cancer patients treated with low-dose-rate brachytherapy," *Brachytherapy*, vol. 13, pp. 369–374, 2014.

[94] G. Merrick, W. Butler, P. Grimm, M. Morris, J. Lief, A. Bennett, and R. Fiano, "Multisector prostate dosimetric quality: Analysis of a large community database," *Brachytherapy*, vol. 13, pp. 146–151, 2014.

[95] D. E. Wazer, D. W. Aurthur, and F. A. Vicini, Eds., *Accelerated Partial Breast Irradiation*. Hidelberg: Springer-Verlag, 2009.

[96] D. Morton, D. Batchelar, M. Hilts, T. Berrang, and J. Crook, "Incorporating three-dimensional ultrasound into permanent breast seed implant brachytherapy treatment planning," *Brachytherapy*, vol. 16, pp. 167–173, 2017.

[97] H. Goldberg, R. Prosnitz, J. Olson, and L. Marks, "Definition of postlumpectomy tumor bed for radiotherapy boost field planning: CT versus surgical clips," *Int. J. Radiat. Oncol. Biol. Phys.*, vol. 63, pp. 209–213, 2005.

[98] T. Major, C. Gutierrez, B. Guix, E. Van Limbergen, V. Strnad, and C. Polgar, "Recommendations from GEC ESTRO Breast Cancer Working Group (II): Target definition and target delineation for accelerated or boost partial breast irradiation using multicatheter interstitial brachytherapy after breast conserving open cavity surgery," *Radiother. Oncol.*, vol. 118, pp. 199–204, 2016.

[99] C. Coles, C. Cash, G. Treece, F. Miller, A. Hoole, A. Gee, R. Prager, R. Sinnatamby, P. Britton, J. Wilkinson, A. Purushotham, and N. Burnet, "High definition three-dimensional ultrasound to localise the tumour bed: A breast radiotherapy planning study," *Radiother. Oncol.*, vol. 84, pp. 233–241, 2007.

[100] J. Ringash, T. Whelan, E. Elliott, T. Minuk, K. Sanders, H. Lukka, and H. Reiter, "Accuracy of ultrasound in localization of breast boost field," *Radiother. Oncol.*, vol. 72, pp. 61–66, 2004.

[101] C. Leonard, C. L. Harlow, C. Coffin, J. Drose, L. Norton, and J. Kinzie, "Use of ultrasound to guide radiation boost planning following lumpectomy for carcinoma of the breast," *Int. J. Radiat. Oncol. Biol. Phys.*, vol. 27, pp. 1193–1197, 1993.

[102] F. Perera, E. Yu, J. Engel, R. Holliday, L. Scott, F. Chisela, and V. Venkatesan, "Patterns of breast recurrence in a pilot study of brachytherapy confined to the lumpectomy site for early breast cancer with six years' minimum follow-up," *Int. J. Radiat. Oncol. Biol. Phys.*, vol. 57, pp. 1239–1246, 2003.

[103] F. Vicini, D. Arthur, C. Polgar, and R. Kuske, "Defining the efficacy of accelerated partial breast irradiation: The importance of proper patient selection, optimal quality assurance, and common sense," *Int. J. Radiat. Oncol. Biol. Phys.*, vol. 57, pp. 1210–1213, 2003.

[104] R. R. Kuske, K. Winter, D. Arthur, J. Bolton, R. Rabinovitch, J. White, W. Hanson, and R. Wilenzick, "Phase II trial of brachytherapy alone after lumpectomy for select breast cancer: Toxicity analysis of RTOG 95-17," *Int. J. Radiat. Oncol. Biol. Phys.*, vol. 65, pp. 45–51, 2006.

[105] D. Landis, W. Luo, J. Song, J. Bellon, R. Punglia, J. Wong, J. Killoran, R. Gelman, and J. Harris, "Variability Among Breast Radiation Oncologists in Delineation of the Postsurgical Lumpectomy Cavity," *Int. J. Radiat. Oncol. Biol. Phys.*, vol. 67, pp. 1299–1308, 2007.

[106] V. Strnad, J. Hannoun-Levi, J. Guinot, K. Lossl, D. Kauer-Dorner, A. Resch, G. Kovacs, T. Major, and E. Van Limbergen, "Recommendations from GEC ESTRO Breast Cancer Working Group (I): Target definition and target delineation for accelerated or boost partial breast irradiation using multicatheter

interstitial brachytherapy after breast conserving open cavity surgery," *Radiother. Oncol.*, vol. 115, pp. 342–348, 2015.

[107] T. Major, C. Gutiérrez, B. Guix, E. Mózsa, J. Hannoun-Levi, K. Lössl, P. Niehoff, A. Resch, E. van Limbergen, and C. Polgar, "Interobserver variations of target volume delineation in multicatheter partial breast brachytherapy after open cavity surgery," *Brachytherapy*, vol. 14, pp. 925–932, 2015.

[108] R. Sharma, M. Spierer, S. Mutyala, N. Thawani, H. W. Cohen, L. Hong, M. K. Garg, and S. Kalnicki, "Change in Seroma Volume During Whole-Breast Radiation Therapy," *Int. J. Radiat. Oncol. Biol. Phys.*, vol. 75, pp. 89–93, 2009.

[109] A. Frederick, E. Watt, M. Peacock, S. Husain, T. Meyer, and M. Roumeliotis, "Positional accuracy in Pd-103 permanent breast seed implant (PBSI) brachytherapy at the Tom Baker Cancer Centre [Abstract]," *Med. Phys.*, vol. 43, pp. 4933–4934, 2016.

[110] D. Pfeiffer, S. Sutlief, W. Feng, H. M. Pierce, and J. Kofler, "AAPM Task Group 128: quality assurance tests for prostate brachytherapy ultrasound systems." *Med. Phys.*, vol. 35, pp. 5471–5489, 2008.